NORTHWESTERN UNIVERSITY

Towards Understanding and Designing of Advanced Li-ion Batteries from First-principles

A DISSERTATION

SUBMITTED TO THE GRADUATE SCHOOL

IN PARTIAL FULFILLMENT OF THE REQUIREMENTS

for the degree

DOCTOR OF PHILOSOPHY

Field of Materials Science and Engineering

By

Zhenpeng Yao

EVANSTON, ILLINOIS

March 2018

ABSTRACT

Lithium ion batteries (LIBs) have been the most prominent electrochemical energy storage technology over the past decades and enabled the wireless evolution of portable electronic devices. Yet the expanded use of renewable but intermittent energy sources coupled with increasing demand for electric transportation vehicles put forward requirements to electrochemical energy storage techniques for higher capacity, lower cost, and fast rate capacity. State-of-the-art LIB electrodes are typically lithium transition metal oxides and phosphates, which store (release) the electrical energy *via* the Li extraction and re-accommodation, accompanied by redox reactions of TM cations. The specific capacity of the electrode is therefore limited by the safe amount of Li can be removed from the system without causing structure collapse and the number of electrons per TM cation that can participate in the redox reaction. To boost the capacity and energy density, conversion reaction electrode materials which can overcome the inherent structural limitation and anionic redox active electrodes with oxygen ions complementarily providing the charge-compensating electrons were introduced to the rechargeable battery chemistry. Here we use the density functional theory (DFT) based first-principles calculations to understand the electrochemical charge and discharge of the conversion reaction electrodes *via* exploring the equilibrium and non-equilibrium thermodynamics with a mechanistic method as designed. We provide detailed information for the origin of large voltage hysteresis and volume expansion which have been hindering the practical application of conversion reaction materials and offer tips on alleviating them through reasonably operation range restrictions. Our findings are reproducible among several well-known transition metal (TM) oxide/sulfide conversion-type electrodes (*e.g.* Co_3O_4, NiO, CuS). For the anionic redox

active electrodes, we demonstrate how the coordination structure and bonding environment enable the reversible oxygen redox in the $3d$ metal oxides. The specific redox active Li_6-O local Li-excess configuration as identified for the iron oxide electrode enriches the anionic redox battery chemistry with a low-cost high energy density battery designed. For the manganese oxide anionic redox active electrodes, we predict novel materials with improved properties compared to the original system through high-throughput DFT screening. On the other hand, using kinetics calculations we discover a novel 2-dimensional material with superior electric and ionic conductivity compared to traditional 2-dimensional nano sheet like graphene which can be used to boost the rate capacity of state-of-the-art LIBs. We accurately reveal the mechanism of the kinetics-dominated electrochemical sodiation and lithiation reactions of selenium. We clarify the relationship between the stability and ionic conductivity of the complex borohydride based lithium ion conductors and giving guidance on their further investigations. Our findings will shed light on the development of the next generation, high energy density, and fast rate advanced lithium ion batteries.

Acknowledgements

I am highly proud to have an opportunity to express my sincerest appreciation to all the help I got in the past several years.

First and foremost, I would like to thank my advisor Prof. Chris Wolverton, who has been leading my way since I was a toddler in the computational material science field. His patience, wisdom, and vision are the reasons for what I have achieved now and in a long future. To me, Chris is a marvelous advisor as well as a thoughtful mentor, I cannot imagine how much more load that means, yet what I learned from him are not only about how to be a competent scientist, but also on being continuously enthusiastic to science and the higher truth, staying courageous to be whoever you want to be, and always keeping democracy and equality in mind.

I am eager to express my deepest appreciation to my committee members: Prof. Vinayak P. Dravid, Prof. Mark Hersam, and Dr. Maria K.Y. Chan for not only have been giving me valuable comments and advice to my thesis work but also guiding me on my research and what's more, giving me significant supports to my career development.

I would like to thank Dr. Michael M. Thackeray for his guidance to my research work and the huge support to my career development. It's an honor and fortune to work with the pioneer and most fabulous scientist in the battery field. Meanwhile, I would like to thank Dr. Christopher Johnson, Dr. Paul Fenter, and all my colleagues in the Center for Electrochemical Energy Science who have made my work in the center fruitful and given tremendous support to my career development.

I want to give my greatest appreciation to Dr. Jinsong Wu, Dr. Kai He, Dr. Qianqian Li, Dr. Lei Li, Dr. Chun Zhan, Dr. Jun Lu, Dr. Kahlil Amine, Dr. Lingzi Sang, Prof. Dong

Su, Prof. Shenmin Zhu, and all my colleagues who have been helping me explore the beauty of materials science and who are always able to make amazing discoveries. They are fantastic physicists, chemists, as well as teachers and partners.

I would like to thank Dr. Jiangang He, Dr. Maximilian Amsler, Dr. Shahab Naghavi, Dr. Yongsheng Zhang, Dr. Kyle Michel, Dr. Shiqiang Hao, Dr. Zhi Lu, Dr. Yongli Wang, Dr. Soo Kim, Dr. Muratahan Aykol, Mr. Vinay Hegde, and all the members from the Wolverton group who have been giving me selfless and tireless help and assistance on my research.

Sincerely thanks to my friends at Northwestern especially Ming Han, Bi-Cheng Zhou, and Lei Li, whose brilliance has been impressing and inspiring me.

I want to give special thanks to my family which has been giving me unconditional support and powerful backing whenever I need it.

Last but not least, thanks to my special one, Ruomeng Qiu, who has been making all my efforts meaningful and lightening my life with her intelligence, cuteness, and love.

Table of Contents

List of Tables

List of Figures

CHAPTER 1

Introduction

Since the first rechargeable lithium ion battery was patented by Yoshino and his coworkers in 1987[1] and later commercialized by Sony, lithium ion battery (LIB) has enabled the wireless evolution of portable devices including cell phones, laptop computers, digital cameras and so on. However, the expanded use of renewable but intermittent energy sources such as solar energy, wind power, and marine energy, coupled with increasing demand for electric transportation vehicles (EVs), put forward requirements to LIBs for higher capacity, lower cost, and fast rate capability.

State-of-the-art electrodes that have been investigated for commercial applications fall mainly into three categories.[2,3] The first group is layered lithium compounds with a close packed oxygen anion lattice. These materials are $LiCoO_2$,[4] and compositional variations such as $LiNi_{1-x}Co_xAl_xO_2$,[5] and $LiNi_xMn_xCo_{1-2x}O_2$.[5] The second group consists materials having 3D spinel structure like $LiMn_2O_4$.[6] The third group contains transition metal phosphates, such as the olivine $LiFePO_4$,[7] with 1D Li ion diffusion channels. Generally, all of these electrodes function *via* the intercalation mechanism during Li accommodation and extraction with the preserved crystal structure, accompanied by redox reactions of transition metal cations. The specific capacity of the electrode is then limited by the safe amount of Li removal without impairing the structure backbone and the number of electrons per transition metal cation that can participate in the redox reaction. Therefore, the development of novel high energy electrode materials for rechargeable lithium ion batteries is becoming more essential.

Electrodes work with conversion mechanism are suggested which can achieve a significantly larger capacity by overcoming the inherent structural limitation. Many transition metal oxides (MOs) and sulfides (MSs) have been investigated in the past as conversion electrodes[8,9], exhibiting different chemical reactions, electrochemical performance, and reversibility. Yet the detailed phase evolution and electrochemistry during the cycling of conversion type electrodes are usually unclear which adds on the hindrance for their practical application.

Meanwhile, the exclusive transition metal redox as mentioned for state-of-the-art electrodes materials is also challenged by the recent discovery of anionic redox reactivity in Li-excess materials, which can be taken advantage of to greatly boost the capacity of anionic redox active electrodes.[10–16] In fact, the anions, rather than the TM ions, are essential as counter-ions and the structural hosts in the Li-driven cathode materials. These studies provide the possibility of boosting the capacity and energy density if anionic and cationic redox activity can be enabled at the same voltage plateau. The exploration of this new opportunity requires a fundamental understanding of the mechanism underpinning the anionic redox chemistry in category variety of battery materials.

On the other hand, the emerging applications like EVs require substantially higher rate capabilities than what can be achieved by state-of-the-art LIBs to be competitive to the combustion engines in terms of the refueling time. Understanding the Li-ion mass transport in the battery materials during the electrochemical cycling is therefore becoming crucial and designing batteries with improved Li-ion conductivity by exploring the kinetic bottlenecks has drawn a significant amount of attention.

First-principles density functional theory (DFT) calculations have been widely used as effective tools to study battery materials to explore new, high-performance electrode materials, understand in detail the underlying mechanisms during electrochemical reactions, and explore the ionic kinetics in battery materials.[17–25] In this thesis, we attempt to understand the state-of-the-art Li-ion chemistries by exploring the relationship between electrode materials atom identity, composition, structure and their properties and use the predictive theory obtained to design advanced Li-ion batteries through first-principles calculations. In Chapter 2, we provide a brief background on the conventional batteries, conversion reaction electrodes, anionic redox active electrodes, and solid state electrolytes. The computational methods used during the course of our research studies are also presented in Chapter 2. In Chapter 3, we discuss the non-equilibrium thermodynamics in the electrochemistry and their impact to the battery performance, as well as a mechanistic method as designed to explore the non-equilibrium thermodynamics. In Chapter 4, we apply this method to reveal the conversion reaction mechanisms during electrochemical lithiation process of several well-known transition metal oxides and sulfides. In Chapter 5 and 6, we discuss the high energy density electrode designing by utilizing the combined cationic and anionic redox reactivity. In Chapter 7, we discovered a novel 2-dimensional material which exhibits superb electric and especially ionic conductions which can be used to boost the rate capacity of current electrodes in lithium ion batteries. In Chapter 8, we investigate the kinetics-dominant reaction mechanisms of Selenium sodiation and lithiation by examining the Li-ion and Na-ion conductivity using first-principle calculations. In Chapter 9, we study the stability and conductivity of a complex lithium borohydride based

solid-state electrolyte. In Chapter 10, we provide a summary of the work presented in this

thesis and future research directions.

CHAPTER 2

Background and Methodology

2.1 Lithium-ion Batteries (LIBs)

2.1.1 Conventional LIBs

The conventional Li-ion cell is comprised of a layered graphite anode, an organic electrolyte and an intercalation cathode (*e.g.* $Li_{1-x}CoO_2$). Li-ions shuttle between these two electrodes through the electrolyte. On discharge, Li-ions leave the anode and intercalate into the layered structure of the cathode material as shown in Equation 2.1, with electrons flowing through the external wiring to generate power. During charging, the process is reversed under an applied voltage (Figure 2.1). The specific capacity of the electrode is then limited by the safe amount of Li removal without impairing the structure backbone and the number of electrons per transition metal cation that can participate in the redox reaction.

$$xLi + Li_{1-x}CoO_2 \leftrightarrow LiCoO_2 \tag{2.1}$$
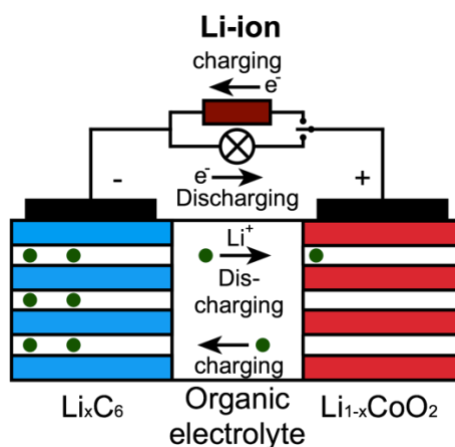
Figure 2.1 Schematic of the conventional lithium-ion battery ($LiCoO_2$ cathode/graphite anode) operation.

2.1.2 Conversion reaction electrodes

Different with the intercalation-type electrode materials, lithium ions (de-)insert conversion reaction electrodes *via* a series of chemical reactions, converting the original compound to new chemical phases as shown in Equation 2.2.

$$mn\text{Li} + \text{MX}_m \leftrightarrow \text{M} + m\text{Li}_n\text{X} \tag{2.2}$$

Conversion-type materials can achieve a significantly larger capacity by overcoming this inherent structural limitation of intercalation electrodes; however, they pose other problems such as limited reversibility and voltage hysteresis. In these conversion-type reactions, non-equilibrium phases often form during repeated charging/discharging cycles, and these non-equilibrium pathways directly affect the electrochemical performance.[26–28] A phase transformation of these non-equilibrium phases to their thermodynamically ground state structures can occur spontaneously (as $t \rightarrow \infty$); however, there may not be sufficient time to allow transformations from non-equilibrium phases into their equilibrium counterparts. The battery performance can be greatly influenced by these non-equilibrium (de-)lithiation reactions, that could affect its capacity and cyclability, as well as cause a voltage hysteresis.[29–37] Also, due to the transient nature of these non-equilibrium phases, it can be challenging to identify and characterize them experimentally during electrochemical reactions.[29,31]

Transition metal oxides (TMO) and sulfides (TMS) such as Co_3O_4,[38] $(Cu,Co)_3O_4$,[39] NiO,[40] MoS_2,[41] and CuS[42] are of significant interest as conversion anode materials for lithium-ion batteries, due to their remarkably high theoretical capacities and low cost. While many previous experiments have found that the charge/discharge reactions of those TMO(S)s can be reversible, detailed information about the mechanisms

of these reactions, such as the detailed phase transition, possible existence of intercalation process, and the origin of the voltage hysteresis between the charge/discharge cycles, are still poorly understood.

2.1.3 Anionic redox active electrodes

The exclusive dependence on the TM cations as the redox center in cathode materials typically used in LIBs has been challenged by the recent discovery of oxygen redox reactivity in Li-excess cathode materials. Hideyuki *et al.*[43] and Sathiya *et al.*[10,15] first reported that the enhanced capacities in $Li_{1.20}Mn_{0.54}Co_{0.13}Ni_{0.13}O_2$ and $Li_2Ru_{1-y}Sn_yO_3$ can be realized *via* reversible *anionic* redox: $O^{2-} \rightarrow (O_2)^{n-}$. In a number of further studies, the redox activity of the anionic species, oxygen, has been confirmed, *e.g.*, during the electrochemical cycling of the Li_4FeSbO_6,[12] Li_3NbO_4,[44] β-Li_2IrO_3,[45] and Li_5FeO_4[46] compounds. Understanding the origin of the oxygen redox, therefore, has become essential. McCalla *et al.* and Grimaud *et al.* proposed that the Li-driven reversible formation of peroxo-like $(O_2)^{n-}$ species boosts the energy storage capacity of these Li-excess materials.[11,16] Different explanations have been given by Luo *et al.* [47], Seo *et al.* [14] and Yao *et al.*[48] who suggest that the formation of localized electron holes on O atoms with local Li-excess environments (contrary to $(O_2)^{n-}$ dimers) are responsible for the excess capacity during Li removal. Exploration of these Li-rich compounds with combined cationic and anionic redox chemistry, high energy density, no O_2 loss, and low-cost are still ongoing and have drawn significant attention from the electrochemical energy storage field.

2.1.4 Solid state electrolytes

Since the commercialization of LIBs,[49] organic liquids have exclusive been the only kind of electrolytes used in commercial systems, which is now a significant safety concern for emerging applications such as electric vehicles and grid storage because of the high risk of leakage[50] and flammability.[51] Besides, a dendritic lithium growth over the extended cell cycling can lead to a short circuit in LIBs, where a lithium metal is used as the anode, as well as containing the organic liquid electrolyte.[52] In addition, some of the cathode materials tend to dissolve in the electrolyte (*e.g.*, Mn ions in $LiMn_2O_4$ spinel cathodes) that can further reduce the overall efficiency of LIBs.[53] The use of an inorganic solid-state electrolyte (SSE) was therefore suggested, instead of using an organic liquid electrolyte, in order to circumvent such disadvantages.[54] Various types of crystalline lithium conducting SSE materials have been studied to date. For example, lithium nitrides,[55] lithium hydrides,[56–60] perovskite-type oxides,[61] argyrodites,[62] garnets,[63] NASICON[64], LISICON[65], and $Li_{10}MP_2S_{12}$ (M = Si, Ge, Sn)[66,67] have been investigated as promising SSE candidates for LIBs.

2.2 Density functional theory (DFT)

2.2.1 Introduction to first-principles density functional theory

While the Schrodinger equation has enable calculations of the quantum state of electronic (and other) systems, it can only be solved exactly for a few simple realistic situations like hydrogen atom. For atoms containing many electrons, a lithium atom for example, the Schrodinger equation quickly becomes intractable because of the many-body electron-electron interaction. For each electron, the wave function has three variables, so a

lithium atom would involve a wave function of nine variables. One enormous simplification to the problem was achieved when Hohenberg and Kohn[68] proves that an external potential acting on electrons, $V_{ext}(\boldsymbol{r})$, in a many electron system is a unique functional of density of electrons, $n(\boldsymbol{r})$. Second one proves, by variational principle, that the exact n(r) is the one that minimizes the total ground state energy, $E[n(\boldsymbol{r})]$, which reads,

$$E[n(\boldsymbol{r})] = \int n(r)V_{ext}(\boldsymbol{r})\,d\boldsymbol{r} + F[n(\boldsymbol{r})] \qquad (2.3)$$

where the exact form of functional $F[n(\boldsymbol{r})]$ is unknown. Kohn-Sham (KS) formalism[69] rendered the theorem applicable to almost all materials by showing that there is a one-to-one correspondence between the real system with many-body electron interactions and a hypothetical non-interacting single-particle KS system, as long their $n(\boldsymbol{r})$'s are the same. Kohn and Sham put $F[n(\boldsymbol{r})]$ in a certain form such that its unknown part (exchangecorrelation (XC) functional, $E_{XC}[n(\boldsymbol{r})]$ is separated from the known single particle kinetic energy TS and electrostatic Hartree energy EH as,

$$F[n(\boldsymbol{r})] = T_s(\boldsymbol{r}) + E_H(\boldsymbol{r})[n(\boldsymbol{r})] + E_{XC}[n(\boldsymbol{r})] \qquad (2.4)$$

The KS formalism is exact but the accuracy of DFT depends on how accurately $E_{XC}[n(\boldsymbol{r})]$ can be approximated. It must account for all the effects that are not properly handled by single-particle KS equations; *e.g.*, the influence of Pauli Exclusion Principle and many body effects on electron motion. Among many different flavors, local density approximation (LDA) and generalized gradient approximation (GGA) are currently the most widely utilized XC-functionals[70]. However, when correlation effects are strong as in *3d-* metal oxides, the electrons which ought to be localized onto atoms are delocalized within DFT calculations. A way to correct this is separately treating the highly correlated electrons with an on-site Hubbard-U term. This method is called DFT+U (or LDA+U) and

is due to Anisimov.[71] We will utilize it with GGA and refer to it as GGA+U. This additional term energetically penalizes partial occupations and localizes electrons. While the value of U_{eff} can be approximated with a linear response approach,[72] it is usually treated as an empirical parameter fit to reproduce desired properties.

Since the experimental screening of a large number of materials can be a challenging and arduous task. Significant time and effort can be saved by using high-throughput computational techniques to predict and guide the selection of promising materials for the experimental evaluation.[73]

2.2.2 Voltage profile prediction using DFT calculations

The average lithiation/delithiation voltage (relative to Li/Li$^+$) corresponding to specific electrochemical reaction can be computed using the negative of the reaction free energy per Li added/removed, as shown in *Eq.* (2):[74]

$$V = \frac{\Delta G_f}{F \Delta N_{Li}} \tag{2.5}$$

where F is the Faraday constant, ΔN_{Li} is the amount of Li added/removed and ΔG_f is the (molar) change in free energy of the reaction. Considering a two-phase reaction between Li$_x$MO and Li$_y$MO: Li$_x$MO + (y - x)Li → Li$_y$MO, ΔG_f can be approximated by the total internal energies from DFT calculations neglecting the entropic contributions (0 K),

$$\Delta E = E\left(Li_y MO\right) - E\left(Li_x MO\right) - (y - x)E(Li_{metal}) \tag{2.6}$$

where $E(Li_x MO)$ and $E\left(Li_y MO\right)$ are the DFT energies at the respective compositions. The neglect of entropic contributions means that the lithiation voltage profiles will follow the T = 0K ground state convex hull and consist of a series of constant voltage steps along the two-phase regions of the convex hull, separated by discontinuities which indicate the

single phase compounds on the hull. It is worth mentioning here that, in practice, lithiation/delithiation do not necessarily proceed through two-phase reactions. Thus, the calculated T = 0K voltage profiles should be viewed as an approximation to the actual voltage profiles.[33] At finite temperatures (*e.g.*, room temperature), the voltage drops in the profile become more rounded , due to entropic effects.[17]

2.2.3 Mass transport and defect conductivity

The kinetic process at the atomic scale was examined by carrying out a point defect calculation in the bulk phases. The ionic conductivity for defect species i is defined as:

$$\sigma_i = C_i \, q_i \, \mu_i \tag{2.7}$$

where C_i is the charged defect concentration, q_i is the charge carried by the defect and μ_i is the defect mobility. Using the Arrhenius equation, the mobility is related to the activation energy E^{act} in the following equation:

$$\mu_i = \mu_{i0} \, exp(-E^{act} / k_B T) \tag{2.8}$$

The concentration C_i for a defect species i can be obtained using equation as follows:[75]

$$C_i = N_i^{site} N_i^{eqv} \, exp\left(-\Delta G_i^{form} / k_B T\right) \tag{2.9}$$

where N_i^{site} is the number of possible defect sites per unit volume and N_i^{eqv} is the number of equivalent ways to introduce the defect at a particular site. ΔG_i^{form} is the formation energy of the defect i. ΔG_i^{form} is equal to:

$$\Delta G_i^{form} = G_i^{def} - G^{pure} - \sum n_i^s \mu^s + q_i(\varepsilon_F + E_{VBM} + \Delta V) \tag{2.10}$$

where G_i^{def} is the energy of a supercell with this defect and G^{pure} is the energy of the supercell without any defect. $\sum n_i^s \mu^s$ is the total chemical potential of the defect; μ^s is the

chemical potential of an atom of type s and n_i^s is the number of atoms of s type in defect i.

$q_i(\varepsilon_F + E_{VBM} + \Delta V)$ corresponds to the energy to introduce (or remove) electrons while

creating of charged defects with charge state q_i and Fermi level ε_F referenced to the valence

band maximum, E_{VBM}, of the bulk material. ΔV term is an extra shift in the average

electrostatic potential, which aligns the VBM of defect supercells with the bulk VBM

caused by the finite size of the defect supercell.[75] The contribution from ΔV is negligible

due to the sufficient large supercell used in this study. The Fermi level is determined

considering the charge neutrality by solving equation (8):

$$\sum_i^{N_{\text{def}}} q_i C_i = 0 \tag{2.11}$$

where N_{def} is the total number of defects considered.

Vacancy sites are identified by considering symmetrically different

sites/configurations for specific atoms/clusters. Interstitial sites are generated using a

geometric method[76] by selecting voids in the structure. A radially decaying exponential

function is defined centered at each atomic site,

$$f_{ij}(\boldsymbol{r}) = \exp(-|\boldsymbol{r} - \boldsymbol{r}_{ij}^0|/a) \tag{2.12}$$

where $\boldsymbol{r}_{ij}^0$ is the vector corresponding to the Cartesian position of atom j in cell i and a is

the control factor for the rate of decay (default value: 0.25). For the whole crystal structure,

an overall function is defined as

$$F(\boldsymbol{r}) = \sum_i^{N_{cells}} \sum_j^{N_{atoms}} f_{ij}(\boldsymbol{r}) \tag{2.13}$$

where N_{cells} is the number of cells in the crystal structure and N_{atoms} is the number of

atoms in an unit cell. The summation is truncated by considering only those terms within

some absolute distance from $\boldsymbol{r}$ while excluded terms are negligible to a fixed tolerance.

Stationary points (local minima) of $F(\mathbf{r})$ with all three Cartesian derivatives equal to zero corresponds to the candidate interstitial sites.

We evaluate the defect mobility using kinetic Monte Carlo (KMC) simulations with the geometric and transition-state[77,78] energetic information gathered from Nudged Elastic Band (NEB) calculations.[79,80] The rate of jumps from site i to site j is calculated using

$$R_{ij} = v_{ij} \exp\left(- \Delta H_{ij}^{mig}/k_B T\right) \tag{2.14}$$

where v_{ij} is the attempt frequency and ΔH_{ij}^{mig} is the energy difference between ground and transition states at 0 K. We choose a uniform $v_{ij} = 10^{13}\ s^{-1}$ because is independent of temperature in the classical limit which would have negligible effect on the calculated activation energies.[78] The diagonal elements of the diffusivity tensor are calculated with

$$D_{\gamma\gamma} = \frac{\langle d_\gamma^2 \rangle}{2 \langle \Delta t \rangle} \tag{2.15}$$

where d_γ is the component of the displacement vector in γ direction ($\gamma = x, y, z$) and Δt is the simulation length. Averaging of d_γ and Δt are made over all simulations at certain temperature. Related simulations are performed until the standard error was less than 1% of the mean diffusivity at specific temperature with 10,000 jumps made in each simulation. Diffusivities are calculated with 10 K intervals using isolated defects in an infinite crystal to simulate the diffusion in the bulk situation. All the diffusion pathways between stable sites are enumerated. Climbing image NEB calculations were performed to find the barriers needed for the KMC simulations.

CHAPTER 3

Understanding the Non-Equilibrium Thermodynamics in Electrochemical

Conversion Reactions

3.1 Introduction

Many transition metal oxides and sulfides have been investigated in the past as conversion electrodes, in this work, we use Co_3O_4 and NiO as examples to examine the non-equilibrium thermodynamics in the electrochemical conversion reactions. As conversion-type electrode materials, Co_3O_4 and NiO can achieve a very high reversible capacity of >700 mAh/g.[81] Co_3O_4 and NiO are observed to lithiate at ~1.1 and 0.7 V (*vs.* Li/Li$^+$), respectively, with a large voltage hysteresis of >1.0 V during charge/discharge runs.[81] While exceptional reversible reactivities of Co_3O_4 and NiO have been achieved in previous experiments,[81–87] the underlying mechanism during the electrochemical process, and the source of the large hysteresis has not been fully understood. During the lithiation of Co_3O_4, it was observed that tetrahedral Co cations are displaced into neighboring empty octahedral sites while incoming Li ions occupy the remaining octahedral sites, producing an intermediate, rocksalt-based, non-equilibrium phase with a partial disordered (Li/Co) structure (*i.e.*, $LiCo_3O_4$).[83,88] Further lithiation of $LiCo_3O_4$ leads to a slow extrusion of cobalt at the octahedral sites.[83] The structural evolution beyond that point ($2 < x < 8$, $Li_xCo_3O_4$) is still unclear. The lithiation of NiO is initiated by a quick saturation of near-surface electroactive sites, followed by propagation of these lithiated phases ($Li_2O \cdot Ni$) into the bulk with a "finger-like" morphology.[89] The conversion-reaction decomposition of Co_3O_4 and NiO in the first cycle involves the

formation of amorphous/nano-sized metal (*e.g.*, Co and Ni, respectively) and lithia (Li_2O); no crystalline Co, Co_3O_4, Ni, NiO, or Li_2O were identified in fully lithiated samples. In subsequent cycles, the amorphous/nano-sized phases of the electrode are preserved.[90] It has been suggested that repeated decomposition and the formation of lithia is facilitated by the nanoscale dimensions and the catalytic activity of the transition metal particles.[86,91,92]

The large voltage hysteresis (> 1.0 V) between charge and discharge voltage profiles causes low cycling efficiency of conversion material electrodes and hinders their practical applications. Many efforts have been made to obtain a comprehensive understanding of the origins of the voltage hysteresis. Several hypotheses were suggested based on experimental and computational studies besides the well-known ohmic drop (typically on the magnitude of 0.1 V).[28] We summarize these hypotheses here: 1) *Nano effect* - Nanosized phases, as mentioned above, have been forming repeatedly during the electrochemical lithiation and delithiation of transition metal oxides. The cohesive energy of nanoparticles can be significantly lower than the bulk counterpart which can thereby affect the reaction voltages.[93] Doe *et al*.[32] reported a voltage drop around 0.4 V upon lithiation, assessed using a 1 nm spherical particle of bcc iron. However, we note that the overall effect on the voltage hysteresis of a complete cycle should be more limited since the nanosized phases are formed on both lithiation and delithiation and the voltage variations due to nanostructuring would presumably affect the charge/discharge voltage in the same direction. 2) *Distinct surface chemistries upon charge and discharge* - Khatib *et al*.[26] and Meggiolaro *et al*.[27] demonstrated that the surface reactions are different between the lithiation and delithiation of CoP and MgH_2. The corresponding reaction

energy difference contributes to the voltage hysteresis observed during the cycling of CoP (0.41 V) and MgH_2 (0.16 V). However, in the conversion electrodes of the present study the magnitude of voltage hysteresis is much larger, and it is unclear whether the surface reaction mechanism can account for such a large hysteresis. 3) *Compositional inhomogeneity caused by kinetic limitation* - Li *et al.*[28] and Wang *et al.*[94] proposed that the distribution of phases formed upon charge and discharge of FeF_3 could be different due to differences in diffusivity between Fe and F. As a result, a Li-deficient surface forms on charge while a Li-rich surface forms on discharge setting the system at different potentials versus Li^+/Li^0 and inducing a voltage gap. Therefore, the voltage hysteresis according to this mechanism should be largely alleviated when the particle size is sufficiently reduced, allowing for fast reaction kinetics. For transition metal oxides, however, the hysteresis is generally maintained regardless of particle morphologies, shapes, and sizes of the electrode materials.[38,95–99] 4) *Different reaction paths upon charge and discharge* - The substantial thermodynamic and kinetic disparities between charge/discharge reaction paths has the possibility to account for the large voltage hysteresis (> 1.0 V) observed in conversion oxides like Co_3O_4 and NiO. These disparate pathways have been found in other systems. Yu *et al.*[100] identified an intermediate phase during the conversion from $LiTiS_2$ to $Cu_{0.5}TiS_2$ while the re-conversion reaction exhibits simple two-phase features without any intermediate phase. Similarly, Chang *et al.*[36] found reaction path differences between the charge and discharge of Cu_2Sb. Boesenberg *et al.*[101] reported asymmetric pathways during cycling of NiO with the formation of a metastable intermediate phase on delithiation. The reaction path difference was then confirmed by Ponrouch *et al.*[102]

The conversion reaction of Li-MOs at room temperature involves a series of non-equilibrium phases that may be different from their thermodynamic equilibrium counterparts due to other kinetic constraints. Here, we develop a DFT-based methodology to determine the non-equilibrium and equilibrium phase evolution during the lithiation and delithiation processes of MOs, namely, Co_3O_4, NiO. We predict the corresponding lithiation and delithiation voltage profiles which show similar trends with the experimentally observed discharge and charge voltage curves. We propose that the large voltage hysteresis occurring in Co_3O_4 and NiO can predominantly be attributed to the dramatic difference in reaction pathways between a thermodynamically non-equilibrium lithiation and an equilibrium delithiation. These conversion-type electrodes, when used within the practical capacity thresholds, are predicted to have improved cycling stability and lower voltage hysteresis.

3.2 Methodology

3.2.1 Density functional theory calculations

All DFT calculations were carried out in the Vienna Ab-initio Simulation Package (VASP)[103–106] with the projector augmented wave (PAW) potentials.[107] The generalized gradient approximation (GGA) of Perdew-Becke-Ernzerhof (PBE)[108] was used for the exchange-correlation functional; also, all calculations are spin polarized. We used a cutoff energy of 520 eV for the plane-wave basis set and Γ-centered k-meshes with the density of 8000 k-points per reciprocal atom in all calculations. We used the DFT + U method with onsite U parameters to treat the $3d$ electrons of Co and Ni ions. The U values of 3.3 eV and 6.4 eV were adopted for Co and Ni ions, similar to previous studies by fitting

the experimental and calculated formation enthalpy.[109–116] Ferromagnetic (FM) and antiferromagnetic (AFM) spin-polarized configurations were used for Co_3O_4 and NiO respectively since NiO is known to display the antiferromagnetic (AFM) ground states below a Néel temperature of 523 K.[117]

3.2.2 Construction of Li-M-O ternary phase diagrams and ground state reaction paths

Phase diagrams represent the thermodynamic phase equilibria of multicomponent systems and reveal useful insights on the processing and reactions of materials. Nevertheless, the experimental determination of a phase diagram can be extremely time and labor consuming which requires dedicated synthesis and characterization of all phases in the target system. Computational tools like DFT can accelerate phase diagram constructions remarkably.[118,119] By calculating the DFT energies of all known compounds in a chemical system, we can determine the T=0K phase diagram, or ground state convex hull, of that system. Here in this study, we constructed ternary Li-M-O (M=Co, Ni) convex hulls using the structures with the lowest energy at each composition. The structures were adopted from the Inorganic Crystal Structure Database (ICSD).[120] The reference states (Li, Mn, Ni, non-solid O_2) were obtained by fitting to experimental data from the SGTE substance database (SSUB) and IIT.[112,114,121–124] Calculations to construct equilibrium Li-M-O (M=Co, Ni) phase diagrams were carried out within the Open Quantum Materials Database (OQMD) framework.[113,114] All the stoichiometries labeled on the phase diagram are part of the ground state convex hull, indicating that these compounds are stable and have lower energy than any linear combination of other

compounds that add up to the same composition. The tie-lines and phase regions in a ternary phase diagram indicate the coexistence of two and three phases, respectively. The equilibrium lithiation/delithiation reaction paths can be determined directly from the ground state convex hull between Li and MOs which is obtained using a linear programming approach.[118]

3.2.3 Non-equilibrium Phase Searching method

Though the equilibrium lithiation pathway can be simply determined from the ground-state convex hull, determining a non-equilibrium reaction pathway is much more difficult, because there is no general, simple guiding principle to determine this pathway. To simulate the non-equilibrium lithiation process (*i.e.* energetically above the equilibrium reaction pathway) of the MOs, we designed a structure-based, mechanistic method namely NEPS (Non-equilibrium Phase Searching method) to search for intermediate phases (Figure. 3.1) by exploring geometrically distinct Li/vacancy configurations on possible insertion sites of MO structures at different compositions (Li/vacancy ratios). An assumption is made based on previous non-equilibrium (de)lithiation studies[36,100] that Li ion diffusion in the transition metal oxide is significantly faster compared to diffusion of the transition metal ions and oxygen ions during the lithiation reaction. Our hypothesis, therefore, is that Li ion(s) inserted into a compound can find the lowest energy empty site(s) for any given arrangement of transition metals and oxygen ions. The positions of the transition metal ions and oxygen ions respond to the presence of the Li only *via* local relaxation, enabling the non-equilibrium lithiation process. Our computational method involves, the following five steps, described below:

i) Starting with the host compound (which may or may not contain Li), identify all possible insertion sites. The method is initiated by searching for interstitial sites in the original transition metal oxide structures. An in-house code MINT (openly available on GitHub)[76,80,125,126] was used which automates the search for insertion sites. The algorithm works by placing an analytic, exponential decaying function (Exp[-r/a]) at each atomic site and searching for geometric minima in the resulting function. An illustration of the utility of MINT to find interstitial sites in a complex crystal structure is given in Ref. ([76]) for the problem of defects and mass transport in $B_{20}H_{16}$. Models with different sizes of supercell were then built with all the empty insertion sites identified.

ii) Generate all symmetrically distinct configurations for Li insertion. We worked with the Enum code[127–129] to generate all symmetrically-distinct configurations of Li on the unoccupied sites. All configurations were classified according to their composition $Li_x \bullet_{1-x} MO$.

iii) Compute total energies of all configurations generated in step ii). To enable a fast energy sampling, simple point-charge electrostatic calculations were conducted, using nominal charge states for the ions in the system.[76]

iv) Select the structures with lowest electrostatic energies to be computed more accurately and atomically-relaxed in DFT. For each composition, the structures were ranked by the electrostatic energies, and the three lowest energy structures were further relaxed using DFT. The formation energies for these selected structures were evaluated according to the following reaction: $MO + xLi^+ \rightarrow Li_xMO$.

v) Using all of these non-equilibrium structures derived from insertion of Li into the initial TM oxide, build the "non-equilibrium convex hull" and determine phases. For

each specific system (Li-MO), we build the corresponding non-equilibrium convex hulls with the calculated formation energies at all compositions. The compositions, structures, energies located on the convex hull correspond to the identified non-equilibrium phases.
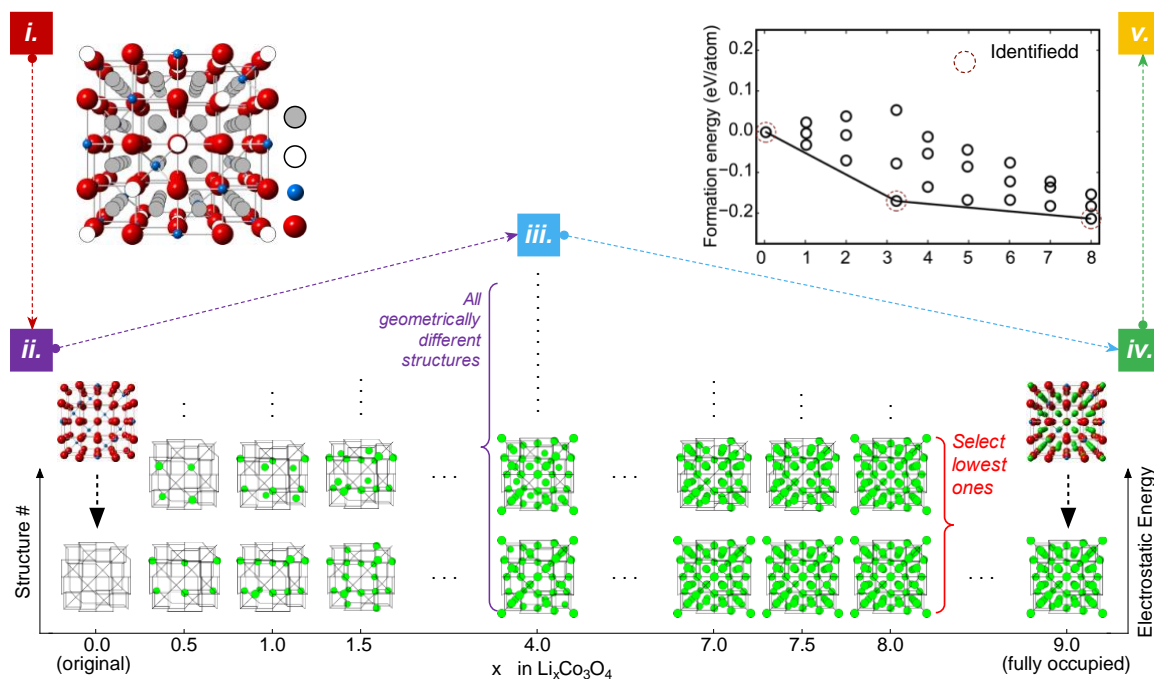
Figure 3.1 Searching for the non-equilibrium phases through the Li-TMO reactions: An example of Li-Co$_3$O$_4$. The searching process proceeds as follows: (i) Possible insertion sites (T$_d$ and O$_h$) were identified from the original Co$_3$O$_4$ spinel structure. (ii) All symmetrically-distinct configurations of Li on the unoccupied sites were generated for each composition using Enum (Li/vacancy orderings are shown by the green circles with the Co$_3$O$_4$ structure visualized by lines).[127–129] (iii) Total energies of all the configurations generated were sampled using electrostatic calculations. (iv) For each composition, corresponding structures were ranked by the total energies, and the three lowest energy structures were further relaxed using DFT. The formation energies for these selected structures were then evaluated. (v) Using formation energies obtained, the non-equilibrium Li-Co$_3$O$_4$ convex hull is built. The composition points located on the convex hull then correspond to the identified non-equilibrium phases.
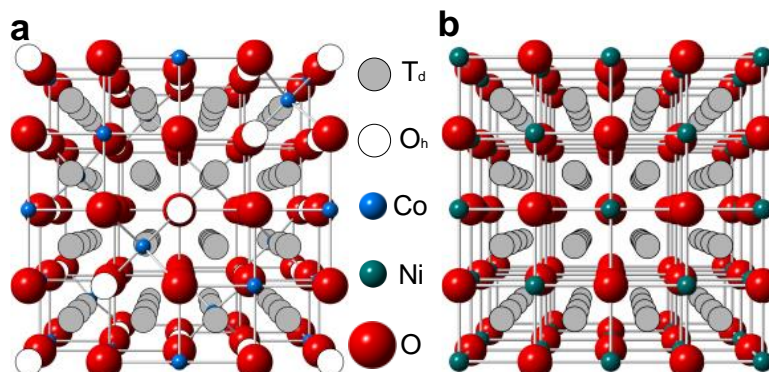
Figure 3.2 Chemical structures of (a) Co_3O_4 (Fd-3m) and (b) NiO (R-3m). All the unoccupied T_d and O_h sites can be used as an insertion site for lithium ions. The dark blue, green, and red circles represent Co, Ni, and O, respectively with grey and white circles represent T_d and O_h vacancy sites within the host structure.

For Co_3O_4, we used a supercell containing 6 Co ions (4 Co^{3+}, 2 Co^{2+}) and 8 O^{2-} ions, which has 16 total tetrahedral and octahedral unoccupied sites that Li ions can insert as shown in Figure 3.2. As mentioned in the introduction, the lithiation of Co_3O_4 is accompanied by the displacement of tetrahedral Co cations into neighboring empty octahedral sites. We considered the energetic influences on the Co ion migration to the octahedral site[83] by creating three initial Co_3O_4 configurations, as shown in Figure 3.3. Figure 3.3a represents the original spinel Co_3O_4 structure (with Co occupying both tetrahedral and octahedral sites in a 1:2 ratio); and Figures 3.3b and 3.3c represent structures where half and all of the tetrahedral Co ions are moved to octahedral sites, respectively. Particularly for the $LiCo_3O_4$ phase which is reported to have all Co ions migrated to the octahedral sites randomly, we reproduce the partially disordered structure using the special quasi-random structure (SQS) method by populating the metal sites with

Co and Li randomly. An SQS was generated based on a Monte Carlo algorithm implemented in ATAT[130–133] with the constraint that the pair and triplet correlation functions of the SQS are identical to those of the statistically random Co/Li population of cation sites at least up to the third nearest neighbor. Starting from these structures shown in Figure 3.3, we insert the Li atom(s) into the unoccupied octahedral and tetrahedral site(s) for a range of compositions within $0 < x \leq 8$ for $Li_xCo_3O_4$.

For NiO, we used a supercell containing 8 Ni^{2+} ions and 8 O^{2-} ions, which has 16 total tetrahedral unoccupied sites where Li^+ can insert as shown in Figure 2.2. We insert the Li atom(s) into the unoccupied tetrahedral site(s) in Figure 3.2b to generate Li_xNiO ($0 < x \leq 2$) structures.

a   **b**   **c**

Original Co_3O_4 Co_3O_4 w/ 1/2 Co Co_3O_4 w/ all Co
                     $(T_d) \rightarrow O_h$ sites $(T_d) \rightarrow O_h$ sites

● Co   ● O
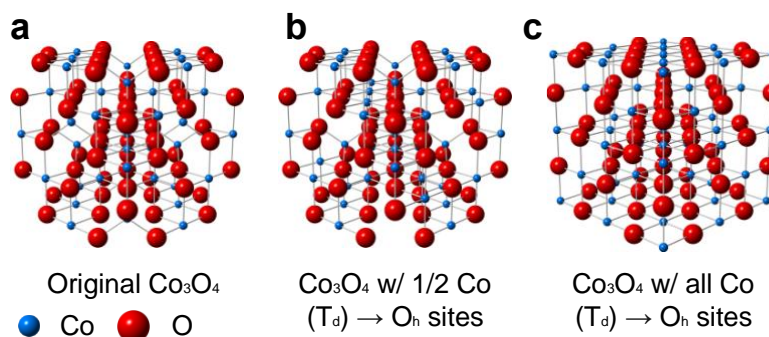
Figure 3.3 Three initial configurations for the searching of $Li_xCo_3O_4$ non-equilibrium phases. (a) Original Co_3O_4, (b) Co_3O_4 structure with 1/2 T_d Co atoms are migrated from T_d sites to O_h sites, and (c) Disordered Co_3O_4 structure with all T_d Co atoms are migrated to O_h site.

3.3 Results and discussion

3.3.1 Li-M-O (M = Co, Ni) ground state convex hulls and equilibrium (de-)lithiation voltage profiles

We begin with the calculation of equilibrium (de)lithiation pathways, given by the equilibrium convex hull construction. The ternary Li-Co-O and Li-Ni-O ground state convex hulls are presented in Figure 3.4 with stable compositions marked by filled circles. Stability of compounds on the convex hull indicates that they have a lower DFT energy than any linear combination of other compounds (which are contained in the OQMD database). Compositions marked with an "×" are the non-equilibrium phases identified in Section 3.2.3 inside a stable three-phase region or on the two-phase tie-line which have higher energy than a mixture of the three/two compounds that define the triangle/tie-line. Although such compounds are thermodynamically unstable, they can be non-equilibrium if kinetic limitations (*e.g.*, diffusion, nucleation) prevent the relaxation of the system to the equilibrium, stable phases.[31]

Table 3.1 Lithiation reactions of the equilibrium path of Co_3O_4 and NiO.

Region	Reaction	Capacity [mAh/g]	Voltage [V]
I	$Co_3O_4 + Li \rightarrow LiCoO_2 + 2CoO$	111	2.53
II	$LiCoO_2 + 2CoO + Li \rightarrow 1/3Li_6CoO_4 + 8/3CoO$	223	1.82
V	$1/3Li_6CoO_4 + 8/3CoO + 4Li \rightarrow Li_6CoO_4 + 2Co$	668	1.81
IV	$Li_6CoO_4 + 2Co + 2Li \rightarrow 4Li_2O + 3Co$	890	1.66
I	$NiO + Li \rightarrow 1/2Li_2NiO_2 + 1/2Ni$	359	1.75
II	$1/2Li_2NiO_2 + 1/2Ni + 1Li \rightarrow Li_2O + Ni$	718	1.71

The equilibrium lithiation reaction paths of MOs go through multiple three-phase regions in Figure 3.4 consisting of the stable phases marked in our ternary phase diagrams.

These regions correspond to various lithiation reactions listed in Table 3.1, where we calculate the capacities and average voltages of these reactions. In Figure 3.3, we compare the equilibrium reaction voltage profiles predicted with DFT with the experimental voltage profiles adapted from *Refs*. [[81,82,134]]. We note that the overall values of the calculated equilibrium voltage profiles of Co_3O_4 and NiO with DFT reasonably agree with the experimental *delithiation* curves (Figures 3.5a-b). Therefore, we conclude that the delithiation of $Li_8Co_3O_4$ ($4Li_2O \cdot 3Co$) and Li_2NiO ($Li_2O \cdot Ni$) follow pathways which are energetically close to the equilibrium reaction processes. There is a voltage difference between the calculated equilibrium profile and experimental curve at the beginning of the delithiation. Many factors (*e.g.* entropy, reaction kinetics, compositional inhomogeneity, *etc.*) can contribute to this voltage difference. Yet detailed investigation on clarify the energetically dominant factor is beyond our current scope. However, for Co_3O_4 and NiO, the calculated equilibrium voltage profiles are much higher compared to the *lithiation* plateaus at 1.1/0.7 V as shown in Figure 3.3a-b. These voltage differences reflect the large voltage hysteresis during the cycling of Co_3O_4 and NiO and suggesting an alternative reaction path for the lithiation processes. As a result, we focus on the non-equilibrium lithiation pathways involving intermediate structures as an explanation of the discrepancies between experimental lithiation and calculated equilibrium voltages.
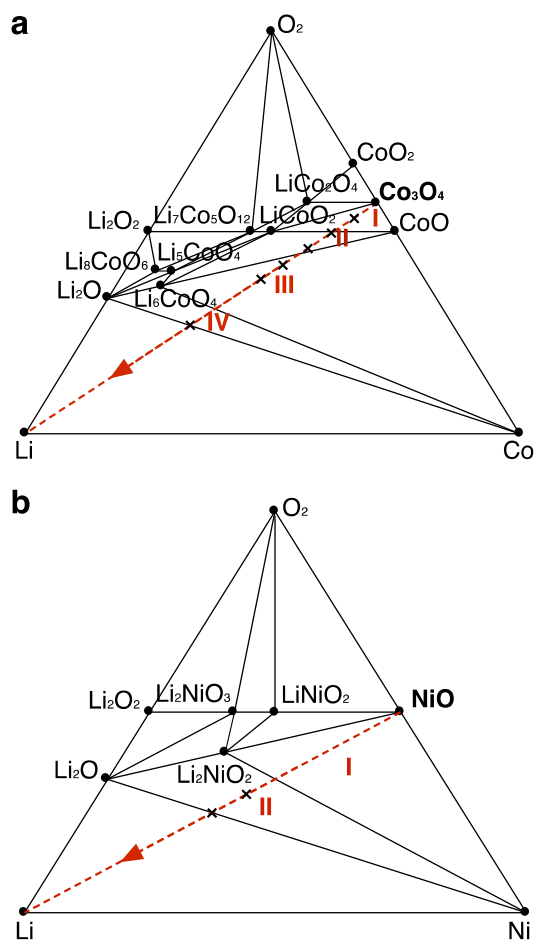
Figure 3.4 The Li-M-O phase diagrams and equilibrium lithiation/delithiation paths of (a) Co_3O_4 and (b) NiO. The equilibrium reaction paths are represented by the dotted line. The three-phase regions which lithiation/delithiation path goes through are marked by Roman numerals. Compositions marked with an "×" are the non-equilibrium phases identified in Section 3.2.3.
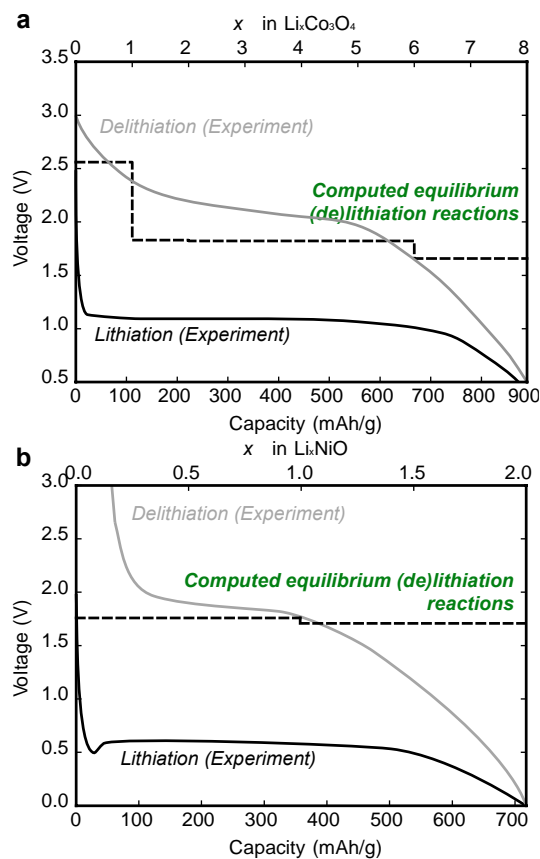
Figure 3.5 Calculated equilibrium lithiation/delithiation voltage profiles for (a) Co_3O_4 and (b) NiO and experimental voltage profiles adapted from *Ref*. [81,82,134]. The overall values of the calculated equilibrium voltage profiles of Co_3O_4 and NiO reasonably agree with the experimental delithiation curves. The experimental lithiation/delithiation profiles are represented by the black and grey curves.

3.3.2 Non-equilibrium lithiation voltage profiles

Since the lithiation voltages from experiments exhibit large differences with the equilibrium voltage profile (Figure 3.5), we investigate the non-equilibrium lithiation process of MOs by the prediction of non-equilibrium structures and reaction pathways based on geometrical enumerations (the methodology is detailed in *Section 3.2.3*). During the lithiation process of Co_3O_4 and NiO, we identify several non-equilibrium phases

($Li_xCo_3O_4$, x = 1, 2, 3, 4, 5, 8 and Li_xNiO, x = 1.625, 2) along the Li-Co_3O_4(NiO) "non-equilibrium convex hulls" as shown in Figure 3.6a and 3.6c. Using these non-equilibrium phases, the overall voltages of calculated "non-equilibrium" lithiation reactions (Figure 3.4b and 3.4d) are in significantly better agreement with experimental lithiation voltages than the calculated equilibrium values.[81,82] Because our voltages are based on T=0K energetics, the shape of the calculated voltage profile is a series of constant voltage reactions with steps in between. However, the experimental curves are generally more smooth and continuous. It is noteworthy that the simulated voltage profiles will generally become more smooth when entropic considerations and finite temperature[17] is taken into account. The comparison of calculated voltages and structural information with experiment (electrochemical, XRD, and EXAFS) lead us to the conclusion that the lithiation of Co_3O_4 and NiO follows a series of non-equilibrium phases instead of the ground state equilibrium phases in Tables 3.1. The structural validation and comparison with experiment will be discussed in following sections. Additionally, discharge voltage curves of certain conversion-type materials could be affected by many different experimental aspects, including synthesis method, particle morphology, test settings, etc. Particularly for Co_3O_4 and NiO, the lithiation voltage profiles of various nano particles[38,98,135–137] demonstrate continuously decreasing trends in contrast to the largely flat profile obtained using bulk materials as shown in Figure 3.6. However, exploring for the detailed reasons behind these nano- vs. bulk experimental voltage curves is beyond the scope of this study.
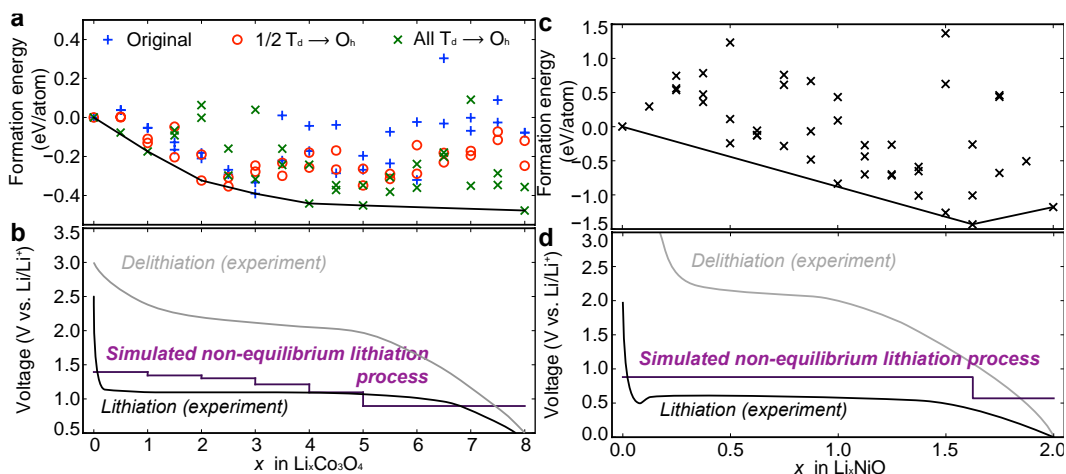
Figure 3.6 Convex hulls generated with all the calculated non-equilibrium phases for (a) Co_3O_4 and (b) NiO, and the corresponding voltage profiles of the Li insertion into (c) Co_3O_4 and (d) NiO. Predicted non-equilibrium reaction voltage profiles fall into the experimental lithiation voltage intervals.

3.3.3 Atomistic structural evolutions during the non-equilibrium lithiation process

Co_3O_4

We next look into the atomistic phase evolution during the non-equilibrium lithiation process. The lithiation of Co_3O_4 starts with both Li and Co (migrated from the T_d sites) taking the unoccupied O_h sites. As all the O_h sites are fully occupied by Li and Co at $x = 1$, the resulting $LiCo_3O_4$ phase adopts a partially disordered (Li/Co) rocksalt structure (Figure 3.7b), as observed by Thackeray *et al*. through X-ray diffraction analysis.[83] In the following step ($x = 2$) in Figures 3.7c, continuing Li ion insertion forces the octahedrally-coordinated cobalt ions in $LiCo_3O_4$ to migrate back to tetrahedral sites in $Li_2Co_3O_4$. A mosaic structure (Figure 3.7c) forms at this step with localized CoO-Li_2O character and Co ions occupy both T_d site and O_h sites confirming the X-ray diffraction analysis conducted for $Li_{1.92}Co_3O_4$ by Thackeray *et al*..[83] With further Li intercalation (*x*

= 3), we observe in Figures 3.7c that the oxygen *fcc* frameworks still stay intact. To better understand the atomistic reduction of ions in the cells, we conduct Bader charge analysis[138,139] for Co ions in intermediate phases (Figure 3.8a). We also monitor the interatomic distance between selected nearest neighbor ions through the lithiation process, as shown in Figure 3.8b. From Co_3O_4 to $Li_3Co_3O_4$, the Bader charge of Co decreases for -0.44e indicating the Co ion reduction ($Co^{3+} \rightarrow Co^{2+}$). Co-Co, and O-O interatomic distances in Figure 3.8b show limited changes indicating the overall preservation of the backbone of the structure. These observations indicate the potential to use Co_3O_4 as a reversible, intercalation-type electrode in a constrained lithiation range ($0 < x < 3$).

a

Co migration

b

partially ordered

Intercalation

c

CoO Li_2O

d

Co_3O_4 (Original) $LiCo_3O_4$ (Rocksalt) $Li_2Co_3O_4$ (Mosaic structure) $Li_3Co_3O_4$

O_h sites

T_d sites

Co

Li

O

g

Co Li_2O

f

Co gathering Li/O congregating

e

Co-O coordination #decreasing

$Li_8Co_3O_4$ ($4Li_2O \cdot 3Co$) $Li_5Co_3O_4$ $Li_4Co_3O_4$
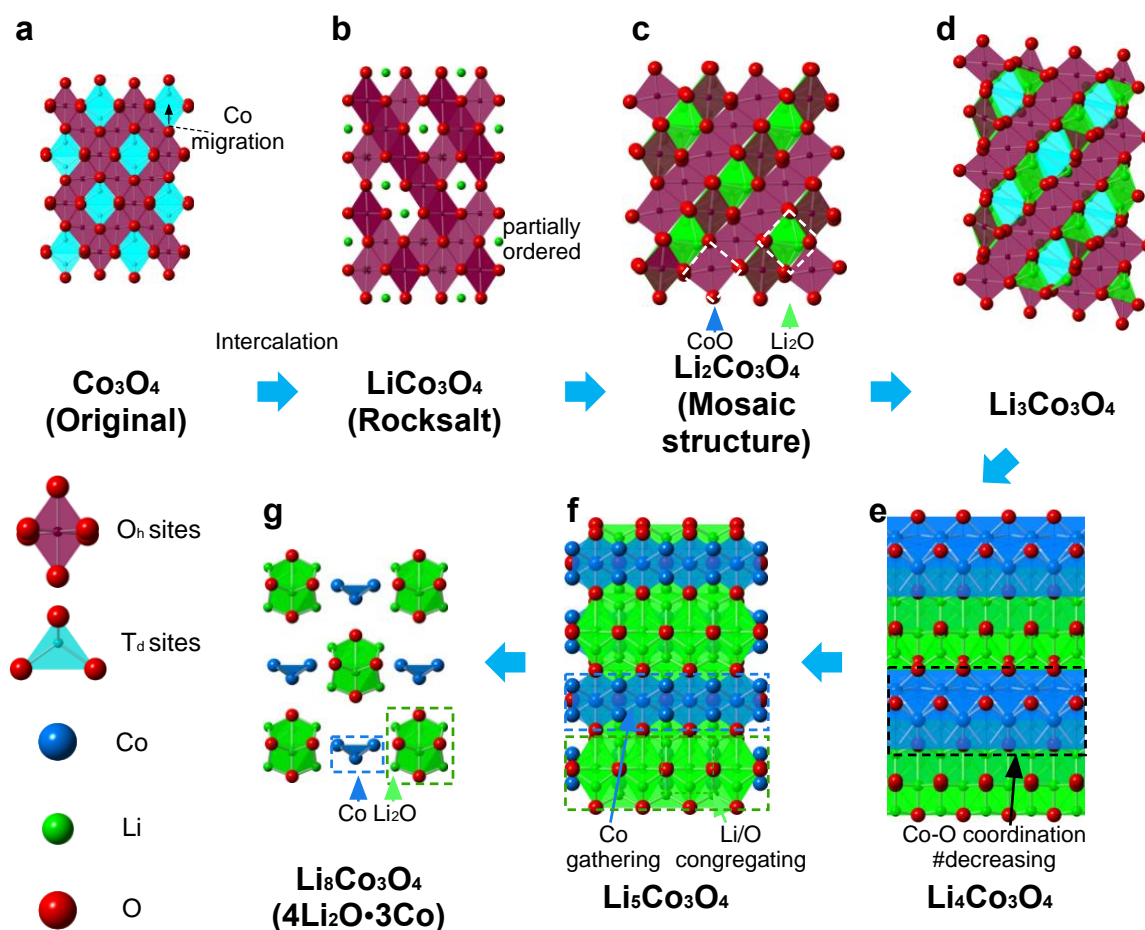
Figure 3.7 Structures of the non-equilibrium phases on the convex hull and the corresponding phase evolution. At the beginning of the lithiation, both inserted Li and Co ions from the T_d sites tend to occupy the empty O_h sites forming $LiCo_3O_4$ as shown in Fig. 3.7b (Co movements are indicated by black arrows). Furthermore, it is observed that the oxygen *fcc* array starts to be distorted in Fig. 3.7c. In $Li_4Co_3O_4$, the Co-O coordination numbers are decreasing (labeled by the green rectangle) [Fig. 3.7e], followed by the Li/O congregating (green rectangle) and Co gathering (blue square) in Fig. 3.7f. Lastly, we observe the formation of Li_2O and Co clusters, *i.e.* a strong tendency to phase separate into ground-state phases at that composition, which is consistent with previous experiments.[82,90]

Beyond the intercalation-type reaction ($x \geq 4$), Co ions start to get partially reduced to their metallic oxidation state ($Co^{2+} \rightarrow Co^0$, Fig. 3.8a) and begin to be extruded from the structure. Co ions in these non-equilibrium structures begin to cluster and Li/O also start to congregate as the system approaches the $x = 5$ $Li_5Co_3O_4$ phase in Figure 3.7f. The lithiation now starts to resemble a pathway closer to the conversion-type reaction. When the Co_3O_4 is fully lithiated ($x = 8$), Co ions have been fully reduced to Co metal; and Li ions combine with O ions to form a distorted Li_2O. We observe that in this highly lithiated state, the Co clusters distribute in an alternate layer of distorted Li_2O in Figure 3.7g, which in an indication of the phase separation tendency between nanoscale Co metal and lithia. We consistently observe that the distances between neighboring Li-O and O-O ions in Figure 3.8 approach the typical bond lengths in Li_2O while the Co-Co distances get close to that of Co metal, which validates the experimental observation of Co nanoparticles dispersed in the disordered Li_2O in previous studies.[82,90] Our results have demonstrated that only Li_2O is forming and no other products such as Li_2O_2 or LiO_2 are observed during the lithiation process (Figure 3.8b). We have compared our calculated Co-Co interatomic

distances during lithiation with the values measured by extended x-ray absorption fine structure method (EXAFS).[86,140] The predicted Co-Co distance show reasonable agreement with the experimental EXAFS observations across a range of Li concentrations, further validating our lithiation pathway results (Figure 3.8b).
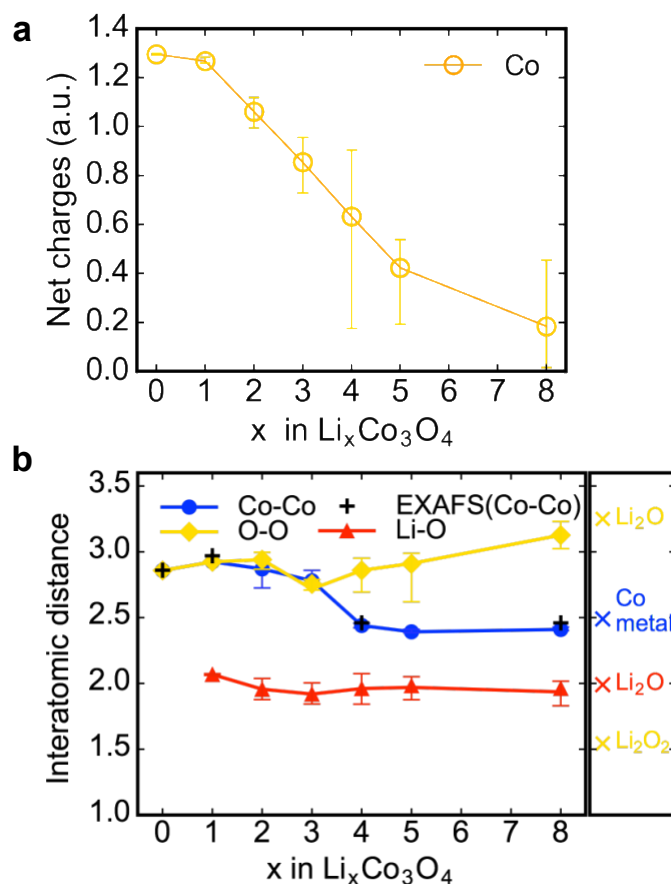
Figure 3.8 (a) Averaged net charges on Co in $Li_xCo_3O_4$, $(0 < x < 8)$ based on the Bader charge analysis. The error bar corresponds to the distribution (maximum and minimum) of charges on the Co ion. (b) Interatomic distance during the lithiation process of Co_3O_4. The error bar corresponds to the distribution (maximum and minimum) of interatomic distances. EXAFS data on Co-Co interatomic distance is adapted from *Ref.* [86,140]. Typical interatomic bond lengths (adapted from *Ref.* [141,142]) are also provided in the figure (right).

NiO

Unlike Co_3O_4, the lithiation of NiO starts with conversion-type features. When lithiation begins, Li ions go into the T_d interstitial sites of the NiO structure (Figure 3.9). After 1.6 Li are inserted, Ni^{2+} ions have been largely reduced to Ni^0 metal atoms as shown by Bader charge analysis (Fig. 3.10a). And, the system reaches its first non-equilibrium phase characterized by alternative layers of distorted Ni and lithia. The variation of Ni-Ni interatomic distance as a function of x in Figure 3.9b confirms the changes in the oxidation state of Ni ($Ni^{2+} \rightarrow Ni^0$). Some of the Ni ions are still bonded with oxygen ions with a narrow distance between them (Fig. 3.10b). When 2 Li are inserted, all the Ni ions are reduced to Ni^0 with lithia forming single layers implying the phase separation between nanoscale Ni metal and lithia (Fig. 3.9c). Again, only Li_2O is formed and no other products such as Li_2O_2 or LiO_2 are observed during the lithiation process (Figure 3.10b). Similar to Co_3O_4, the predicted Ni-Ni distance show remarkable agreement with the experimental observations as a function of Li concentration (Figure 3.10b).[101] Using *in-situ* TEM observations,[89] He *et al.* reported the lithiation of NiO penetrates into the material through a "finger-like" morphology. The lithiation "fingers" that propagate into the sample are in the form of high-aspect-ratio lithia and Ni^0 layers, and our non-equilibrium pathway calculations feature precisely this type of morphology and hence help explain the experimental observations. Here we propose that the development of the fingers is enabled by the formation and growth of the non-equilibrium intermediate phases Li_xNiO (1.625 < x < 2.0) featured with lithia and Ni metal layers. The experimental identification of the non-equilibrium intermediate phases is under investigation.[143]
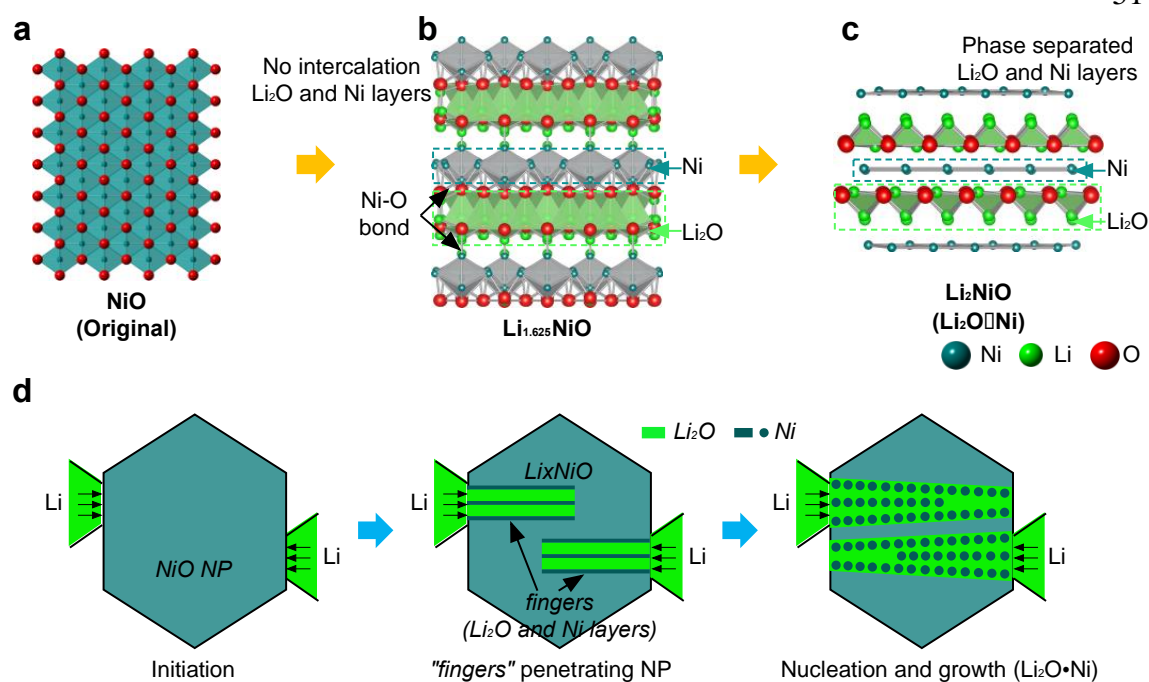
Figure 3.9 Structures of the two non-equilibrium phases on the convex hull and schematic illustration of the "finger" lithiation mechanism of NiO.[89] The lithiation of NiO starts with conversion-type features and Li ions go into the T_d interstitial sites of the NiO structure. After 1.625 Li are inserted, Ni^{2+} ions have been partially reduced the Ni^0 metal atoms. The system reaches the first non-equilibrium phase characterized by alternative layers of distorted Ni and lithia shown in Fig. 3.9b. Some of the Ni ions are still bonded with oxygen ions with the narrow distance between them. When the 2 Li are inserted, all the Ni ions get redox by Li with lithia structures getting more regular and Ni metal atoms forming single layers implying the phase separation between nanoscale Ni metal and lithia (Fig. 3.9c). The non-equilibrium phases featured with alternative layers of lithia and Ni can be used to explain the "finger" lithiation mode of NiO.
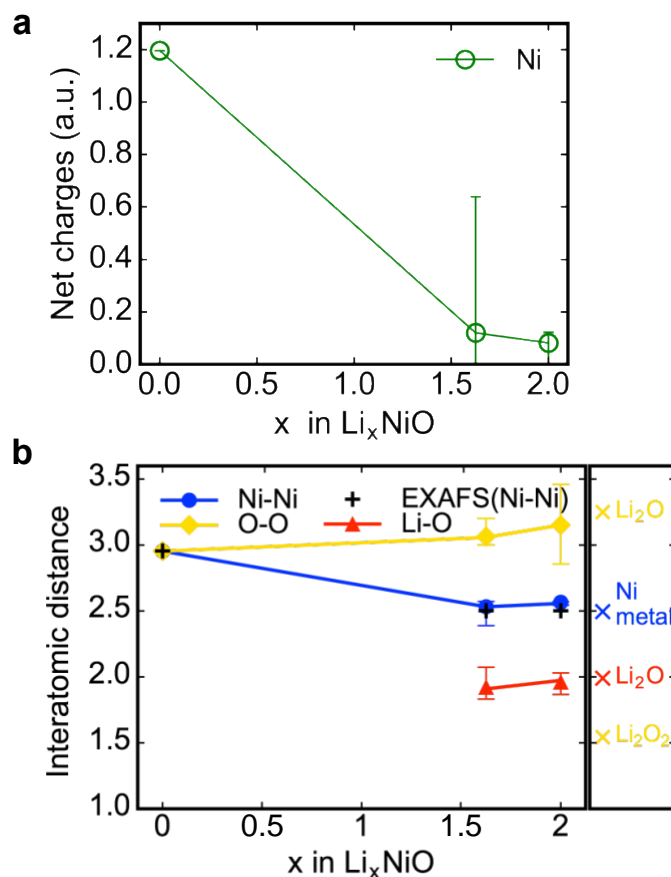
Figure 3.10 (a) Averaged net charges on Ni in Li_xNiO, $(0 < x < 2)$ based on the Bader charge analysis. The error bar corresponds to the distribution (maximum and minimum) of charges on the Ni ion. (b) Interatomic distance during the lithiation process of NiO. The error bar corresponds to the distribution (maximum and minimum) of interatomic distances. EXAFS data on Ni-Ni interatomic distance is adapted from *Ref.* [[101]]. Typical interatomic bond lengths (adapted from *Ref.* [[141,142]]) are also provided in the figure (right).

As described above in section 3.3.2 and 3.3.3, the final non-equilibrium phases after full lithiation of Co_3O_4 and NiO are composed of nanoscale Co, Ni, and Li_2O clusters, and we assert that the reverse delithiation process will proceed at a potential closer to the equilibrium voltage profile. Since the Co/Ni/Li_2O clusters are very closely integrated into the nanoscale with high interfacial area, they will still be at a higher energetic state

compared with the bulk phase (where these clusters can exist on a much larger length scale with lower interfacial energy). Once the electrode is fully delithiated back to the original Co_3O_4 or NiO structure, the non-equilibrium lithiation process will start again. There is voltage difference between the calculated equilibrium profile and experimental curve at the beginning of the delithiation which disappear after the first plateaus when all Li_2O get decomposed as shown in Tab 3.1. It can be readily understood since the replacement of Li from Li_2O by TM generally requires much lower voltage compared to the Li extraction from Li_xTMO_y with or without concurrent TM oxidation. By determining the lithiation/delithiation reaction paths, our theoretical study now provides an insight to the large voltage hysteresis observed during the cycling of Co_3O_4 and NiO.[81,82,90] The distinct reaction pathways between the lithiation and delithiation process induce the large voltage hysteresis.

Specifically, during the lithiation of Co_3O_4, the oxygen *fcc* frameworks start to collapse after four Li ions inserted ($x \geq 4$), as displayed in Figures 3.7e. We hypothesize that if only 3 lithium units are inserted into the Co_3O_4 electrode, the lithiation process may proceed as an intercalation reaction with the oxygen backbone still preserved yet with Co migration in the structure, which may offer an enhanced cyclability with a capacity of ~334 mAh g^{-1} and much more constrained volume expansion. It is also possible that the following delithiation process may proceed with the intercalation-type reaction that may prevent the voltage hysteresis and particle cracking.

There have been studies using the confinement of multiple nano-scale NiO layers within an electrode to direct lithium transport and reactivity.[87,144] The layered features of the non-equilibrium phases predicted in this work (Fig. 3.9b, c) during the lithiation of

NiO rationalize the design of the multi-nano-layer electrode and also offer guidance on its further improvement. With the advancement of the synthesis at the nanoscale, we assert that enhanced reactivity and reversibility could be achieved when the single NiO layer thickness approaches the counterpart of Ni/Li$_2$O dual layers in our computed non-equilibrium phases (~10 Å). In this case, the corresponding (de)lithiation would therefore require only Li, Ni and O ion migration within extremely limited length scales and only in a layered morphology, showing the possible use of these nanoscale materials as a fast rate electrode material.

3.4 Conclusion

We have combined first-principles calculations of equilibrium and non-equilibrium structures derived from the original MOs (Co$_3$O$_4$, NiO) structures to explain the underlying mechanisms of lithiation and delithiation of these conversion electrodes in Li-ion batteries. A structure-based method was designed to search for non-equilibrium intermediate phases by exploring geometrically distinct Li/vacancy configurations on possible insertion sites of MO structures at different compositions (Li/vacancy ratios). For Co$_3$O$_4$ and NiO, the overall value of equilibrium voltage profiles (~ 2.1 V and 1.74 V) reasonably agree with the experimental delithiation voltages, however, they show large deviations from the experimental lithiation counterparts (~ 1.1 V and 1.2 V) reflecting the large voltage hysteresis during cycling. We focus on the voltage deviations caused by the nonequilibrium lithiation process by searching for possible non-equilibrium phases that appear in the lithiation reactions. For Co$_3$O$_4$, we have identified non-equilibrium phases where the first three phases (x = 1, 2, and 3) preserve a nearly rigid oxygen *fcc* framework. Therefore, we

assert that Co_3O_4 should have enhanced reversibility as an electrode when the charge/discharge is limited to 3 moles of Li per formula unit or less. Even with this restriction, this material could offer better cyclability at a reasonable capacity of ~334 mAh g^{-1}. For NiO, we have identified non-equilibrium phases (Li_xNiO, $x = 1.625$ and 2) both of which are characterized by alternative layers of distorted Ni and lithia. The overall voltages of calculated lithiation/delithiation profiles using energetics of these non-equilibrium/equilibrium phases show good agreement with experimental voltages and explain the large voltage hysteresis during Co_3O_4/NiO cycling. Our study provides new insights on the lithiation process of transition metal oxides and could help future experiments to overcome the current limitations of the conversion-type electrode materials promoting the development of more advanced LIBs.

CHAPTER 4

Revealing the Conversion Mechanism of Transition Metal Oxide (Sulfide) Electrodes

4.1 Introduction

Based on what we have learned from these systems, we continue our research on applying the Non-Equilibrium Phase Searching method as designed to other transition metal oxides/sulfides in order to obtain a more general understanding of the detailed mechanism for conversion materials during charging and discharging. Together with experimental efforts, we attempt to reveal the conversion mechanisms of additional transition metal oxides and sulfides such as $(Cu,Co)_3O_4$, CuS, and MoS_2. Our study could help future experiments to overcome the current limitations of the conversion-type electrode materials and promote the development of more advanced LIBs

4.2 $(Co,Cu)_3O_4$

4.2.1 Introduction

Unlike intercalation/de-intercalation reactions, conversion and alloying reactions induce large volume changes during charge/discharge cycles that often lead to fracture and loss of electrical contact, among other deleterious mechanical effects of volume change.[145−148] The resulting loss of electrical contact to active electrode materials is one of the main causes of capacity loss and reduced Coulombic efficiency. In addition, most electrode materials for conversion and alloying reactions are semiconductors (and even insulators) that possess relatively low electronic conductivity. Thus, improved

electrical conductivity would also improve the prospects of conversion and alloying reaction materials in Li-ion and related battery applications.

Metallic Cu is often used as the current collector at the anode in batteries due to its high electrical conductivity. Metallic Cu can also be mechanically stretched or bent significantly and repeatedly without fracture due to its high ductility and malleability. It has been demonstrated that incorporation of a third element into metal oxides/fluorides can greatly improve the cycling stability.[94] Combined with experimental proofs,[39] we show here that by substituting a small amount of Cu into a Co_3O_4 lattice uniformly, the resulting composite electrode material ($Cu_{3/7}Co_{18/7}O_4$) can endure large volume change caused by lithiation/delithiation cycles, thereby maintaining high capacity and cycling stability.

4.2.2 Methodology

All the first-principle calculations were conducted *via* the Vienna *Ab-initio* Simulation Package (VASP)[103–106] with the projector augmented wave (PAW) potentials.[107] For the exchange-correlation functional, we used the generalized gradient approximation (GGA) of Perdew-Becke-Ernzerhof (PBE)[108] with spin polarization considered. We used two different sets of parameters: one for lower energy configuration sampling and the other for accurate total energy determination of these lower energy configurations determined. For the coarse energy sampling calculations, a plane-wave basis set with a cutoff energy of 300 eV and Γ-centered *k*-meshes with the density of 2000 *k*-points per reciprocal atom were used. The accurate total energy calculations were performed with a plane-wave basis set cutoff energy of 520 eV and Γ-centered *k*-meshes

with the density of 8000 k-points per reciprocal atom. DFT + U method[109] was used to treat the $3d$ electrons of Co and Cu ions with U values of 3.3 eV and 4.0 eV adopted following previous studies.[112] To simulate the sodiation process of the MoS_2, we used the Non-Equilibrium Phase Searching method as described in Section 3.2.3.

4.2.3 Results and discussion

We investigate the non-equilibrium lithiation process of Cu-substituted Co_3O_4 by the prediction of non-equilibrium structures along the lithiation pathway based on geometrical numerations. Four non-equilibrium phases ($Li_xCu_{0.5}Co_{2.5}O_4$, x = 1.0, 2.5, 5.0, 8.0) are identified constituting the Li-$Cu_{0.5}Co_{2.5}O_4$ convex hull (**Figure** 4.1a) during the lithiation process of Cu-substituted Co_3O_4. Using a series of lithiation reactions with these non-equilibrium phases considered, we offer the calculated non-equilibrium lithiation voltage profiles (**Figure** 4.1b) which fit well to the experimental curves. To confirm the sequential order of reduction, Bader charge analysis were conducted for Co and Cu ions in metastable phases (**Figure** 4.3).[138,139]
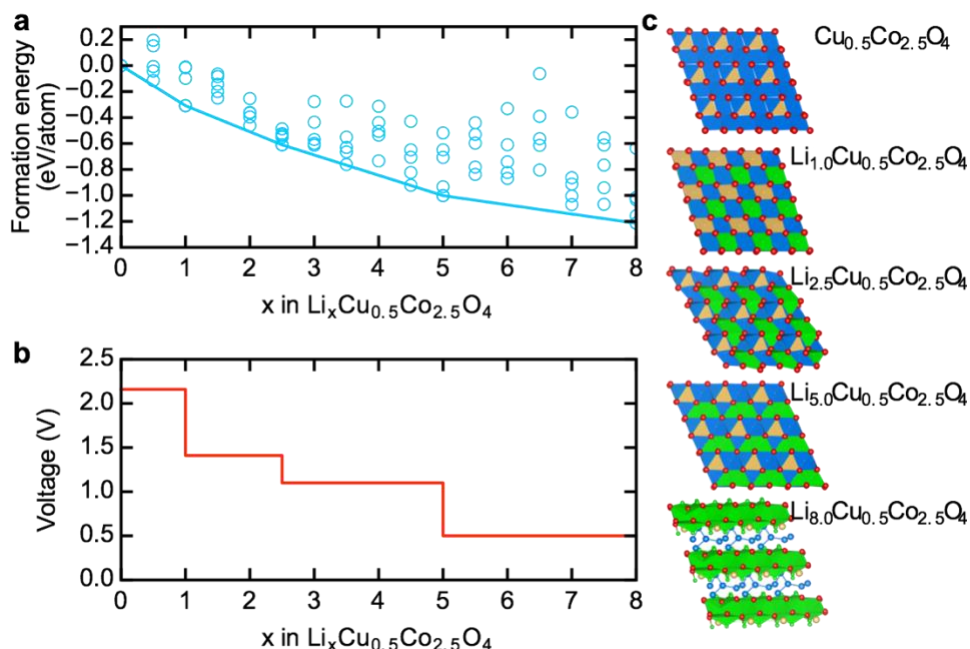
Figure 4.1. Search for the non-equilibrium intermediate phases through the Li- Cu-substituted Co_3O_4 (taking Cu:Co ratio as 1:5) reactions. (a) Convex hull built with all the calculated non-equilibrium phases and (b) corresponding voltage profiles of the Li insertion into Cu-substituted Co_3O_4. (c) Structures of the four non-equilibrium phases predicted along the lithiation of Cu-substituted Co_3O_4.

The lithiation of Cu-substituted Co_3O_4 initiates by Li taking the octahedral sites ($x = 1.0$) neighbored by Cu ions as shown in **Figure** 4.1c and Co^{3+} ions partially get reduced to Co^{2+} when Bader charge of Cu decreases from to +1.27e to +1.23e. With further lithiation ($x = 2.5$ and 5.0), the amount of Li inserted exceeds what the octahedral can accommodate and the Li ions energetically prefer the tetrahedral sites. Cu and Co ions experience reduction $Co^{3+} \rightarrow Co^{2+} \rightarrow Co^0$, $Cu^{2+} \rightarrow Cu^{1+}$ with Cu ions get partially reduced to their metal states. Meanwhile, the oxygen *fcc* framework only gets distorted slightly and the lithiation shows features of intercalation-type with overall preserved oxygen backbones.

Beyond the intercalation-type reaction range ($x \geq 5.0$), both Cu and Co ions get partially

reduced to their metal states (**Figure** 4.1c) and extruded. The lithiation now switches to the

conversion-type reaction with features of phase separation. When the Cu-substituted Co_3O_4

is fully lithiated ($x = 8$), Cu and Co ions have been fully reduced to Cu/Co metal and Li

ions combine with O ions forming Li_2O.
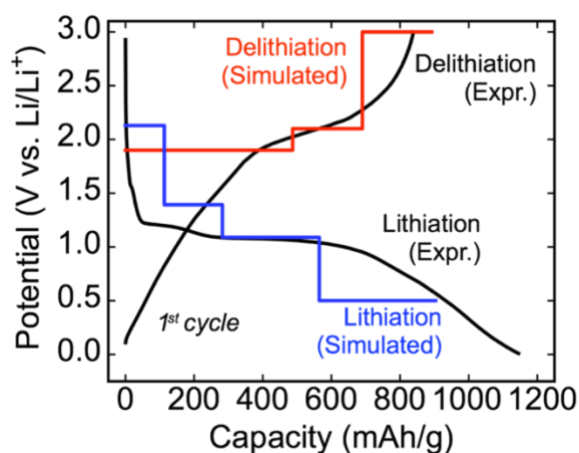
Figure 4.2. Comparison of experimental and DFT simulated voltage profiles for the first cycle of

lithiation and delithiation.
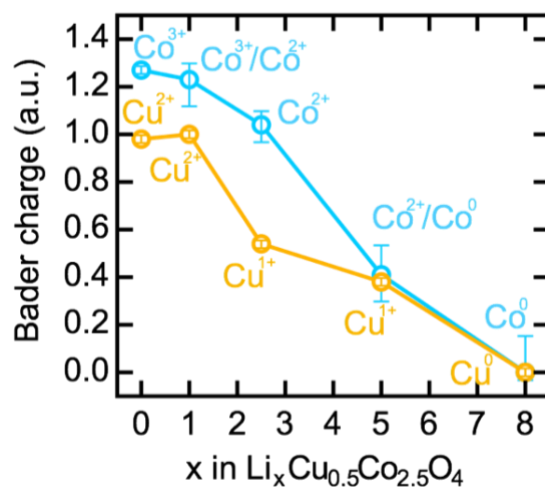
Figure 4.3. Averaged net charges on Cu and Co in $Li_xCu_{0.5}Co_{2.5}O_4$ ($0 < x < 8$).

4.2.4 Conclusion

In conclusion, the substitution of a third metallic element (Cu) into binary oxides (Co_3O_4) alters the fundamental processes of lithiation/delithiation. Together with experimental proofs[39] we show that metal Cu intrinsically formed in the first lithiation cycle remains partially stable as a metallic support on which Li_2O+Co/CoO redox products are anchored. The Cu-based network also provides a highly conductive pathway for electrons and enables Li-ion transport. This "adaptive architecture" accommodates the formation of Li_2O in the discharge cycle, and underpins the catalytic activity of Li_2O decomposition in the charging cycle.

4.3 CuS

4.3.1 Introduction

Recent development of two-dimensional (2D) transition metal chalcogenides provides new choices for battery electrodes since they have intercalation channels to enhance the reaction cyclability and proceed *via* a conversion reaction to maintain their high capacities. As a member of this family, copper sulfide (CuS) exhibits a similar 2D layered structure as many others, in which the layers composed of Cu-S tetrahedrons are separated by van der Waals S-S bonds, providing open channels to facilitate fast lithium intercalation. This phenomenon has been observed in similar metal sulfides such as TiS_2, MoS_2, and SnS_2.[149–154]

Previous studies have revealed that the full lithiation of CuS follows the equation similar to a conversion reaction, to allow for 2 Li^+ ions being stored for each CuS formula unit:[155–163]

$$CuS + 2\ Li^+ + 2\ e^- \rightarrow Cu + Li_2S \qquad (4.1)$$

Under conditions of thermodynamic equilibrium, this reaction would proceed through a two-step process to produce Cu_2S and Cu sequentially as revealed by X-ray diffraction: [155–158]

$$CuS + Li^+ + e^- \rightarrow 0.5\ Cu_2S + 0.5\ Li_2S \qquad (4.2)$$

$$0.5\ Cu_2S + Li^+ + e^- \rightarrow Cu + 0.5\ Li_2S \qquad (4.3)$$
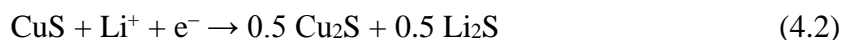
where Cu is reduced from 2+ to 1+ in the Eq. 4.2, when lithium ions break the interlayer van der Waals S-S bonds but keep the overall anion framework intact; and further lead to the extrusion of Cu metal and microscopic phase separation (so-called displacement reaction)[156,157] in Eq. 4.3. However, in practical cases where non-equilibrium conditions such as local concentration and diffusion rate of lithium and electrochemical overpotential are generally applied, there have been a diversity of proposed reaction paths, such as disproportionation reaction and conversion reaction (nanoscopic phase separation associated with dispersive metal nano-precipitation and complete destruction of host structures).[155,156,159–163] Although recent development showed improved cycling performance of CuS by nanostructuring, where kinetic effects tend to be more pronounced due to the dramatic size reduction and usually play a key role in the determination of the reaction paths, it is still unclear whether the lithiation of copper sulfide dictates a displacement or conversion mechanism, the answer to which may provide implications for a general group of metal sulfide materials as LIB electrodes. It is also noted that precise identification of intermediate phases during phase transformation of CuS appears to be difficult due to the existence of many non-stoichiometric copper sulfides, such as djurleite $(Cu_{1.96}S)$, digenite $(Cu_{1.8}S)$, anilite $(Cu_{1.75}S)$ in addition to the most stable covellite (CuS)

and chalcocite (Cu_2S) phases, especially when the samples were examined by post-mortem X-ray or electron microscopy techniques at conditions far away from the operando state.[155,156] First-principles calculations would offer an intriguing chance to accurately reveal the detailed underlying mechanisms at the atomistic scale, which is often difficult to obtain solely *via* conventional experiments.

Here, we use DFT to track the structural and chemical evolution and phase transformations during lithiation in CuS. The proposed reaction mechanism can interpret the overall electrochemical discharge profile that represents the collective behavior of the entire nanocrystals. These findings uncover the reaction pathways of the Li/CuS system and shed light on the mechanistic understanding of phase transformations in general metal sulfides materials with fast lithiation channels induced by van der Waals interlayers.

4.3.2 Methodology

First-principles density functional theory (DFT) calculations were performed *via* the Vienna Ab-initio Simulation Package (VASP) [103–106] with the projector augmented wave (PAW) potentials. [107] For the exchange-correlation functional, generalized gradient approximation (GGA) of Perdew-Becke-Ernzerhof (PBE) [108] was used with spin polarization and the vdW-D2 functional was adopted including a self-consistent van der Waals (vdW) correction.[164] Two different sets of parameters were used with one for lower energy configuration sampling, and the other for accurate total energy determination. For coarse sampling calculations, we used kinetic energy cutoffs of 300 eV for the plane wave basis set, and Γ-centered grids of approximately 4000 k-points per reciprocal atom. The accurate calculations were conducted with a plane-wave basis set cutoff energy of 520

eV, and Γ-centered k-meshes with the density of 8000 k-points per reciprocal atom were used in related calculations. To search for the non-equilibrium phases through the Li-CuS reaction, the Non-Equilibrium Phase Search method was applied as described in Section 3.2.3.

4.3.3 Results and discussion

We investigated the lithiation process of CuS using DFT calculations by exploring both equilibrium and non-equilibrium reaction pathways using approaches as described in Methods. To simulate the equilibrium path, the ternary Li-Cu-S phase diagram (0 K) was constructed by calculating formation energies of all known compounds of the Li-Cu-S chemical space with structures adopted from the Inorganic Crystal Structure Database (ICSD).[120] The ground state Li-CuS reaction was found to go through two three-phase regions (Figure 4.4). A two-step lithiation route is therefore suggested (CuS + Li → Cu_2S + Li_2S → Cu + Li_2S) as observed in bulk CuS systems. The corresponding equilibrium lithiation voltage profile was calculated which shows a similar trend with the experimental discharge voltage curve of the bulk CuS materials (Figure 4.5). It is noteworthy that the discharge curve measured from the nanoflakes exhibits large differences from the one measured in bulk materials and voltage profile predicted by the equilibrium lithiation (Figure 4.5), suggesting an alternative reaction path for the lithiation processes of the CuS nanoflakes. As a result, we focused on the non-equilibrium lithiation pathways involving intermediate structures as the source of the shape and magnitude variations from the equilibrium voltages. We studied the non-equilibrium lithiation process of CuS by the prediction of non-equilibrium structures along the discharge pathway based on geometrical

enumeration and electrostatic energy screening. We were able to identify a series of non-equilibrium phases constituting a metastable Li-CuS convex hull as shown in Figure 4.6. The calculated non-equilibrium voltage profile shows reasonable agreement with the experimental discharge curve for the lithiation of CuS nanoflakes (Figure 4.5). We then looked into the atomistic structural evolution during the non-equilibrium lithiation. As displayed in the upper panel of Figure 4.7, during the non-equilibrium lithiation, Li ions would first intercalate into the interlayer channels held by van der Waals bonds, and then fill up the open tetrahedral sites on both sides of the interlayer spacing, forming $Li_{1.0}CuS$ with Cu^{2+} partially reduced to Cu^{1+} (Figure 4.). Afterward, further Li insertion (up to 6 per unit cell) would take the remaining empty tetrahedral sites and gradually extrude the fully reduced Cu^{0} atoms, resulting in a nominal composition of $Li_{2.0}CuS$, followed by the phase separation into Cu and Li_2S. The final phase is characterized by alternative Cu and Li layers. The evolution of atomic structure confirms the lithiation through the displacement mechanism and matches with HRTEM observations at the pristine and final states.[42]
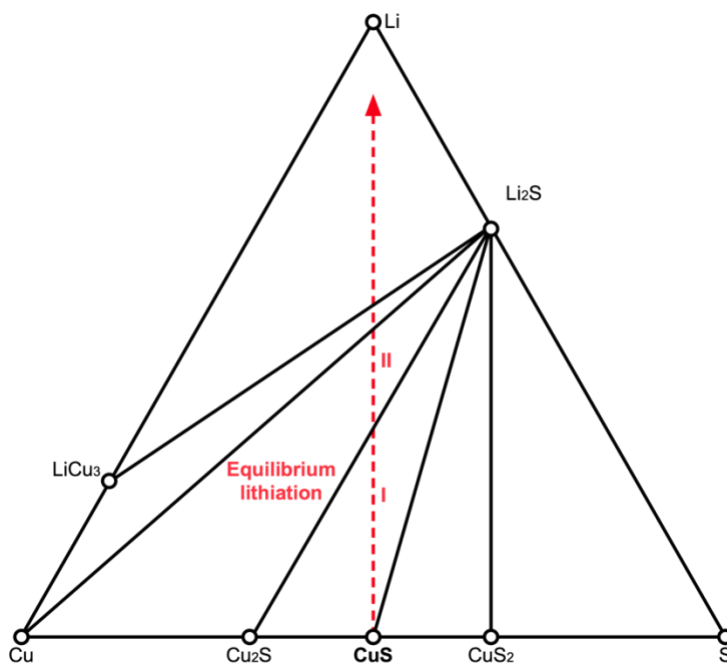
Figure 4.4 Calculated Li-Cu-S ternary phase diagram (0 K) and the equilibrium lithiation reaction path of Li-CuS. The equilibrium reaction path is presented by the red dotted line through two three-phase regions (I, II).
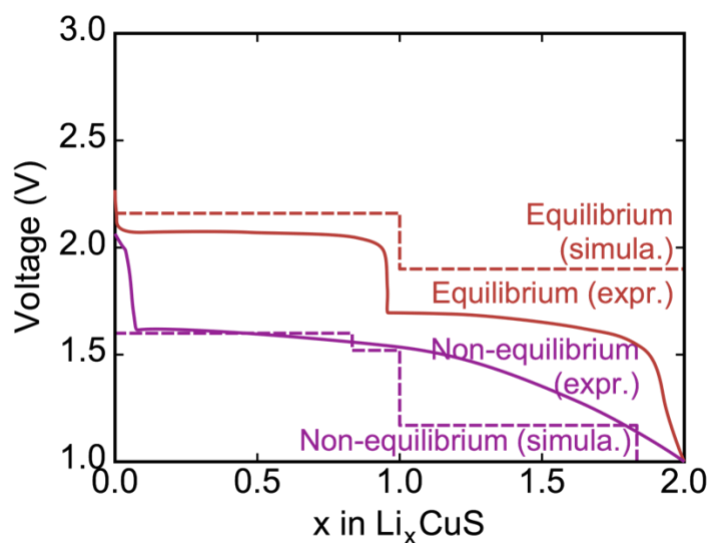
Figure 4.5 Calculated equilibrium and non-equilibrium lithiation voltage profiles compared to the experimentally observed counterparts. Equilibrium calculated/experimental curves are shown as

red solid/dotted lines. Non-equilibrium calculated/experimental curves are shown as blue solid/dotted lines.
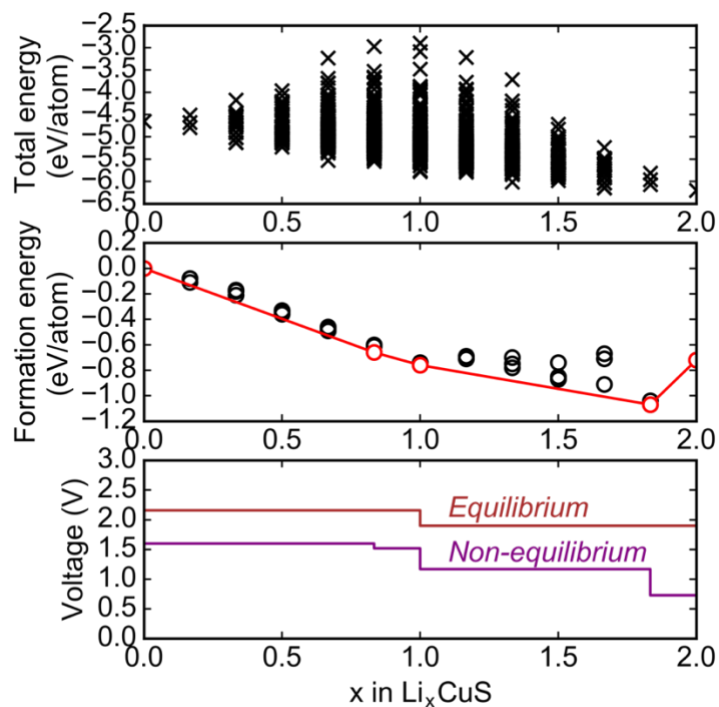
Figure 4.6. (a) Sampled total energies of all the configurations. (b) Non-equilibrium Li-CuS convex hull with four intermediate phases determined. (c) Predicted non-equilibrium reaction voltage profile with the equilibrium voltage profile as the reference.
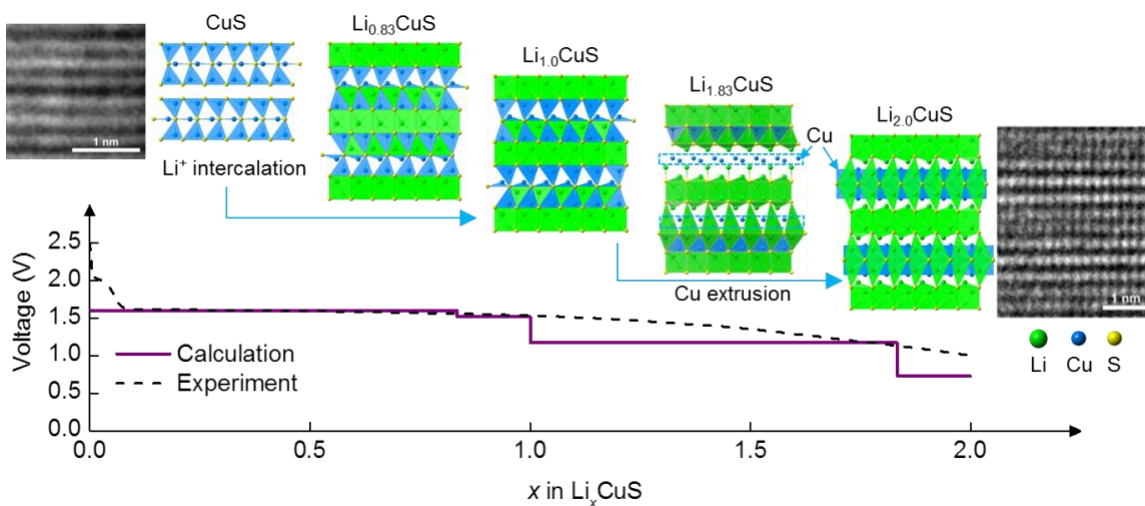
Figure 4.7 DFT calculated discharge voltage profile and atomic models corresponding to the predicted intermediate phases during the non-equilibrium lithiation process in CuS nanocrystals. The black dashed line indicates experimental discharge curve. Two HRTEM images show good structural agreement for both pristine CuS (left) and final Li_2CuS (right).
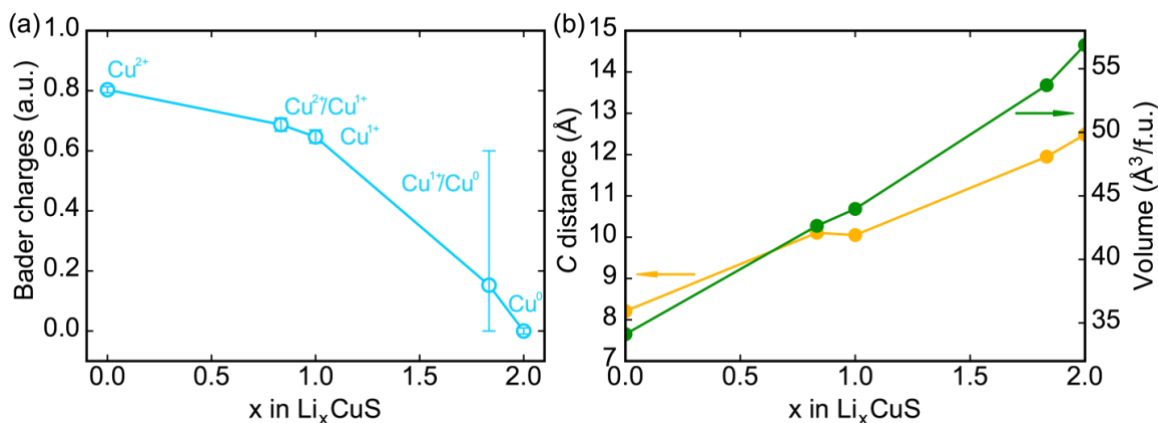
Figure 4.8 (a) Averaged net charges on Cu in Li_xCuS ($0 < x < 2$) based on the Bader charge analysis. (b) C-distance and volume evolution during the lithiation process of CuS. The error bar corresponds to the distribution of charges on specific Cu ions.

4.3.4 Conclusion

In summary, we have investigated the phase transformations in the CuS/Li electrochemical system. With DFT calculation, the atomistic mechanism of non-equilibrium lithiation in CuS has been uncovered, which is suggested to be responsible for the flattened voltage profile in the first discharge under realistic kinetic circumstances. Our findings obtained from CuS nanoflakes shed light on the mechanistic understanding of nanoscale lithiation in other 2D transition metal chalcogenide systems.

4.4 MoS$_2$

4.4.1 Introduction

To meet the demand of inexpensive and environmentally friendly energy storage technologies, sodium-ion battery is promising especially for large-scale energy storage integrated with renewable energy sources such as solar and wind. Due to the scarcity of lithium, there are clear and compelling economic and practical drivers to explore alternative to lithium ions in charge storage devices. Transition-metal dichalcogenide materials such as molybdenum disulfide (MoS$_2$) have layered structure in which each layer has a slab of transition metal atoms sandwiched by two slabs of chalcogenide atoms. They are potentially promising electrodes materials for alkali-ions rechargeable battery, such as Li$^+$,[165,166] Na$^+$,[167] Mg^{2+},[168] and even K$^+$.[169] Covalent bonds are formed between Mo and S within each layer and the Mo-S polyhedron can be described as a trigonal prism where Mo^{4+} is in the center of the prism. In the structure, there is enough space between the MoS$_2$ layers interconnected with weak van der Waals force to host alkali metal ions during charge. MoS$_2$ allows alkali ions to intercalate therein without a significant volume expansion, which enables MoS$_2$ to be a promising electrode material for high capacity rechargeable batteries. However, the number of the alkali cations can be hosted in the S-Mo-S layer is limited while the structural framework remains stable. It has been shown that up to 1.5 cations can be stored per formula unit of MoS$_2$ before the layered structure collapses.[41] Meanwhile, structure transition between trigonal 2H- and octahedral 1T-AMoS$_2$ (A = Li, Na, K, *et. al.*) accompanied by an electronic state change from semiconducting to metallic have been observed upon alkali-metal ion's

intercalation.[41,167] The phase transformation from 2H to 1T can be achieved by a transversal gliding of one S plane[170]. In sodium intercalation, several Na-intercalated phases, such as 2H-MoS$_2$ (a=0.316 nm and c=1.229 nm), 2H-Na$_{0.5}$MoS$_2$ (P1; a=0.321 nm and c=1.506 nm), 1T-Na$_{0.5}$MoS$_2$ (P2; a= 0.306 nm and c=1.397 nm), 1T-NaMoS$_2$ (P3; a=0.311 nm and c=1.429 nm) and Na$_x$S (P4; a=0.343 nm and c=1.397 nm), have been identified by *ex-situ* X-ray and electron microscopy.

There could be both thermodynamically stable and metastable processes involved in the phase transformations of the electrode materials in the charge and discharge cycles. Here, we applied DFT to study the dynamically structural evolutions of sodium-intercalated MoS$_2$ crystals during sodiation.

4.4.2 Methodology

The first principle density functional theory (DFT) calculations were conducted through the Vienna Ab-initio Simulation Package (VASP).[103–106] With the projector augmented wave (PAW) potentials,[107] generalized gradient approximation (GGA) of Perdew-Becke-Ernzerhof (PBE)[108] was used for exchange-correlation function under considering spin polarization. The vdW-D2 functional was adopted to treat exchange and correlation including a self-consistent van der Waals (vdW) correction.[164] We use two different sets of parameters, one for lower energy configuration sampling, and another for accurate total energy determination of the low energy structures that are determined from the sampling. For coarse sampling calculations, we use kinetic energy cutoffs of 300 eV for the plane wave basis set, and Γ-centered grids of approximately 4000 **k**-points per reciprocal atom. The accurate calculations are performed with a plane-wave basis set cutoff

energy of 520 eV, and Γ-centered **k**-meshes with the density of 8000 **k**-points per reciprocal

atom were used in related calculations. To simulate the sodiation process of the MoS_2, we

used the Non-Equilibrium Phase Searching method as described in Section 3.2.3.
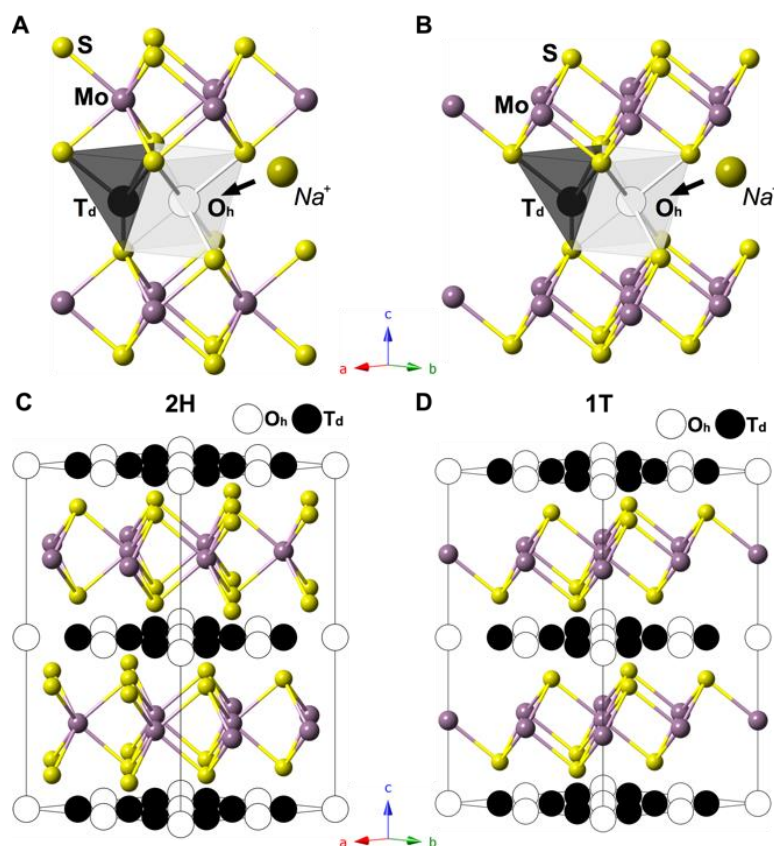
Figure 4.9 Intercalation geometries in 2H/1T MoS_2 structures for Na ions. Tetrahedral (black) and

octahedral (grey) empty sites in (A) 2H and (B) 1T structures of MoS_2. The 2H and 1T structures

with all equivalent tetrahedral and octahedral sites marked are shown in figure (C) and (D).

4.4.3 Results and discussion

MoS_2 is a $4d$ transition metal dichalcogenide which exists in three different

polytypes of 2H, 3R and 1T with different structures while the 2H and 1T polymorphs

involved in the electrochemical sodiation. In 2H-MoS_2, each Mo occupies a trigonal

prismatic coordination sphere that is bound to six sulfide ligands. The trigonal prisms are

interconnected to give a layered structure. The 2H structure has two intercalation sites: the octahedral (O_h) site above the hexagon center where six Na-S bonds can form; and the tetrahedral (T_d) site above a Mo atom where four Na-S bonds can form (Fig. 4.9). Contrarily, the Mo atoms locate in octahedral coordination spheres in 1T-MoS$_2$, which are also bound to six sulfide ligands. A different layered structure is built by octahedron interconnection. The 1T structure also has two intercalation sites: the octahedral (O_h) site above a S atom where six Na-S bonds can form; and the tetrahedral (T_d) site above a Mo atom where four Na-S bonds can form (Fig. 4.9).
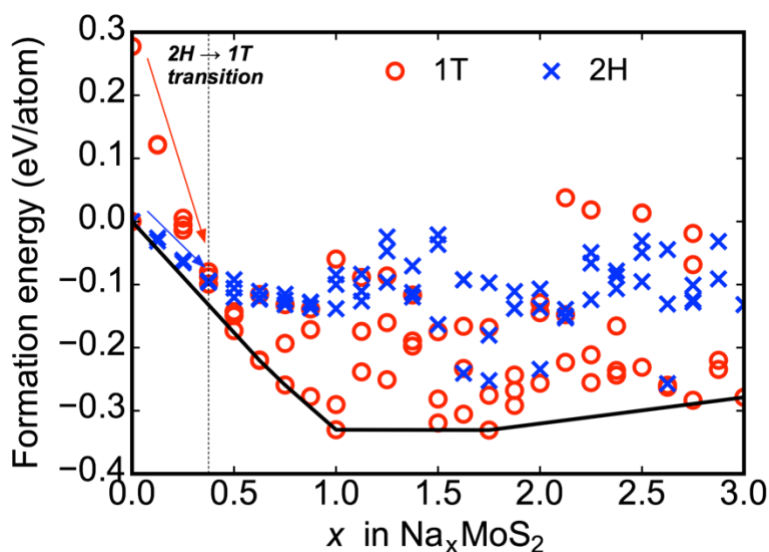
Figure 4.10 Convex hull generated with all calculated intermediate phases. A cross point between the trends of 1T and 2H around $x = 0.375$ can be determined indicating the energetic preference of the 1T configuration over the 2H counterpart after 0.375 Na per MoS$_2$ inserted.

During the sodiation process of MoS$_2$, we were able to identify five intermediate phases (Na$_x$MoS$_2$, $x = 0.625, 0.75, 1.0, 1.75$, and 3) that are shown in Fig. 4.12. The convex

hull built on these stable phases is shown in Fig. 4.10, along with the corresponding voltage profile in Fig. 4.12. Start from the original 2H structure (Fig. 4.12A, $x = 0$), the sodiation initiates by taking the unoccupied O_h sites and proceeds through a phase transition from 2H to 1T structure (Fig. 4.12B, $x = 0.625$) by S shifting.
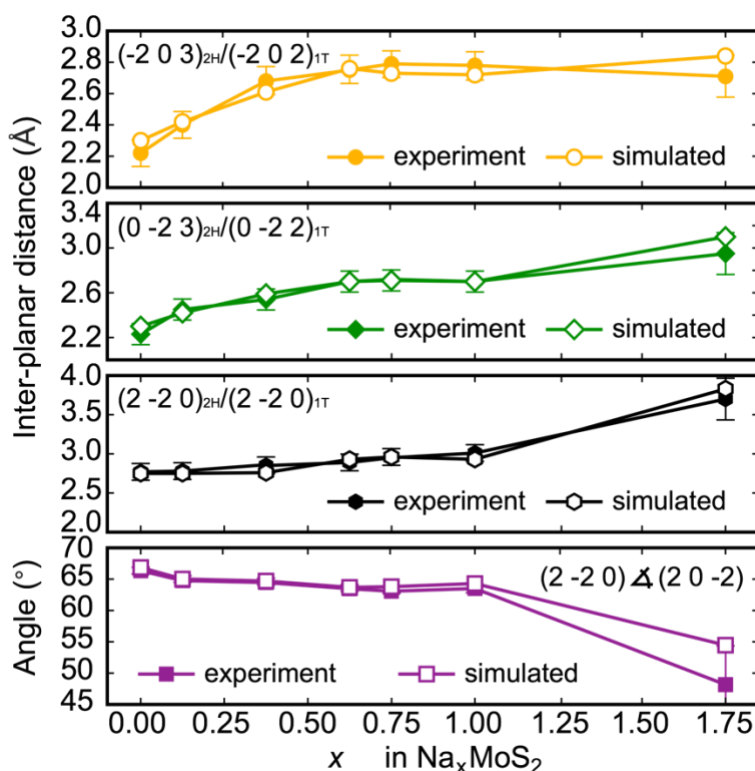
Figure 4.11 Comparison of calculated and experimental spacing of the lattice plane (-2 0 3)_2H, (-2 0 2)_1T, (0 -2 3)_2H, (0 -2 2)_1T, (2 -2 0)_2H and (2 -2 0)_1T, and angles between the (2 -2 0) and (2 0 -2) for all the intermediate phases during the sodiation of the MoS_2 nano particle.

Further sodiation occurs *via* two intermediate phases (Fig. 4.12C, $x = 0.75$), (Fig. 4.12D, $x = 1.0$) through Na ion ordering with intact Mo and S backbones. The $NaMoS_2$ phase reproduces the structure of the known $LiMoS_2$ with all the O_h sites now being

filled.[171,172] Na ions have to take the T_d sites in subsequent sodiation. The Mo-S layers start to collapse when more than 1.5 Na ions inserted (Fig. 4.12E, $x = 1.75$) with the congregating between S and Na atoms. Na ion intercalation stops after that and the sodiation reaction switches to the conversion style with the final phase (Fig. 4.12F, $x = 3.0$) featured with separated Na_2S and isolated Mo atoms. To get a better energetic understanding of the 2H → 1T phase transition occurring around the range ($0 < x < 0.625$), the convex hull between the first two phases was examined in detail. A cross point between the trends of 1T and 2H around $x = 0.375$ can be determined indicating the energetic preference of the 1T configuration over the 2H counterpart after 0.375 Na per MoS_2 inserted. Na ions occupy O_h sites randomly during the onset of the sodiation ($x = 0.125$, 2H, $x = 0. 25$, 2H). The unbalanced sodiation between Mo-S layers enables the S shifting and triggers the 2H → 1T phase transition around $x = 0.375$. The following intermediate metastable phases ($x = 0.375$, 1T, $x = 0.5$, 1T) show ordered Na occupation. Using a series of sodiation reactions considering the intermediate phases, we provide a calculated sodiation voltage profile that is in great agreement with the experiment (Fig. 4.12G). The calculated spacing of the lattice plane (-2 0 3)_2H, (-2 0 2)_1T, (0 -2 3)_2H, (0 -2 2)_1T, (2 -2 0)_2H and (2 -2 0)_1T, and angles of two selected lattice planes for all the intermediate phases show consistency with the experimentally observed values (as shown in Fig. 4.11).
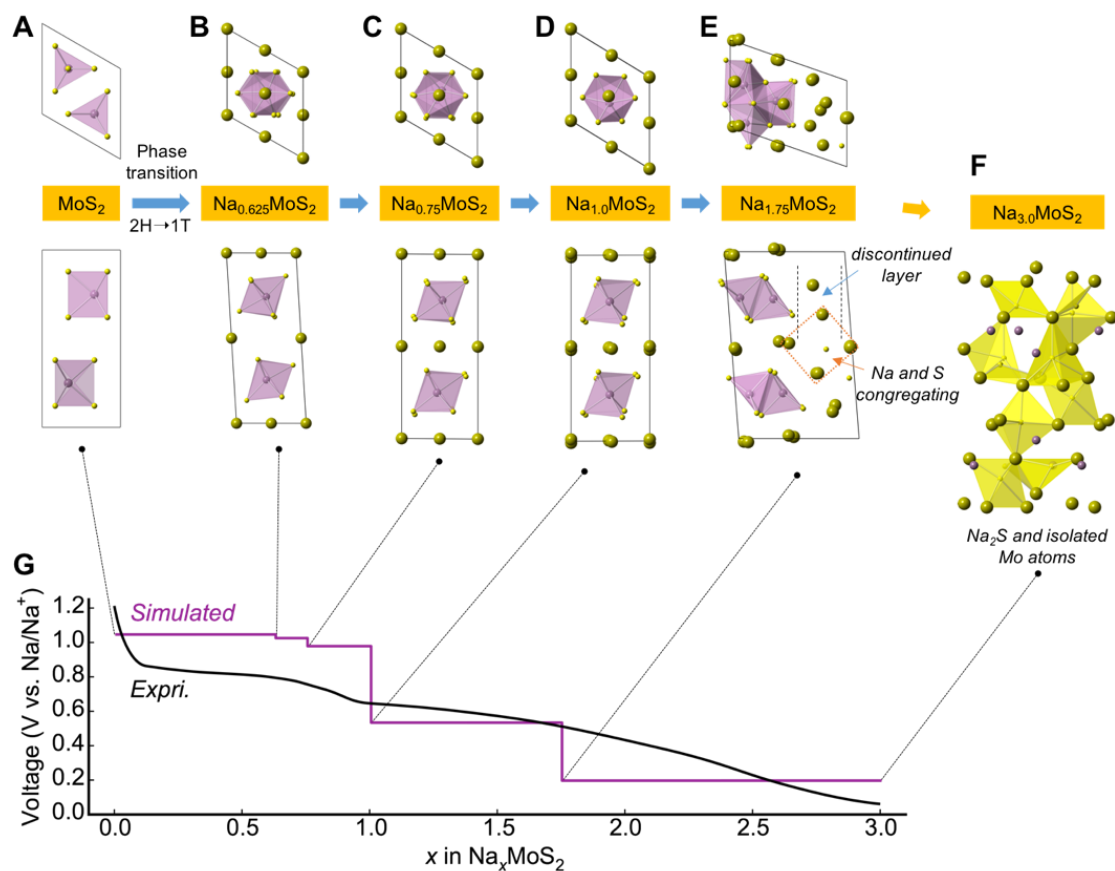
Figure 4.12 Electrochemical sodiation process of MoS_2. Start from the original 2H MoS_2 structure (A, $x = 0$), the sodiation proceeds through a phase transition from 2H to 1T structure (B, $x = 0.625$) by S ion shifting and reordering. Further sodiation occurs *via* two intermediate phases (C, $x = 0.75$), (D, $x = 1.0$) by Na ion ordering with intact Mo and S backbones. The Mo-S layers start to collapse when more than 1.5 Na ions inserted (E, $x = 1.75$). Na ion intercalation stops after that and the sodiation reaction switches to the conversion style with the final phase ($x = 3.0$, F) featured with Na_2S and isolated Mo atoms. (G) Simulated voltage profile of MoS_2 through the intermediate phases, compared to experimental voltage profile.

4.4.4 Conclusion

In summary, several stable/metastable phases have been identified in the early stage of sodiation in nanostructured MoS_2 crystals. The MoS_2 crystal can host up to 1.75 Na per unit formula before the layered structure collapses. Phase transformation from 2H- to 1T MoS_2 is identified to happen when Na content is 0.375, along with Na-ions ordering in the structure. This study provides the insights to understand the sodiation kinetics in a typical layered transition-metal dichalcogenide structure, which is helpful to design advanced type sodium ion batteries in the future.

CHAPTER 5

Exploring the Simultaneous Anionic and Cationic Redox Reactivity in the Li-rich Li_5FeO_4 Based High-Energy-Density Cathode Materials

5.1 Introduction

Conventional cathode materials employed in lithium-ion batteries (LIBs) are generally lithiated transition metal (TM) oxide compounds. These materials store and release electrical energy when Li ions are extracted and inserted with charge compensated by redox reactions of the TM cations, respectively.[2] The specific capacity (mAh/g) of these cathodes, therefore, is limited by the number of electrons per TM cation that can participate in the redox reactions and the relatively high atomic weight of the transition metal oxide host. Recently, the exclusive dependence on the transition metal cations as the redox center in the cathode has been challenged by the discovery of oxygen redox reactivity in cathode materials of Li-excess layered oxide cathode.[10–12,14–16,47] The opportunity has thus arisen to boost the capacity and energy density of lithium-ion batteries if the anionic and cationic redox activity can be enabled at the same potential.[45,173] However, it is challenging to develop anionic-redox-based cathodes with acceptable cycle performance. The key issue is the irreversible O_2 gas release due to the instability of oxygenates (*i.e.* O^- or O_n^{2-}) generated in the solid state. Several studies have demonstrated stabilized oxygenate species in cathode materials using expensive $4d$ or $5d$ TM-metal ions such as Ir and Ru.[10,11,16,45] Nevertheless, cheap $3d$ TM-metal oxides are desirable to achieve highly reversible oxygen redox in practical applications, which requires

understanding of the mechanisms underpinning the anionic redox chemistry in this category of materials.

In principle, Li_2O with the anti-fluorite structure maximally exploits the anionic redox, as it only uses oxygen ions to provide the charge-compensating electrons in the lithiation/delithiation: $Li_2O \leftrightarrow 0.5Li_2O_2 + Li^+ + e^-$.[174] The direct Li_2O/Li_2O_2 conversion requires a catalyst to promote the electrochemical reaction because of the low electrochemical activity and poor electronic conductivity of lithium oxides. The release of O_2 is often associated with this reaction due to the metastability of the delithiated Li_2O.[175] Prior studies show that the potential of the oxygen redox reaction of $Li_2O/Li_2O_2/LiO_2$ is as low as ~3.0 V *vs.* Li^+/Li.[176,177] This value is comparable to the potential of several *3d* TM redox reactions, offering the possibility of simultaneous cationic and anionic redox in TM-substituted anti-fluorite compounds. Indeed, it has been shown that the ionic and electronic conductivity, and thus electrochemical activity, are enhanced upon substituting some of the Li ions with TM in Li-rich, defect anti-fluorite compounds such as Li_5FeO_4, Li_6CoO_4, and Li_6MnO_4.[178–181] The anti-fluorite structure offers high potential capacity due to the rich Li ion content (over 5 per transition metal ion). For instance, Li_5FeO_4 (LFO) delivers a theoretical capacity over 700 mAh/g when charging to 4.7V vs. Li^+/Li, amounting to an electrochemical extraction of about 4 Li^+ ions per Fe^{3+} ion.[180,182,183] Since it is unrealistic to expect that four electrons can be removed from a single Fe^{3+} ion, anionic (O^{2-}) oxidation has been suggested but without quantitative analysis or clear confirmation.[46,182,183] Despite previous studies of the electrochemical properties of LFO, little is known about the nature of the oxygen redox including the electrochemical potential, the reversibility, and the interplay of Fe and O redox.

Herein, we report the realization of simultaneous anionic and cationic redox in anti-fluorite structures, exemplified by Li_5FeO_4, at the same potential. Highly reversible anionic redox reactivity with no obvious oxygen release is enabled in this earth-abundant iron oxide under controlled voltage range. We obtained a clear and quantitative picture of the structural and composition evolution of the LFO by ex-situ and in-situ XRD, Raman, pressure measurement, DEMS and XAENS, and first-principle calculations. Simultaneous oxidation of Fe^{3+} to Fe^{4+} and O^{2-} to O^- is observed at approximately 3.5 V *vs*. Li^+/Li during the extraction of the first two Li ions from LFO. After the initial extraction of two Li ions, the iron and oxygen redox couples are highly reversible within the solid state in subsequent cycles between 1.0 and 3.8 V *vs*. Li^+/Li. A Li-excess Li_6-O configuration, identified by DFT calculations plays a key role in enabling the reversible O^-/O^{2-} redox behavior. Our findings enrich the oxygen redox mechanism and help designing low cost $3d$ transition metal oxide based high energy density cathode materials.

5.2 Methodology

In this dissertation, we will focus on the methodology of the computational study and all the experimental synthesis, characterization, and electrochemical test procedures are exhibited in *ref.* [48]. All first-principles DFT calculations reported in this study were conducted using the Vienna Ab-initio Simulation Package (VASP)[103–106] with the projector augmented wave (PAW) potentials[107] and the Perdew-Becke-Ernzerhof (PBE)[108] exchange-correlation. A plane wave basis with a cutoff energy of 520 eV and Γ-centered k-meshes with a density of 8000 k-points per reciprocal atom were used for all calculations. All calculations were spin-polarized, with Fe atoms initialized in a high-spin

ferromagnetic configuration and relaxed to self-consistency. The DFT + U method introduced by Dudarev *et al.*.[109] was used to treat the localized $3d$ electrons of Fe with a U of 4.0, obtained by fitting it to experimental and calculated formation enthalpies in a previous study.[112]

a **b** **c**

Li$_4$FeO$_{3.5}$ (SQS)

Li$_3$FeO$_{3.5}$ (SQS)

Li$_2$FeO$_3$ (SQS)
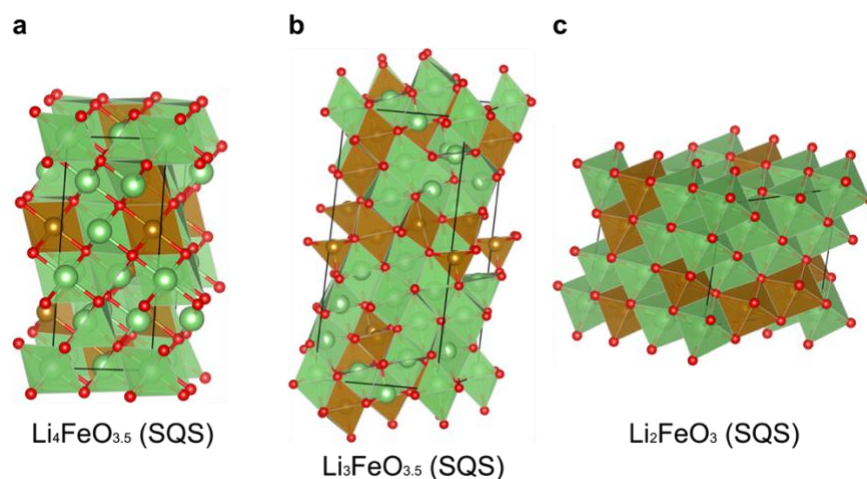
Figure 5.1 The disordered structure of the (a) Li$_4$FeO$_{3.5}$, (b) Li$_3$FeO$_{3.5}$, and (b) Li$_2$FeO$_3$ generated by the SQS method.

Since the delithiated phases of Li$_4$FeO$_{3.5}$, Li$_3$FeO$_{3.5}$ and Li$_2$FeO$_3$ adopt disordered cubic structures, the corresponding computational unit cells were built (Fig. 5.1) using the special quasi-random structure (SQS) method. Started with the cubic rock-salt cell, supercells containing 30 cation sites/30 anion sites, 56 cation sites/56 anion sites and 27 cation sites/27 anion sites were created for Li$_4$FeO$_{3.5}$, Li$_3$FeO$_{3.5}$ and Li$_2$FeO$_3$. We populated the cation sites randomly with Fe and Li in ratios of 4:1, 3:1 and 2:1 for Li$_4$FeO$_{3.5}$, Li$_3$FeO$_{3.5}$ and Li$_2$FeO$_3$. Vacancies were introduced to the anion sites of the Li$_4$FeO$_{3.5}$ and Li$_3$FeO$_{3.5}$ structures randomly in ratios of 3:7 and 1:7 with respect to O while all the anion sites of Li$_2$FeO$_3$ were occupied by O. All SQSs were generated based on a Monte Carlo algorithm

implemented in ATAT[131,132,184] with the constraint that the pair and triplet correlation functions of the SQS are identical to those of the statistically random Li/Fe population of cation sites and O/Vacancy population of anion sites at least up to the third nearest neighbor. According to the XRD observations mentioned in the main text, the $LiFeO_2$ phase shows features of amorphization. A corresponding amorphous computational cell containing 100 atoms was constructed (Fig. 5.2) by applying *ab initio* molecular dynamics to a liquid like state at 2900 K and followed by a rapid temperature quench and energy minimization.[185] The liquid state configurations were equilibrated over two picoseconds under an NVT ensemble. The quench was enabled through a molecular dynamics simulation starting at the equilibration temperature and dropping down to 300 K at the rate of 1 K/fs, followed by conjugate-gradient relaxation of atomic coordinates and cell parameters, stopping when average forces fall below 10^{-2} eV/Å.
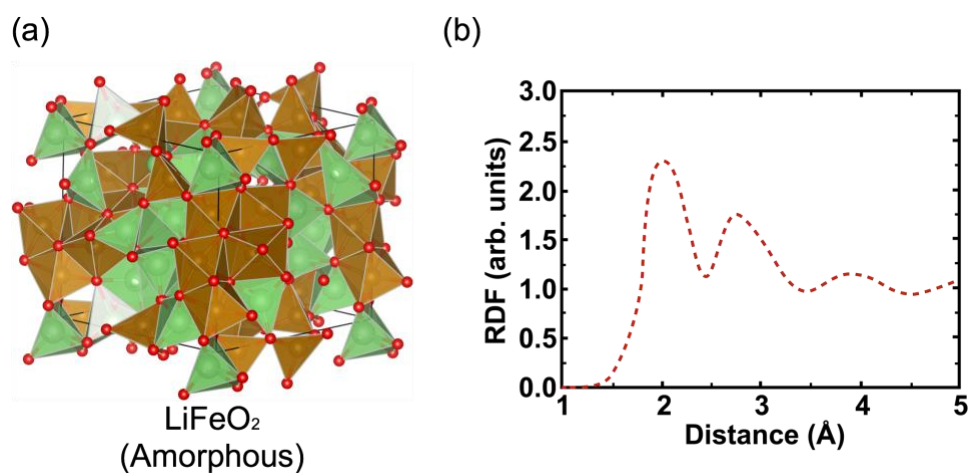
Figure 5.2 Calculated structure of $LiFeO_2$ (a) Generated amorphous structure of $LiFeO_2$. (b) Radial distribution function of amorphous $LiFeO_2$.

5.3 Results and discussion

5.3.1 Phase conversion of LFO during electrochemical cycling

The crystal structure of Li_5FeO_4 can be viewed as substituting 24 Li+ ions with 8 Fe^{3+} ion and 16 cation vacancies in a $2\times2\times2$ Li_2O cell (Fig. 5.3a). The charge-discharge behavior of LFO between 4.7 and 1.0 V is plotted in Fig. 5.3b. The initial charging curve exhibits two plateaus at about 3.5 V and 3.9 V, denoted stage I and stage II respectively. This charging curve is consistent with previous literature,[182,186,187] but the subsequent discharging and cycling curves have been rarely discussed before. In the first discharge to a potential as low as 1.0 V, two tilted plateaus at about 2.2 V and 1.5 V can be observed corresponding to the "insertion" of 1 Li ion at each plateau. The first charge to 4.7 V is electrochemically irreversible under the operating conditions employed here. In the following cycles, neither of the plateaus at 3.5 V and 4.0 V is recovered; instead, the charging and discharging curves show a plateau at about 2.5 V, and the capacity fades rapidly in the first 5 cycles.
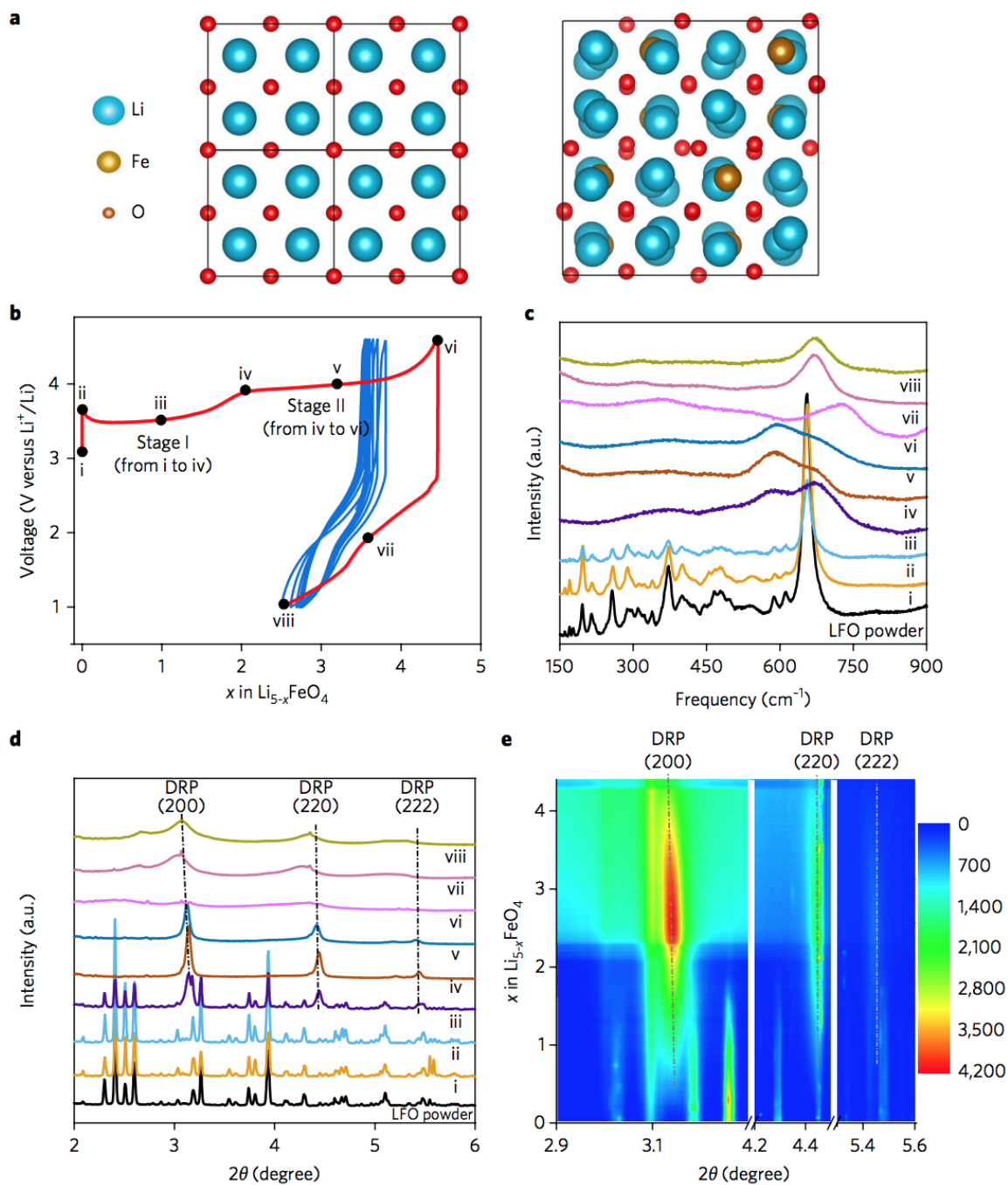
Figure 5.3 Phase conversion of LFO during electrochemical cycling. a, Structure of a $2\times2\times2$ Li_2O supercell and a Li_5FeO_4 unit cell both in the [100] view. b, The charge–discharge behavior of LFO in the first six cycles between 4.7 V and 1 V (first cycle as a red line and the following five cycles in blue). c, d, The *ex-situ* Raman spectra obtained with a 633 nm laser (c) and *ex-situ* high-energy

XRD patterns (d) collected at different states of charge and discharge corresponding to the points in a (labelled as points i–viii). The pristine LFO powder and the cathode collected at points i and ii show typical features of the anti-fluorite Li_5FeO_4, with the prominent band at about 660 cm^{-1} and multiple bands at lower frequency according to *ref.* [188]. e, 2D contour of *in-situ* XRD patterns collected in the first charge, illustrating the continuous evolution of XRD patterns from i to viii in d. The vertical dashed lines in d and e label the diffraction peaks indexed to the (200), (220) and (222) planes of the disordered rocksalt phase (DRP).

LFO electrodes at different states of charge in the first cycle (as labelled from *i* to *viii* in Fig. 5.3b) were harvested for *ex-situ* Raman and X-ray diffraction (XRD) analyses to determine the crystal phase conversion correlated with the plateaus, as shown in Figs. 5.3c and 5.3d, respectively. Both the *ex-situ* Raman and XRD profiles show that the initial LFO with an orthorhombic structure (space group of P*bca*) converted completely to a disordered rocksalt phase at the 3.5 V plateau with the removal of 2 Li ions (from point *i* to *iv* in Fig. 5.3b). [188] The two-phase coexistence can be observed in the middle of the plateau (point *iii* in Fig. 5.3b) as shown by the XRD pattern (Fig. 5.3d). Continuous phase conversion in the first charge is demonstrated in the 2D contour of the *in-situ* XRD patterns (Fig. 5.3e). Gradual fading of the original anti-fluorite phase and growth of the disordered rocksalt phase can be observed when $0 < x < 2$.

Charging of LFO beyond two Li ions on the 4.0 V plateau has been reported previously,[182] but the mechanistic details of the reaction were not elucidated. Here, both the *ex-situ* and *in-situ* XRD patterns show that the disordered rocksalt phase remains as the dominant phase on the 4.0 V plateau. The peaks of the DRP grow stronger at the beginning

of the 4.0 V plateau ($2 < x < 2.5$), then start to get broader and weaker when $x > 2.5$, and eventually become flattened at the end of charging. The XRD patterns of the DRP appear again in the first discharge, but the anti-fluorite phase cannot be recovered, confirming that deep delithiation of LFO is irreversible.
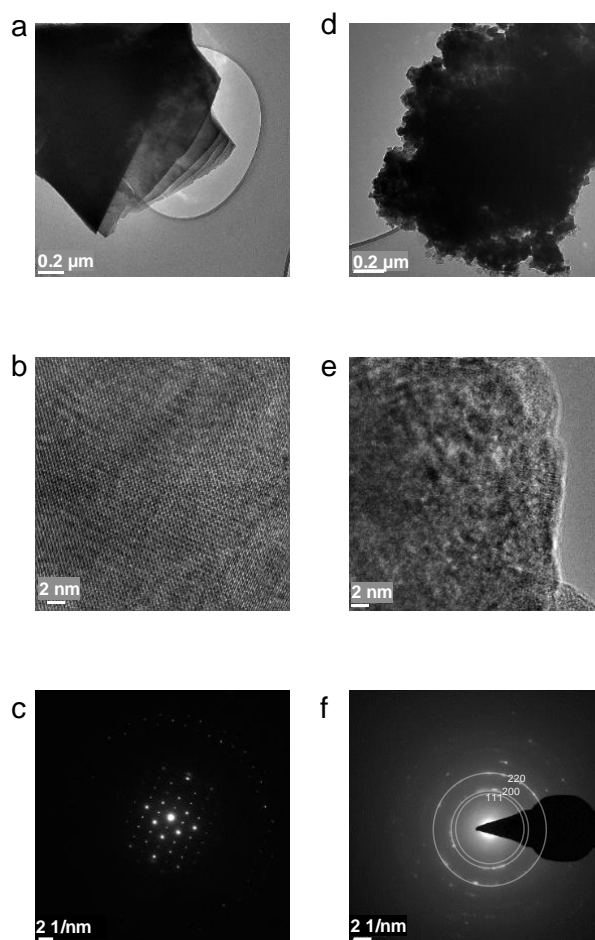
Figure 5.4 Morphology and structure change of Li_5FeO_4 during first charge. Low-resolution TEM image (a, d), high-resolution TEM image (b, e), and SAED pattern (c, f) of pristine Li_5FeO_4 (a, b, and c) and the sample charged to 3.8 V for the removal of 2 Li ions (d, e, and f). It can be observed clearly that the micrometer size LFO particles break into nanoparticles due to the delithiation. The

SAED pattern of the delithiated LFO is indexed by the typical cubic phase structure, with diffuse rings generated by the nanoparticles.

High-resolution images from transmission electron microscopy (TEM) helped explain the evolution of the XRD patterns, as shown in Fig. 5.4. The pristine LFO consists of well-crystallized particles of about 1 μm size, with the selected-area electron diffraction (SAED) pattern showing a typical single-crystal character (Fig. 5.4a-c). In contrast, after the removal of 2 Li ions, the single crystal of LFO breaks into nanoparticles about 10 nm in size with the overall shape maintained (Fig. 5.4d and e). The SAED pattern indicates a polycrystalline property of the particle, and the diffraction rings are well correlated with the XRD patterns.

The fracture of the active particles greatly increases the interface area between the cathode and electrolyte, which should lead to the impedance falling of the LFO cathode in the first plateau. This trend is observed in the in-situ electrochemical impedance spectra in Fig. 5.5. Other possible reasons for this impedance falling include the enhanced charge conductivity due to the initial delithiation and the electronic structure change of iron and oxygen ions. The impedance of cathode reaches the lowest level at the end of the first plateau and then increases gradually with further delithiation at the second plateau. Further understanding of the electrochemistry in the delithiation is required to understand this V-shape evolution of impedance, which will be discussed in detail in the section after the next one.
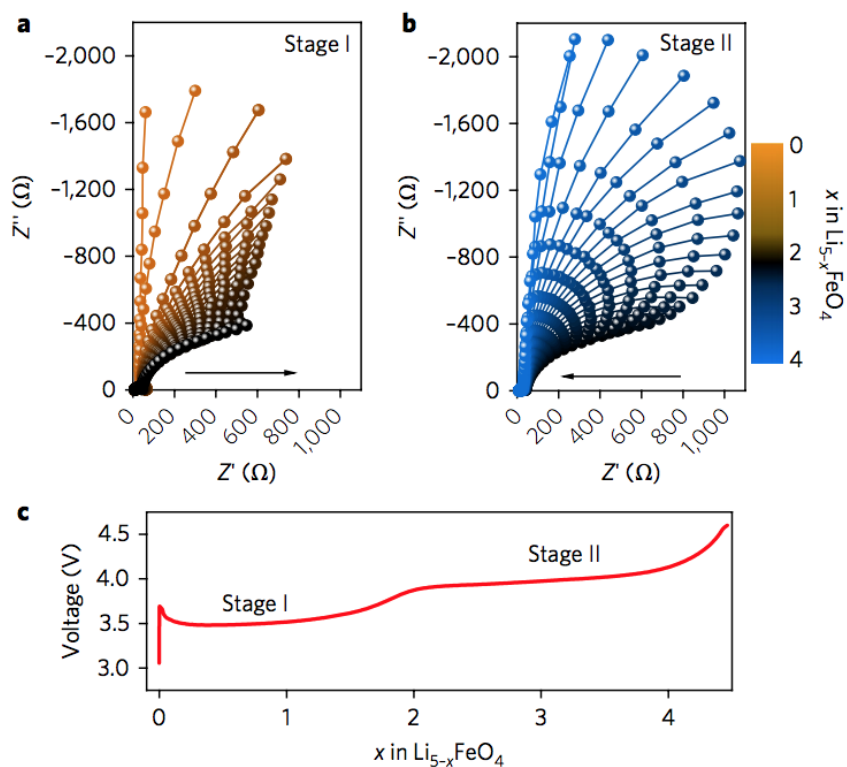
Figure 5.5 In situ electrochemical impedance spectra of Li_5FeO_4 during the first charge. a–c, The EIS plots collected during charging stage I (a) and stage II (b) as denoted in the voltage profile of the first charge of LFO to 4.7 V (c). The color of the lines and spheres represents the number of Li ions removed from the cathode, as demonstrated by the color scale bar on the right. The arrows in a and b show that the impedance of LFO decreases at the 3.5 V plateau but increases at the 4.0 V plateau. The EIS measurements were performed using a three-electrode cell with LFO as the working electrode, a Li wire as the reference electrode and a Li metal foil as the counter electrode. In this way, the impedance contribution of the Li metal anode can be eliminated.

5.3.2 Cationic and anionic oxidation during the first charge

Figure 5.6a shows the in-situ Fe K-edge X-ray absorption near edge spectra (XANES) of LFO during the first charge to 4.7 V. In Stage I (charge to 3.5 eV), the edge position of the main peak A_1, which is related to the oxidation state of Fe, shifted to higher

energy (A_1') due to the oxidation of Fe^{3+} to $Fe^{(3+\delta)+}$ ($\delta \approx 0.5$) with extraction of the first two Li^+ ions. This is an indirect indication that some other type of redox reaction is active, for δ should be 2 if the Li removal is fully charge-compensated by the Fe ion. The shoulder peak B and the strong pre-edge peak C are signatures of FeO_4 tetrahedral coordination.[182,187] The pre-edge is partly caused by a quadrupole-allowed Fe 1s to 3d transition, which is also evident in the octahedral coordination, just not as strongly as in the tetrahedral coordination. The decrease of the intensity of peaks B and C, as well as the gradual change of the three main peaks (A_1, A_2, and A_3 to A_1' and A_2'), originated from the conversion of the FeO_4 tetrahedron in the pristine LFO to the FeO_6 octahedron in the DRP.[187] The disappearance of the FeO_4 tetrahedron is also evident in the Raman spectra (Fig. 5.3c). In contrast, during Stages II, the edge position of peak A shifted to lower energy, indicating that Fe was reduced during further removal of Li^+ without coordination change. Again, the reduction of Fe during charge indicates that some other species is being oxidized (*i.e.*, O ions).
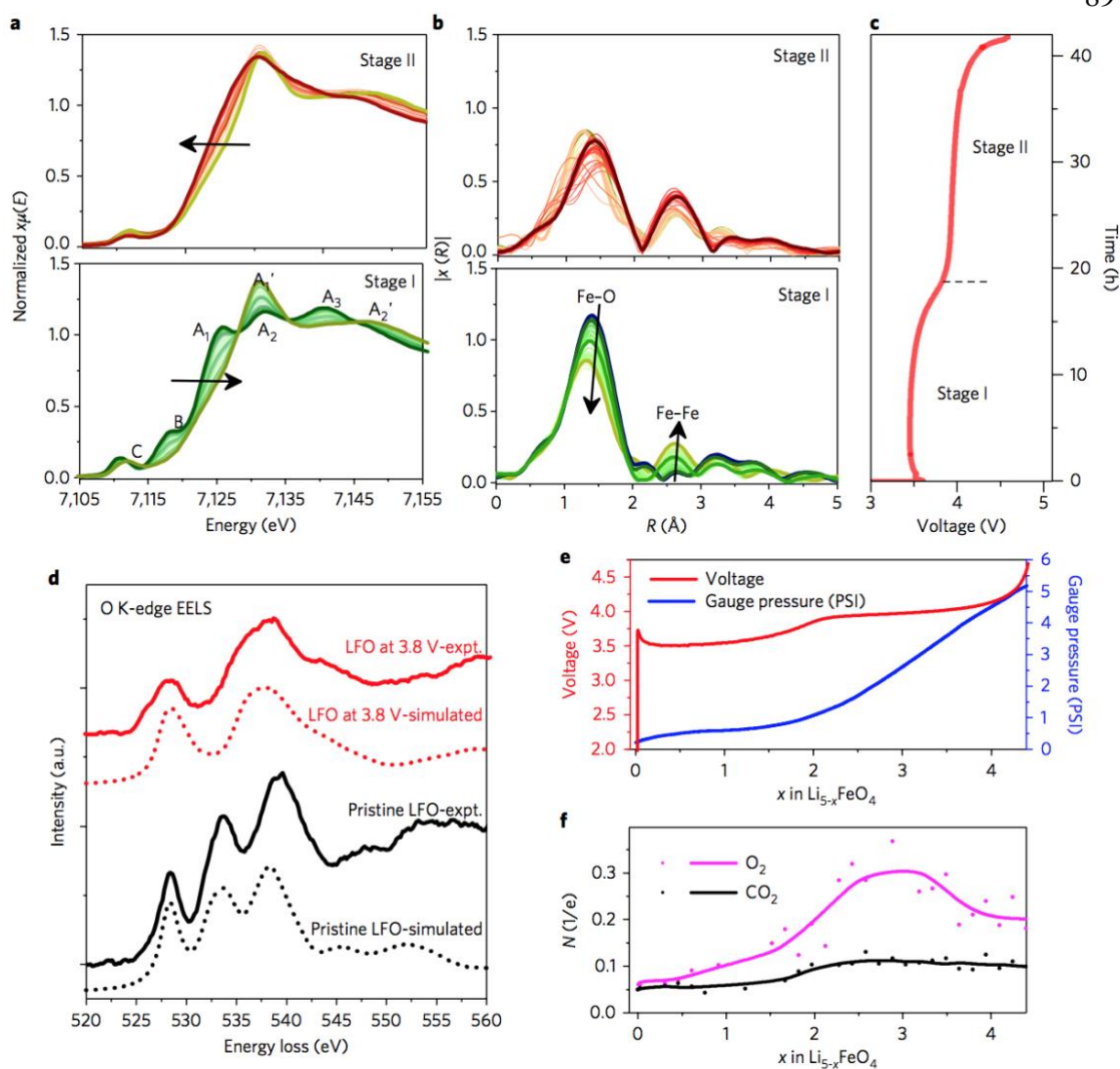
Figure 5.6 Evolution of iron and oxygen in the first charge. *In-situ* Fe K-edge XANES (a) and EXAFS (b) spectra of LFO during the first charge to 4.7 V, corresponding to the stages denoted on the charging curve in c. The decrease of the shoulder peak B and the pre-edge peak C, as well as the gradual change of the three main peaks (A_1, A_2, and A_3 to A_1' and A_2'), originated from the conversion of the FeO_4 tetrahedron in the pristine LFO to the FeO_6 octahedron in the DRP. The arrows in *a* show the shift of the main edge in the two stages, while the arrows in *b* show the decrease of Fe-O peak and the increase of Fe-Fe peak during the charging stage I. FeO, Fe_3O_4, Fe_2O_3 and $SrFeO_3$ were used as standards. d, Experimental collected and simulated *ex-situ* O K-

edge EELS of $Li_{5-x}FeO_4$ when $x = 0$ and 2 in the first charge. The simulations were performed using the crystal structure obtained using the experimental results, which involves both the structural evolution and O redox. e, *In-situ* pressure measurement (upper panel, gauge pressure value of the battery in blue line and the corresponding changing voltage profile in red line), and quantitative DEMS data (lower panel) of O_2 and CO_2 released in the LFO/Li cell in the first charge to 4.7 V. N(1/e) means the number of gas molecules generated by each electron. The lines show the smoothed curves.

The Fe K-edge extended X-ray absorption fine structure (EXAFS) was measured to investigate bond distances and the local structure surrounding the Fe atoms. Figure 5.6b shows the Fourier transform (FT) of the k^2-weighted EXAFS. The peak at ~1.5 Å corresponds to the Fe-O bond. The Fe-O bond in pristine LFO is longer than that in the FeO_6 unit in Fe_2O_3, which demonstrates tetrahedral coordination of Fe in LFO. The Fe-O bond is gradually shortened at the end of Stage I, *i.e.*, approaching the Fe-O bond length of the FeO_6 units in Fe_2O_3. The Fe-O bond distance did not change in an obvious manner during Stage II.

When comparing the number of Li ions extracted versus the valence change of Fe during the two plateaus, we inferred that about $(2-\delta)$ electrons per formula unit (or per Fe) are required from O atoms in the 3.5 V plateau, and another $(2+\delta)$ electrons are required in the 4.0 V plateau. Therefore, the average valances of the four oxygen ions are expected to change from -2 to $-(1.5+0.25\delta)$ and then to -1. The evolution of oxygen valence in the solid cathode was traced by ex-situ O K-edge electron energy loss spectroscopy (EELS) of pristine LFO and LFO charged to 3.8 V (Fig. 5.6d). Three peaks near 528.4 eV, 533.6 eV,

and 539.4 eV are observed in the O K-edge spectrum of pristine LFO, whereas the spectrum for LFO after charging across the 3.5 V plateau exhibits only two board peaks at 528.4 eV and 538.2 eV. The drastic change in the EELS spectra shows the response of oxygen electronic structure to Li electrochemical extraction, which may possibly be linked to a change in the oxygen bonding environment or oxygen redox. The experimentally observed O K-edge EELS spectra of pristine and delithiated LFO were confirmed by O core-level spectrum simulation.

Figure 5.6e shows the in-situ pressure measurement and quantitative differential electrochemical mass spectrometry (DEMS) data of the LFO/Li cell in the first charge to 4.7 V. The pressure increase shows that minor gas release is observed during the charge plateau at 3.5 V. Subsequently, a large amount of gas is released during the 4.0 V plateau. The calculation from DEMS data shows that about 0.1 O_2 gas molecules are released per electron on the first plateau. This number increases rapidly to about 0.3 O_2/e^- when the potential rises to 4.0V.

5.3.3 Simultaneous cationic and anionic redox

The composition of the product generated at the 3.5 V plateau was assumed to be $Li_\alpha Fe^{(4-\alpha)+}O_2$ by Okumura $et\ al$.,[187] but the (111)/(200) peak intensity ratio for this composition should be much higher than that in their observed XRD profiles. They attributed the mismatch of $I(111)$ to lattice distortion. This so-called "mismatch" is also observed here and, indeed, can be eliminated by reducing the Fe/O ratio in the disorder rocksalt phase in the XRD Rietveld refinements. The fined occupancies yield a stoichiometry of $Li_3FeO_{3.5}$ for the DRP after the removal of two Li ions.
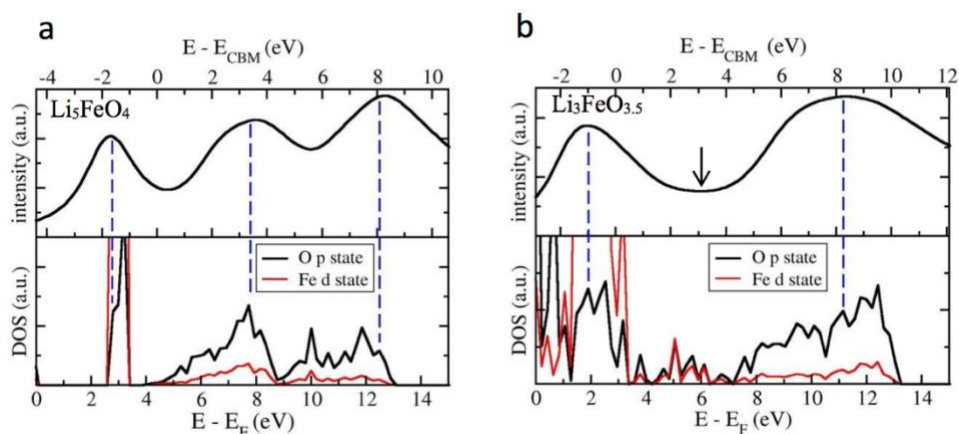
Figure 5.7 Simulated core-level spectrum and ground-state density of states (DOS) for (a) Li_5FeO_4 and (b) $Li_3FeO_{3.5}$. Upper panels show the simulated O K-edge spectra, and lower panels show the GGA-PBE DOS for O p states (black line) and Fe d states (red line). Zero energies in the lower and upper panels correspond to the Fermi level and conduction band minimum (CBM), respectively. The first peaks in the simulated spectra are below zero due to the excitonic effects. Blue dashed lines indicate the coincidence of the peaks.

The O K-edge spectra for both Li_5FeO_4 and $Li_3FeO_{3.5}$ are simulated based on the DFT predicted structures (Fig. 5.1), using the OCEAN code implementing the Bethe-Salpeter equation approach.[189,190] The simulated spectra are in excellent agreement with the EELS spectra (Fig. 5.6d). In order to determine the electronic origin of each peak, we also compared the simulated spectra with the projected ground-state density of states (DOS) of Li_5FeO_4 and $Li_3FeO_{3.5}$, as shown in Fig. 5.7. The three peaks in the Li_5FeO_4 spectrum are attributed to electronic transitions from the O $1s$ core level to the unoccupied Fe $3d$ states (of Fe^{3+} in tetrahedral sites) mixed with O $2p$, and to delocalized O p states that are mixed with Fe states at higher energies. Similarly, the two peaks in the $Li_3FeO_{3.5}$

spectrum can tentatively be assigned to the empty $3d$ states of Fe^{3+} and Fe^{4+} that hybridize with O $2p$, and also to O p mixed with Fe-d hybridization in the extended region. The fidelity of the $Li_3FeO_{3.5}$ structure model obtained from DFT calculation is thus corroborated by the close resemblance between the experimental and simulated O core-level spectra.

Therefore, the removal of the four Li ions can be expressed as following:

$$Li_5FeO_4 \rightarrow 2\ Li^+ + 2e^- + 0.25O_2(gas) + Li_3FeO_{3.5} \tag{5.5}$$

$$Li_3FeO_{3.5} \rightarrow 2\ Li + 2e^- + 0.75O_2(gas) + LiFeO_2 \tag{5.6}$$
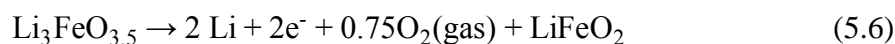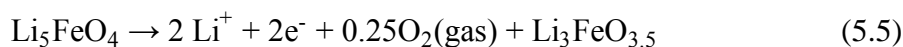
The number of O_2 molecules released per electron is 0.125 and 0.375 at 3.5V [equation (5.5)] and 4V [equation (5.6)] respectively, which is close to the DEMS results mentioned above. Based on the EELS and XANES results mentioned above, $Li_3FeO_{3.5}$ can be expressed as $Li_3(Fe^{3+}_{0.5}Fe^{4+}_{0.5})(O^{2-}_3O^-_{0.5})$, which is also consistent with charge states deduced from DFT (see below and Fig. 5.8). According to this electrochemistry, the lowest impedance of the cathode at around $x=2$ (Fig. 5.5) is originated from the high electrochemical activity of the Fe^{4+} and O^- in the $Li_3FeO_{3.5}$. In total, the removal of the first 2 Li^+ ions is charge-compensated by $1e^-$ from the formation of oxygen vacancies (0.5 O^{2-} to 0.25 O_2), 0.5 e^- from oxygen redox in the solid state (0.5 O^{2-} to 0.5 O^-), and 0.5 e^- from Fe redox (0.5 Fe^{3+} to 0.5 Fe^{4+}). Subsequently, 0.75 O_2 gas per formula unit is released from 0.5 O^- plus one O^{2-}, providing 2 e^- for the removal of another 2 Li ions and 0.5 e^- for the reduction of 0.5 Fe^{4+} back to 0.5 Fe^{3+}.
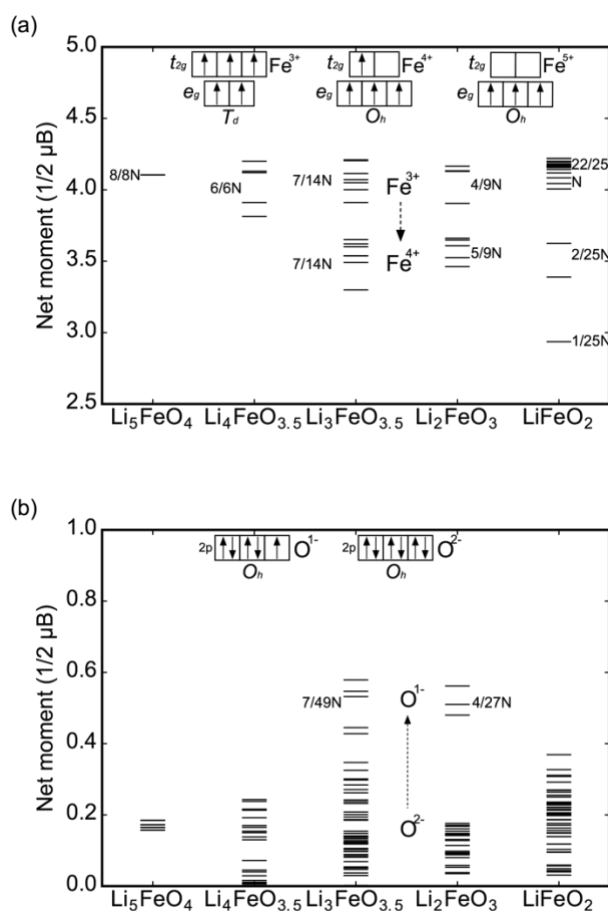
Figure 5.8 The magnetizations of (a) Fe ions and (b) oxygen ions in Li_5FeO_4, $Li_4FeO_{3.5}$, $Li_3FeO_{3.5}$, Li_2FeO_3 and $LiFeO_2$. The electronic configurations of Fe^{3+}, Fe^{4+}, Fe^{5+}, O^{1-} and O^{2-} are presented.

When comparing our results for LFO with those of layered oxides reported previously, we find that the potential for oxygen redox (~3.5 V *vs.* Li^+/Li) and O_2 release (4.0 V *vs.* Li^+/Li) in the LFO cathode is lower than that in the layered oxides (4.2 V and 5 V *vs.* Li^+/Li, respectively, for Li_4FeSbO_6).[12] One possible reason for the more facile oxygen redox is the difference in bonding or coordinate environment of the oxygen ions relative to the cation (Li/Fe) disordered sub-lattice in the DRP. Unlike conventional cubic cathode materials, which are well ordered and have only a single local environment for

oxygen ions, a variety of local oxygen environments exist in cation disordered rocksalt phases. Through systematically calculating and examining the DOS and charge/spin density around oxygen ions in various local environments using DFT, we demonstrate that the local configuration sensitively affects oxygen redox activity in LFO (Fig. 5.9).

The oxidation states of Fe and oxygen ions in the original Li_5FeO_4 and following delithiated phases ($Li_{5-x}FeO_{4-y}$): $Li_3FeO_{3.5}$, Li_2FeO_3 and $LiFeO_2$ were determined by comparing calculated magnetizations of Fe and oxygen ions with the number of unpaired electrons of the corresponding ions at each oxidation states. The numbers of unpaired electrons for Fe^{3+} (tetrahedrally coordinated), Fe^{4+} (octahedrally coordinated), and Fe^{5+} (octahedrally coordinated) are 5, 4, and 3 as shown in Fig. 5.8. In the original Li_5FeO_4 phase, the magnetizations are around 4.1 for all Fe ions implying an overall 3+ oxidation state. After 2 Li and a slight amount of O being extracted ($x = 2$, $y = 0.5$), seven Fe ions show magnetizations around 3.5 while the other seven remain around 4.1, indicating that half of the Fe ions have been oxidized to 4+. After 3 Li and 1 O per formula unit being extracted ($x = 3$, $y = 1$), the Fe magnetization distribution stays almost the same with the $Li_3FeO_{3.5}$ phase while four Fe ions show magnetizations around 4.1 corresponding to the oxidation state of 3+ and five Fe ions show magnetizations around 3.5 corresponding to the oxidation state of 4+. In the final phase ($x = 4$, $y = 2$), most Fe ions (22 of 25) show magnetizations around 4.1 corresponding to oxidation state of 3+ indicating the reducing of most Fe^{4+} by additional O removing. Three Fe ions show smaller magnetizations around 3.5 and 3 corresponding to oxidation states of +4 and +5, which are expected considering the complex local environments for specific Fe ions in the amorphous structure.

The magnetizations of oxygen ions in the original Li_5FeO_4 are close to 0 corresponding to an overall valence state of 2- for oxygen ions. After 2 Li and 0.5 O per formula unit being extracted ($x = 2$, $y = 0.5$), several oxygen ions (7 of 49) show increased magnetizations around 0.5 (Fig. 5.8b) indication the partially oxidation of O^{2-} to O^{1-}. With further Li and O removal ($x = 3$, $y = 1$), similar portion of oxygen ions (4 of 27) show increased magnetizations. In the final phase ($x = 4$, $y = 2$), magnetizations of oxygen ions show a relatively wide distribution corresponding to various oxygen ion local environments in the amorphous structure while no oxygen ions show increased magnetization, indicating the overall oxidation state of -2 for oxygen ions.

The atomic environments of Fe and O ions in cation-disordered pseudo-cubic phases $Li_3FeO_{3.5}$, and Li_2FeO_3 and their effects on the electronic states of O ions are examined and shown in Fig. 5.9, and 5.10. During the first delithiation step of Li_5FeO_4 with 2 Li and slight amount (0.5) of O removal, there is a concurrent phase transition from antifluorite to cation-disordered pseudo-cubic, which brings Li-excess O ion configurations (Fig. 5.9d) to the system. In the resulting $Li_3FeO_{3.5}$ phase, all the O^{1-} ions are identified to be in the particular "Li_6-O" configuration (Fig. 5.9d) with only Li ion coordination (first nearest neighbors) while the remain oxygen ions stay as O^{2-} with at least one Fe first nearest neighbor. The projected DOS (pDOS) of the oxygen $2p$ states and iron $3d$ states of these two configurations are shown in Fig. 5.9b-c. A much greater pDOS from the oxygen states than from the iron states between 0 and -3.5 eV of the Fermi level is found for the O^{1-} ion coordinated with six Li ions (Fig. 5.9b). The origin of this increased DOS can be identified by visualizing the charge density around the oxygen ion for the energy range between 0 and -1 eV (inset of Fig. 5.9b). This energy range corresponds to

the extraction of one electron. As seen in the isosurface plot, a large charge density resembling the shape of an isolated O $2p$ orbital is present along the directions where oxygen is linearly bonded to six Li (Li_6-O configuration). This result indicates that on further delithiation, the O^{1-} in the local Li-excess environment originate from this particular Li_6–O configuration can give out one labile electron and becomes O^0, similarly with previous study.[14] The irreversible delithiation from $Li_3FeO_{3.5}$ to Li_2FeO_3 and $LiFeO_2$, is proceeding by gradually oxidation of O^{1-} to O^0 and eliminating these specific Li_6-O configurations (Fig. 5.9d).
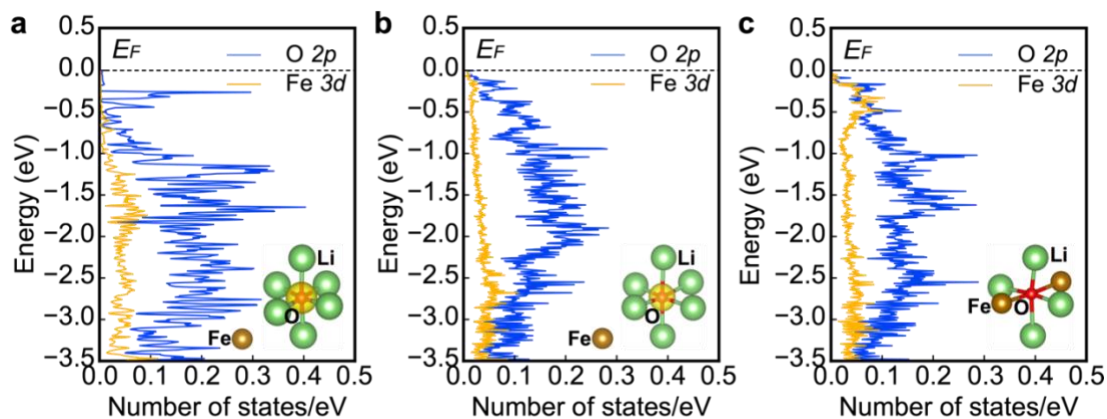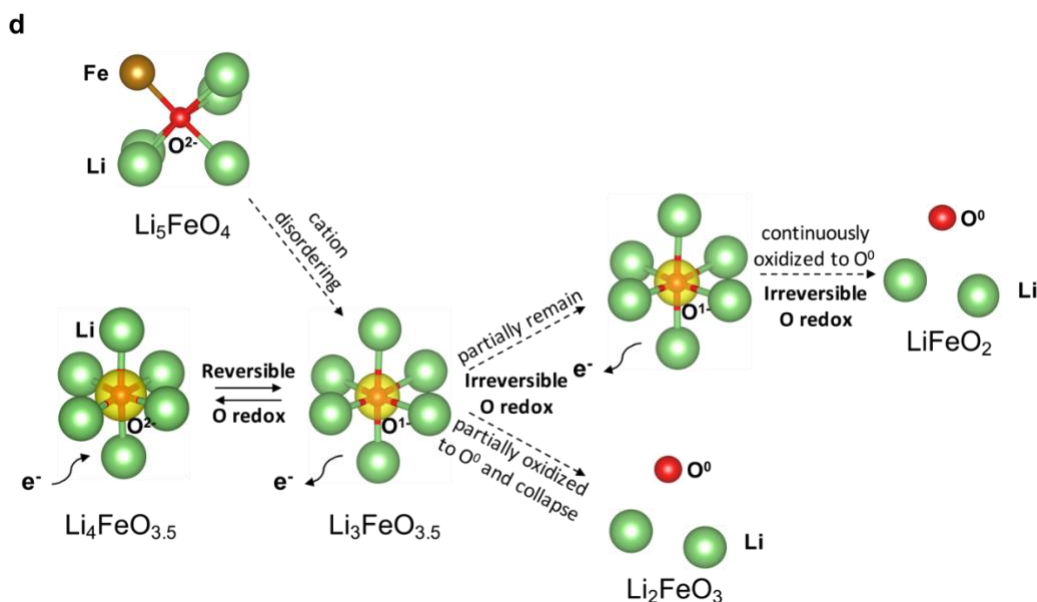
Figure 5.9 Effect of Li_6-O configurations on the electronic states of O ions in cation-disordered rocksalt phases. The Li_6-O configurations lead to the labile oxygen states. a-c, Projected density of states (pDOS) of the O $2p$ orbitals and Fe $3d$ orbitals of: a, O^{2-} ions in the Li_6-O configurations and nearest Fe ions in cation-disordered $Li_4FeO_{3.5}$, b, O^{1-} ions in the Li_6-O configuration and nearest Fe ions in cation-disordered $Li_3FeO_{3.5}$, and c, O^{2-} ions in Li/Fe-coordinated O configurations and nearest Fe ions in the cation-disordered $Li_3FeO_{3.5}$. Insets: isosurfaces of the charge density (yellow) around the oxygen ions in the energy range of 0 to -1.0 eV. Increased pDOS can be found near the Fermi level for the O ions coordinated by six Li, which originates from the particular Li_6–O configuration. d, Schematic of the role played by the Li_6-O configurations during the (de)lithiation of LFO. The irreversible delithiation from $Li_3FeO_{3.5}$ to Li_2FeO_3 and $LiFeO_2$ is accompanied by the oxidation of O^- to O^0 and subsequent elimination of the Li_6-O configurations. Meanwhile, the O^- ions in these Li_6-O configurations can be reversibly reduced to O^{2-} on further lithiation instead of delithiation. Thus, the O^-/O^{2-} redox can be reversible when the delithiation does not proceed beyond the point where Li_6-O configurations are eliminated.

5.3.4 Reversibility of the anionic and cationic redox

Figure 5.11 shows the cycle performance and the *in-situ* gas release measurements for LFO during cycling between 1.0 and 3.8 V after the first 2-Li-ion extraction. As shown in Fig. 5.11a, no obvious gas release occurred when the cell was cycled with the upper voltage limited to 3.8 V. On the contrary, the gas pressure increased every time the cell was charged to 4.0 V (Fig. 5.12a). In addition, the noticeable gas release at the 4.0 V plateau is maintained after several cycles between 3.8 V and 1.0 V, confirming that the oxygen ion redox couple stays in the solid cathode when it is cycled below 3.8 V after the first 2 Li extraction. The cathode showed stable capacity when cycled with the upper voltage limit at 3.8 V, but not 4.7 V (Fig. 5.11b and Fig. 5.12b).

To study the reversibility of the Fe^{3+}/Fe^{4+} redox couple, *in-situ* Fe K-edge XANES spectra were collected for the LFO cathode during the cycles after the first charge to 3.8 V, as shown in Fig. 13. During the discharge from 3.8 V to 1.0 V, the main Fe K-edge shifted back to around 7130 eV, confirming the reduction from $Fe^{(3+\delta)+}$ to Fe^{3+}. However, the typical tetrahedral Fe^{3+} peaks and edges of the original LFO (shown in Fig. 13a) were not recovered. This finding indicates that the octahedral $Fe^{(3+\delta)+}$ in the DRP does not move back to a tetrahedral site (in the original LFO phase) after being reduced to Fe^{3+}. The irreversibility of the Fe redox in the first charge and discharge is consistent with the asymmetric voltage-capacity profile in the first cycle. On the other hand, after the first charge to 3.8 V, the Fe K-edge XANES shows a nearly symmetric pattern between the 1st discharge and 2nd charge, as demonstrated in the 2D contour graphs (Figs. 13c and 13d), indicating that $Fe^{(3+\delta)+}/Fe^{3+}$ at the octahedral site can be reduced and oxidized reversibly.

According to the DFT simulations of the lithiated phase ($Li_{\sim4}FeO_{3.5}$), the pDOS

from the *2p* states of the oxygen ions in the center of the Li_6-O configurations, which are

inherited from the $Li_3FeO_{3.5}$, is confirmed to be greater than the pDOS from the *3d* states

of the nearest iron ions (Fig. 9a). Corresponding labile electron extraction/insertion from

these Li_6-O configurations enables the reversible O^{2-}/O^- redox. As about 1 Li ion

(corresponding to a capacity around 190 mAh/g) is involved in the first discharge and the

following cycling between 1.0 and 3.8 V, about 0.5 e$^-$ is provided by cationic redox (0.5

$Fe^{4+} \leftrightarrow 0.5\ Fe^{3+}$) and 0.5 e$^-$ is then provided by anionic redox (0.5 $O^- \leftrightarrow 0.5\ O^{2-}$).
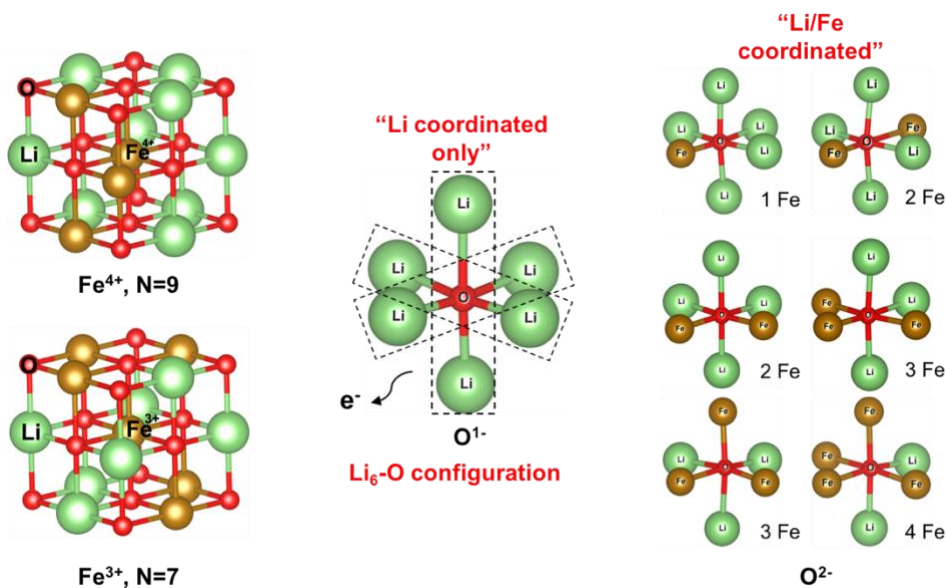
Figure 5.10 Local atomic environments for Fe and O ions in delithiated phases $Li_4FeO_{3.5}$,

$Li_3FeO_{3.5}$, and Li_2FeO_3.
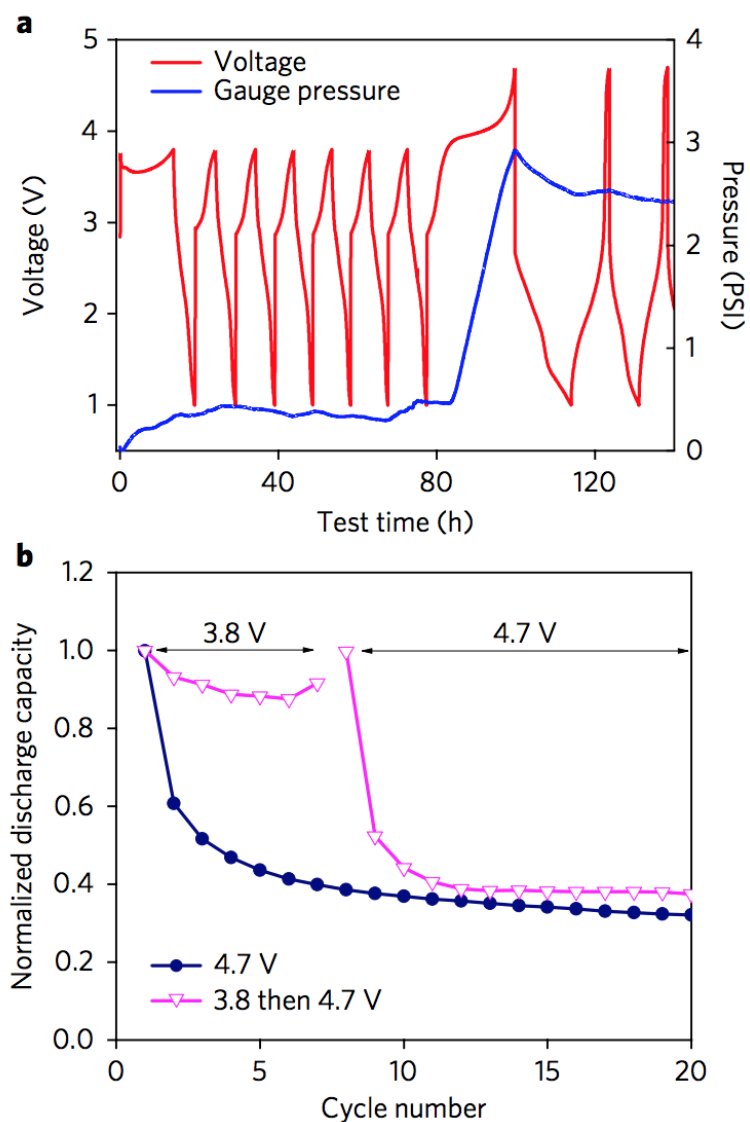
Figure 5.11 Onset voltage for O_2 gas release from Li_5FeO_4 a, The voltage profile (red line) and the *in-situ* pressure (blue line) of the Li_5FeO_4/Li cells during cycles with an upper cutoff voltage of 3.8 V. b, Performance of Li_5FeO_4 when cycled with a cutoff voltage of 3.8 V and then 4.7 V (magenta line, corresponding to cell in a versus at 4.7 V from the beginning (navy line)).
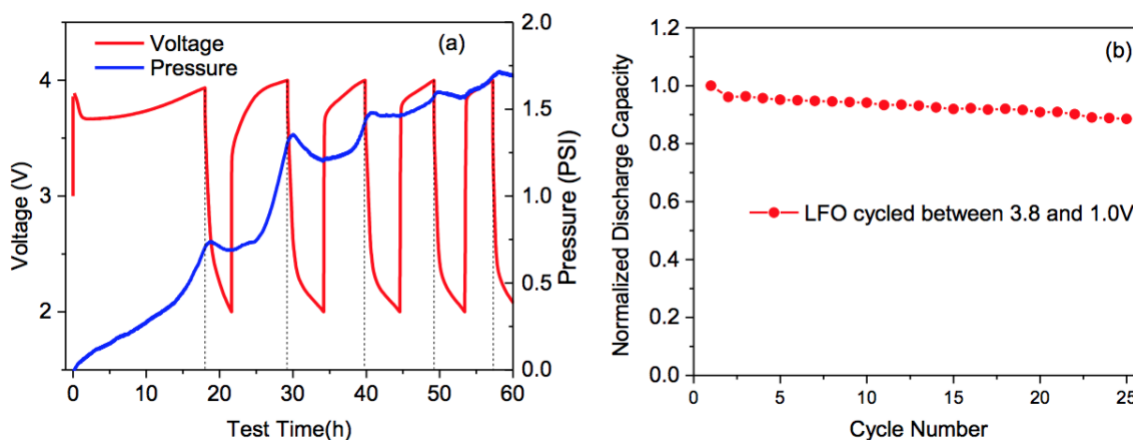
Figure 5.12 Additional characterization of the 3.8-1V cycling. a, *In-situ* pressure measurement with cutoff voltage at 4.0 V. The voltage profile (red line) and the *in-situ* pressure (blue line) of the Li$_5$FeO$_4$/Li cells collected during cycles with upper cutoff voltage at 4.7 V. b, Cycle performance of Li$_5$FeO$_4$/Li cell cycled between 3.8V and 1.0V.
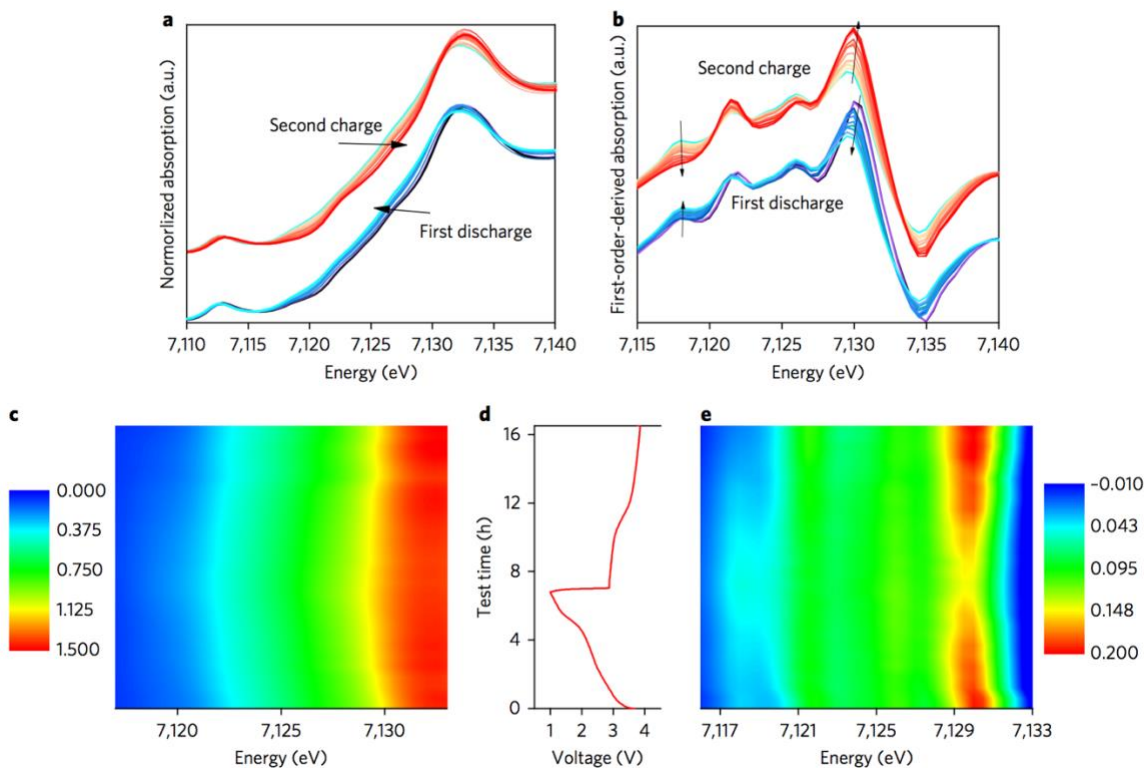
Figure 5.13 Reversibility of the Fe^{3+}/Fe^{4+} redox couple. a,b, Normalized (a) and first-order-derived (b) in situ Fe K-edge XANES collected on the LFO cathode during the first discharge and the

second charge after the initial charge to 3.8 V. c–e, 2D contour of a (c) and b (e), corresponding to

the charge–discharge curve (d).

5.4 Conclusion

Figure 5.14 summarizes the structural changes and redox reactions involved in the

electrochemical cycling of LFO. With the removal of two Li ions on the 3.5 V plateau, Fe

and Li ions migrate from tetrahedral sites to octahedral sites with a conversion from the

anti-fluorite to a disordered rocksalt phase. At the same time, part of the Fe^{3+} and part of

the O^{2-} are oxidized to Fe^{4+} and O^{-}, together with the formation of some oxygen vacancies.

The Fe^{4+}/Fe^{3+} and O^{-}/O^{2-} redox couples in the lattices are reversible with substantial

capacity retention in the subsequent cycles when the upper potential is limited to 3.8 V.

Charging beyond 2 Li ions results in the reduction of Fe^{4+} to Fe^{3+}, as well as O_2 gas release.
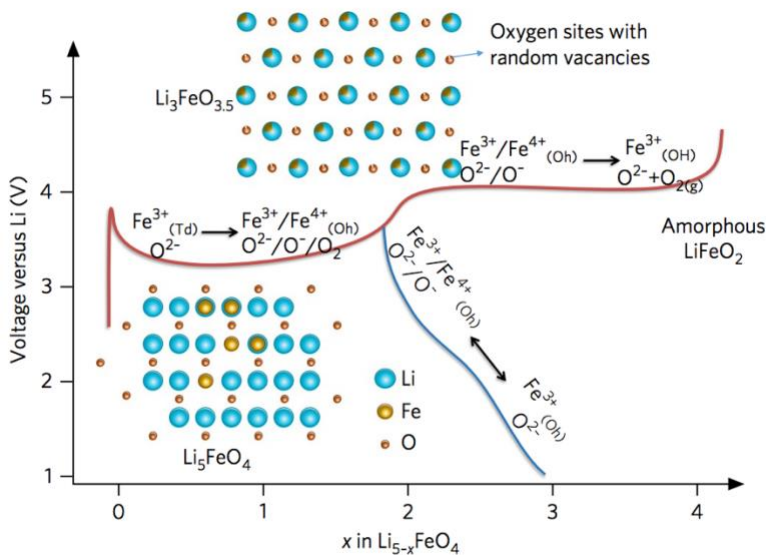
Figure 5.14 Schematic of the structural change and redox reactions in Li_5FeO_4 during

electrochemical cycling. For clarity, the structure of pristine Li_5FeO_4 is simplified as the standard

anti-fluorite structure by ignoring the position offsets of the atoms. The first charging voltage profile is plotted in red.

The pursuit of breaking the capacity limits has recently turns the research focus to the anionic redox. Fundamental research has been carried out on stabilizing oxygenate species by using $4d$ or $5d$ metal ions *via*, *i.e.* high M-O covalence; however, we believe that $3d$ metal oxides with lower cost and weight could be more practical in terms of real applications. The combined experimental and computational studies in this work demonstrate how the coordination structure and bonding environment enable the reversible oxygen redox in the $3d$ metal oxides. The Li_2O-like anti-fluorite structure facilitates oxygen redox potential lower than 3.8V, while the fully cationic disordered rock-salt phase generated in the charging stabilizes the oxygenate species (*i.e.* O^-) via Li_6O configuration. In fact, the Li_6-O configuration can be tuned in the oxides by controlling the Li/TM disordering which could be readily followed by further studies to realize improved capacities and stability in different electrodes. This extensive understanding of oxygen redox in different coordination environments could enable new pathways to next-generation, high-energy cathode materials based on simultaneous anionic and cationic redox chemistry.

CHAPTER 6 Interplay of Cation and Anion Redox in Li₄Mn₂O₅ cathode material and Prediction of Improved Li₄(Mn,M)₂O₅ Electrodes

6.1 Introduction

Recently, Freire *et al.*[173] reported a new disordered rocksalt-type Li-excess Li₄Mn₂O₅ cathode material with partially occupied cation and anion sites that exhibits a discharge capacity of 355 mAh g^{-1} in the first cycle within an operating voltage window of 1.2 to 4.2 V *vs.* Li/Li$^+$. On subsequent cycling, the material is reported to preserve its rocksalt structure with a discharge capacity of ~250 mAh g^{-1}. A complex delithiation mechanism was proposed, consisting of three possible redox couples: Mn^{3+}/Mn^{4+}, O^{2-}/O^{1-}, and Mn^{4+}/Mn^{5+}, based on magnetic susceptibility measurements[173], as shown in the *Eq.* (1):

$$Li_4Mn_2^{3+}O_5^{2-} \rightarrow 4Li^+ + 4e^- + Mn_x^{4+}Mn_{2-x}^{5+}O_{5-x}^{2-}O_x^{1-} \quad (0 \leq x \leq 2) \qquad (6.1)$$
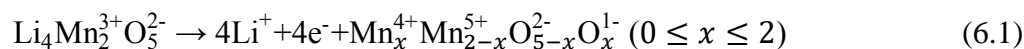
However, the formation of an octahedrally-coordinated Mn^{5+} (as in the rocksalt structure) during electrochemical delithiation is rather rare. Mn^{5+} ions are usually tetrahedrally-coordinated by oxygen atoms, such as in Li₃MnO₄.[191] Many factors can contribute to the difficulty of oxidizing Mn^{4+} to Mn^{5+} and here in this study we use the crystal field theory [192,193] to analyze the preference of Mn^{5+} toward tetrahedral coordination. For a given metal/ligand, the energy level splitting (Δ_{oct}) of a metal *d*-orbital by an octahedral field of ligands is larger than that caused by a tetrahedral field (Δ_{tet}), as schematically shown in Figure 6.1.[192,193] In addition, the ordering of the split energy levels, t_{2g} and e_g, in an octahedral field is opposite to that in a tetrahedral field. Consequently, the energy required to remove an electron from the low-lying t_{2g} levels of

an octahedrally-coordinated metal ion (ΔE_{oct}, see Figure 6.1) is significantly larger than that needed for removing an electron from the high-lying t_{2g} levels of a tetrahedrally-coordinated metal ion (ΔE_{tet}). Further, the energy needed to remove an electron from the high-lying e_g orbital ($\Delta E_{oct}'$) is much smaller compared to that needed to remove an electron from the t_{2g} orbital (ΔE_{oct}) in an octahedral field. As a result, the oxidation of octahedrally-coordinated Mn^{4+} to Mn^{5+} would require an impractically high voltage compared to the oxidation of octahedrally-coordinated Mn^{3+} to Mn^{4+}. Hence, it is therefore worth examining the TM/O redox mechanism in $Li_4Mn_2O_5$. Furthermore, the structural evolution and ionic coordination of redox active species in $Li_4Mn_2O_5$ during the (de-)lithiation is not completely understood, and also warrants further investigation. In addition, because of the difficulty of oxidizing Mn^{4+} to Mn^{5+}, improving the structural stability and electrochemical properties of $Li_4Mn_2O_5$ by doping or substitution of Mn with a different transition metal that can easily access an oxidation state greater than 4+ is an appealing prospect.

Here, we simulate the disordered rocksalt $Li_4Mn_2O_5$ structure through the special quasi-random structure (SQS) method (with Li/Mn mixing on the cation sublattice of rocksalt and O/vacancy mixing on the anion sublattice) and also determine the ground state ordered $Li_4Mn_2O_5$ structure *via* DFT-based calculations. The ordered structure as determined is predicted to have much lower energy (-119 meV/atom) compared to the disordered structure. Next, we investigate the structural evolution of phases during the delithiation of $Li_4Mn_2O_5$, and use these phases to study the redox activities during the delithiation reactions. We further elucidate the TM and O redox sequences of $Mn^{3+}/Mn^{4+}/Mn^{5+}$ and O^{2-}/O^{1-} during the charging cycle and show that the electrochemical

delithiation process of $Li_4Mn_2O_5$ occurs in the following three-step reaction pathway: *1)* initial oxidation of Mn^{3+} to Mn^{4+} for $Li_xMn_2O_5$ (4 > x > 2), *2)* followed by anionic redox of O^{2-} to O^{1-} for $Li_xMn_2O_5$ (2 > x > 1), and finally *3)* further cation oxidation of Mn^{4+} to Mn^{5+} for $Li_xMn_2O_5$ (1 > x > 0), validating the observations of Freire *et al.*[173]. Our calculations show that the oxidation of Mn^{4+} to Mn^{5+} imposes a migration of the Mn ion from its octahedral site to a nearby, unoccupied tetrahedral site and impairs the cycling performance of $Li_4Mn_2O_5$. Lastly, we perform computational screening of mixing on the Mn sites with metal cations (M) that produce energetically stable $Li_4(Mn,M)_2O_5$ mixtures, and also have stable 5+ oxidation states. Our approach suggests that alloying this compound with the following elements should produce new compounds with substantially improved electrochemical properties and cyclability: M = V and Cr in $Li_4(Mn,M)_2O_5$.
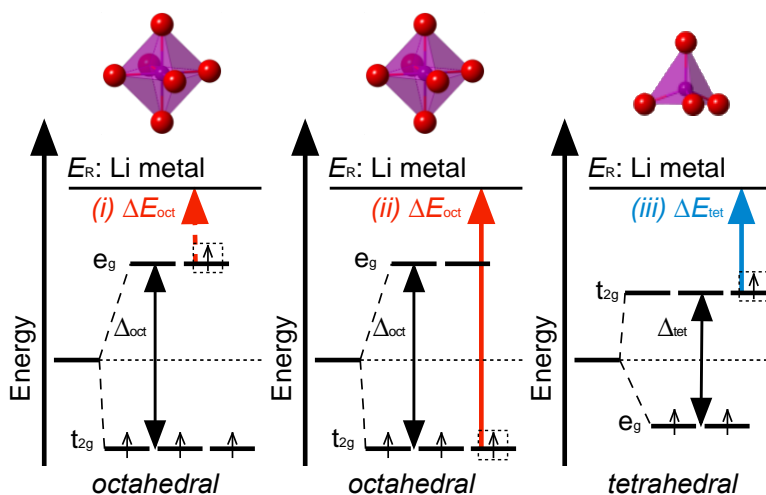
Figure 6.1 Energy levels of the Mn *d*-orbitals in octahedral and tetrahedral coordinations. The energies needed to oxidize octahedrally coordinated (i) Mn^{3+}(occupation: d^4) to $Mn^{4+}(d^3)$ and (ii) $Mn^{4+}(d^3)$ to $Mn^{5+}(d^2)$ to the reference state E_R (Li metal) are indicated by the dotted and solid red arrows, respectively. The energy needed to oxidize tetrahedrally coordinated (iii) $Mn^{4+}(d^3)$ to $Mn^{5+}(d^2)$ is indicated by the solid blue arrow. The energy ΔE_{oct} required to remove an electron from

the t_{2g} levels of octahedrally coordinated Mn^{4+} is significantly larger than that (ΔE_{tet}) needed to remove an electron from t_{2g} levels of tetrahedrally coordinated Mn^{4+}. The oxidation of octahedrally coordinated Mn^{4+} to Mn^{5+} is rarely observed.

6.2 Methodology

All DFT calculations reported in this study were performed using the Vienna Ab-initio Simulation Package (VASP)[103–106] with the projector augmented wave (PAW) potentials[107] and the Perdew-Becke-Ernzerhof (PBE)[108] exchange-correlation. A plane wave basis with a cutoff energy of 520 eV and Γ-centered k-meshes with a density of 8000 k-points per reciprocal atom were used for all calculations. All calculations were spin-polarized, with Mn atoms initialized in a high-spin configuration and relaxed to self-consistency. Both ferromagnetic (FM) and antiferromagnetic (AFM) configurations of the Mn ions were used to explore the ground state of $Li_4Mn_2O_5$ with the FM arrangement exhibiting lower energy (0.2 meV/atom). Therefore, the FM configuration was applied in following calculations. The DFT + U method introduced by Dudarev et $al.$.[109] was used to treat the localized $3d$ electrons of Mn with a U of 3.8, obtained by fitting it to experimental and calculated formation enthalpies in a previous study.[112] Phonon calculations were carried out with the frozen phonon approach as implemented in the PHONOPY package,[194] and phonon density of states was computed using a dense $30\times30\times30$ mesh in the irreducible Brillouin zone. Further, Heyd-Scuseria-Ernzerhof screened hybrid functional (HSE06)[195] was used to accurately determine the energies, magnetic and electronic states of Mn and O in the delithiated phases with structures relaxed using DFT + U: $Li_{4-x}Mn_2O_5$ ($x = 0, 1, 2, 3, 4$).

The tendency of two ordered rocksalt $Li_4M_2O_5$ and $Li_4M_2'O_5$ (space group *Cmmm*) materials to mix and form a mixed-metal rocksalt $Li_4MM'O_5$ structure can be evaluated by calculating the mixing energy as shown in *Eq.* (4):

$$E_{mix} = E(Li_4(M, M')_2O_5) - 1/2\big(E(Li_4M_2O_5) + E(Li_4M'_2O_5)\big) \tag{6.2}$$

where $E(Li_4(M, M')_2O_5)$, $E(Li_4M_2O_5)$, and $E(Li_4M'_2O_5)$ are the total energies of the *Cmmm* structure with two geometrically identical TM sites occupied by metal atoms M and M', M alone, and M' alone, respectively.

6.3 Results and discussion

6.3.1 Determining the rocksalt type structure of $Li_4Mn_2O_5$

Mechanical milling, as applied in the $Li_4Mn_2O_5$ experimental study[173] has been proven to be a viable solid state processing route for the synthesis of various equilibrium and non-equilibrium phases.[196] Structural disordering and thermodynamic metastability can be introduced to the synthesized compounds through ball milling, such as in the intermetallic $GdAl_2$ compound, [197] or in cation-disordered oxides Li_3NbO_4[44] and $Li_{1.25}Nb_{0.25}Mn_{0.5}O_2$.[198] $Li_4Mn_2O_5$ is claimed to adopt a disordered rocksalt type structure with Li/Mn randomly mixed on the cation sites and O/vacancies randomly mixed on the anion sites (see Figure 6.2a). Here, we employ the special quasi-random structure (SQS) method,[131,132,184] using a rocksalt-based 108-site supercell with Li/Mn occupying the 54 cation sites in a 2:1 ratio, and O/Vac occupying the 54 anion sites in a 5:1 ratio. The SQS was generated (see Figure 6.2b) using a Monte Carlo algorithm as implemented in the ATAT package[131,132,184] with the pair and triplet correlation functions of the SQS constrained to be identical to those of the statistically random compound (Li/Mn occupying

the cation sites, and O/Vac occupying the anion sites) at least up to the third nearest neighbor.

a
$Li_4Mn_2O_5$
disordered rocksalt
(Fm-3m)

O:5/6
Vac:1/6

Li:2/3
Mn:1/3

Li   Mn   O   Vacancy

b

$Li_4Mn_2O_5$, disordered (SQS, *P1*)

c

$Li_4Mn_2O_5$, ordered (*Cmmm*)

d

Relative energy (eV/atom)

SQS

Ordered
(*Cmmm*,
ground
state)

Proto-
type
(*Fddd*)
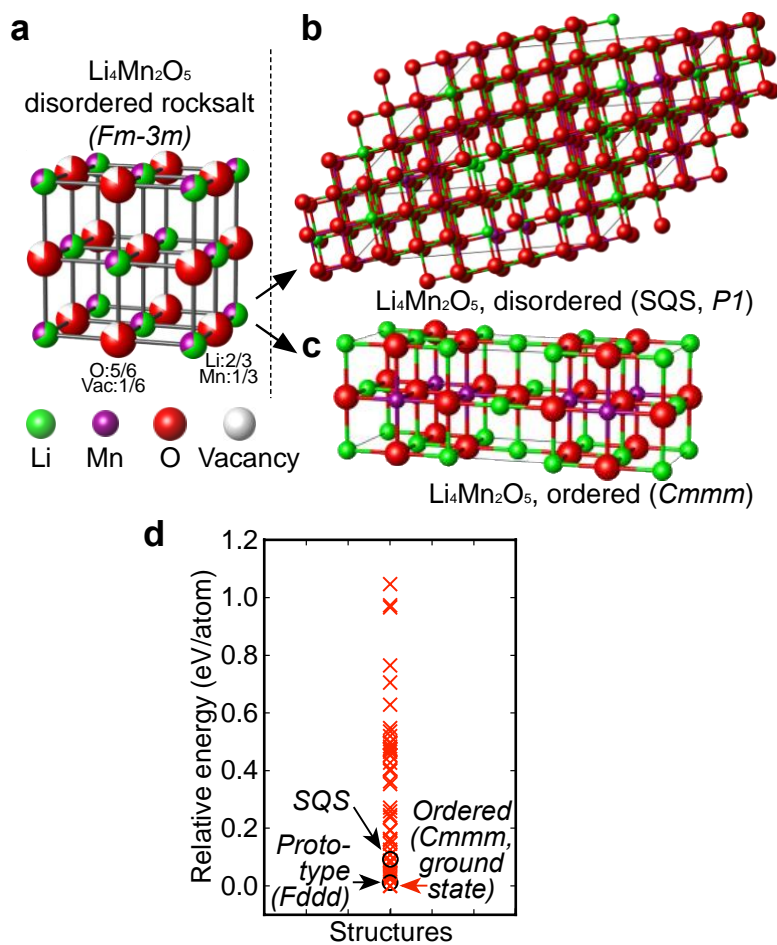
Structures

Figure 6.2. Determining the rocksalt type structure of $Li_4Mn_2O_5$. (a) A schematic illustration of the disordered rocksalt $Li_4Mn_2O_5$ structure with Li/Mn randomly mixed on the cationic sites and O/vacancy randomly mixed on the anionic sites. (b) Simulated disordered structure using the special quasi-random structure (SQS) method. (c) Predicted ground-state structure of $Li_4Mn_2O_5$, with all Mn octahedrally coordinated by O atoms and Li ions square-planarly or square-pyramidally coordinated because of oxygen vacancy neighboring (space group *Cmmm*). (d) Total energy distribution of the 100 structures selected, the SQS structure, and the $Na_4Mn_2O_5$ prototype structure

from DFT calculations. The *Cmmm* structure as predicted in this study exhibits the lowest total energy.

In addition, we also study ionic ordering in the $Li_4Mn_2O_5$ compound. We determine the lowest-energy, ground state structure of $Li_4Mn_2O_5$ by exploring a vast number of geometrically-distinct Li/Mn/O ordered configurations using DFT calculations. Starting from the cubic rocksalt primitive cell, we generate two sets of supercells: 1) containing 6 cations and 6 anions with all symmetrically distinct supercell shapes; 2) containing 12 cations and 12 anions with two specific shapes, given by $3\times2\times2$ and $2\times3\times2$ multiples of the primitive rocksalt unit cell. We then populate the cation sites with Li and Mn atoms in the ratio 2:1, and introduce vacancies (Vac) on the anion sites with a Vac:O ratio of 1:5. 616 geometrically different configurations were generated using the Enum code.[127–129] We calculated the electrostatic total energy for all configurations using nominal charge states for the ions in the system as a quick energy sampling step.[76] All structures were ranked by their normalized electrostatic energies, and the 100 $Li_4Mn_2O_5$ structures with the lowest electrostatic energies were fully relaxed, and their energies calculated, using DFT. We find the structure with the lowest DFT total energy, *i.e.*, the ground state structure of $Li_4Mn_2O_5$, has a space group of *Cmmm* with all Mn^{3+} ions octahedrally-coordinated by 6 oxygen atoms (see Figure 6.2c). Meanwhile, Li ions are square-planarly or square-pyramidally coordinated by 4 or 5 oxygen atoms as a result of oxygen vacancy neighboring. The cation ordering between Li and Mn in our proposed $Li_4Mn_2O_5$ ground state structure is the ordering of the Ga_2Zr compound[199] with crystallographic information given in Table S1. The fully-relaxed DFT energy of the SQS structure is found to be higher than the

ordered ground state by 119 meV/atom (34 ordered structures having lower total energies, see Figure 6.2d). We note that the isoelectronic compound, $Na_4Mn_2O_5$ is known and adopts an ordered rocksalt-type structure (*Fddd*).[200] Using this structure type for the Li compound, we find that $Li_4Mn_2O_5$ in the *Fddd* structure type exhibits a total energy 4 meV/atom higher than the *Cmmm* structure we found here. The thermodynamic and dynamical stability of the ordered Cmmm $Li_4Mn_2O_5$ structure is discussed in detail in the following section.

6.3.2 Li-Mn-O phase diagram and thermodynamic stability of ordered (*Cmmm*) $Li_4Mn_2O_5$

Phase diagrams represent the thermodynamic phase equilibria of multicomponent systems and provide useful information on reactions of phases. While the experimental determination of a phase diagram for specific system is significantly time and labor consuming, we can accelerate the phase diagram constructions by calculating energies of all known compounds in a specific chemical system using DFT, and using them to construct a $T = 0K$ convex hull.[118,119] In this study, we constructed ternary Li-M-O ground state convex hulls using the structures with the lowest energy for each composition for M = Mn and all metal elements with possible oxidation states of 5+ or above: *i.e.*, M = Bi, Cr, Ir, Mo, Nb, Os, Pd, Pr, Pt, Re, Rh, Ru, Sb, Ta, V, and W.[201] All compounds within each Li-M-O ternary system were adopted from the Inorganic Crystal Structure Database (ICSD).[120] The elemental reference states (Li, M, non-solid O_2) were obtained by fitting[121] to experimental formation energies, mainly from two major databases, the SGTE substance database (SSUB) and a database constructed by P. Nash *et*

al..[112,114,121–124] Calculations to construct equilibrium Li-M-O phase diagrams were carried out within the Open Quantum Materials Database (OQMD) framework.[113,114] We construct the convex hull of stable phases, *i.e.*, the set of compounds that have an energy lower than that of any other compound or linear combination of compounds at that composition, for each ternary Li-M-O system. Using such convex hulls, or $T = 0K$ phase diagrams, we can then evaluate the ground state stability of transition metal oxides, *e.g.*, $Li_4M_2O_5$ and $Li_4(Mn,M)_2O_5$, by using the GCLP technique.[35,114]
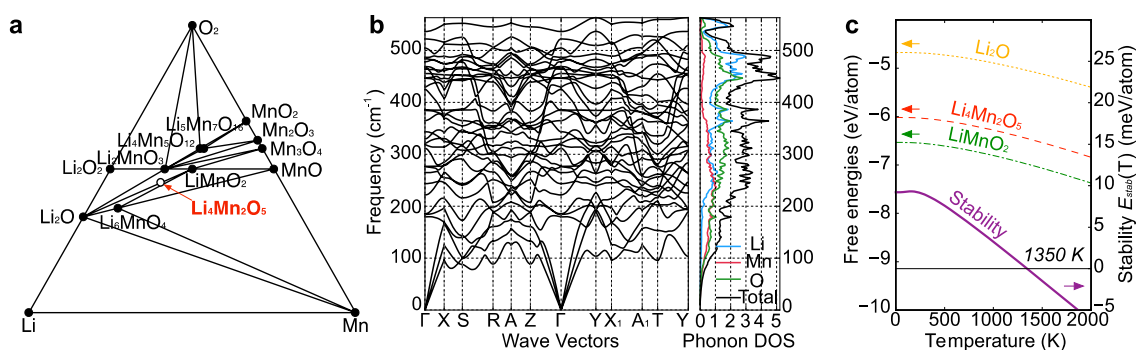
Figure 6.3 Thermodynamic and dynamic stabilities of $Li_4Mn_2O_5$. (a) Calculated Li–Mn–O (T=0 K) phase diagram. The $Li_4Mn_2O_5$ phase is slightly higher in energy (13.6 meV/atom) relative to that of the ground state phases—a mixture of Li_2O and $LiMnO_2$. (b) Phonon dispersion of ground-state $Li_4Mn_2O_5$ and (c) calculated temperature-dependent free energy of $Li_4Mn_2O_5$ (red dotted line), Li_2O (orange dotted line), and $LiMnO_2$ (green dotted line) as well as the stability (purple solid line) of $Li_4Mn_2O_5$ *vs.* temperature relative to Li_2O and $LiMnO_2$ phase mixtures. We find that $Li_4Mn_2O_5$ is dynamically stable and can be entropically stabilized at ~1350 K.

The Li-Mn-O phase diagram ($T = 0$ K) is shown in Figure 6.3a with the ground state, stable compounds marked by filed circles (*i.e.*, having lower energy than the linear

combination of other structures). $Li_4Mn_2O_5$ is shown as an empty circle, which is compositionally located on the tie-line between Li_2O and $LiMnO_2$. $Li_4Mn_2O_5$ at $T = 0$ K is predicted to have an energy only slightly higher (+13.6 meV/atom) than a two-phase mixture of Li_2O and $LiMnO_2$. The $Li_4Mn_2O_5$ compound is, therefore, not a ground state structure, but rather is unstable at $T = 0$ K, albeit by a very small energy. The compound is very close to the convex hull, and hence may be stabilized at elevated temperatures by entropic contributions, *e.g.*, vibrational entropy. Our DFT calculated phonon dispersion of the *Cmmm* $Li_4Mn_2O_5$ is provided in Figure 6.3b. No imaginary phonons are shown, which indicates our predicted $Li_4Mn_2O_5$ compound is dynamically stable.

By computing the harmonic phonons and vibrational entropies of $Li_4Mn_2O_5$, $LiMnO_2$, and Li_2O, we can calculate the temperature dependence of the free energies between these three competing phases. We find that $Li_4Mn_2O_5$ has a higher entropy than the combination of Li_2O and $LiMnO_2$, suggesting that $Li_4Mn_2O_5$ should become stable at elevated temperatures. The temperature-dependent free energy curves (Figure 6.3c, left), $F(T) = E - TS$, consist of the energy of a static lattice and the harmonic vibrational free energy at the same volume. Both Li_2O and $LiMnO_2$ are calculated to be dynamically stable, having only real phonon frequencies. Using the free energies for each of the three compounds, we can calculate the stability (formation free energy) for $Li_4Mn_2O_5$, $Stability(Li_4Mn_2O_5) = F(Li_4Mn_2O_5) - F(Li_2O) - 2F(LiMnO_2)$. The stability of $Li_4Mn_2O_5$ as the function of T is shown in Figure 6.3c with a temperature at which $Li_4Mn_2O_5$ is stabilized to be approximately ~1350 K. Due to the relatively small entropy differences between phases, the uncertainty of this temperature (*e.g.*, due to an uncertainty of ±1 meV/atom in free energy) results in a range of transition temperatures of 1240-1450 K. Our

calculations then suggest that the $Li_4Mn_2O_5$ compound is stable at high temperatures, implying the favored formation of this compound above the transition temperature. However, the elevated temperature would also favor ionic disorder because of the greater configurational entropy contribution. As a result of these thermodynamic arguments, we suggest that the synthesis of the ordered $Li_4Mn_2O_5$ compound might be difficult (though it has been accomplished for a disordered phase of $Li_4Mn_2O_5$ and an ordered compound of $Na_4Mn_2O_5$). The possible stable decomposition phases are $LiMnO_2$, Li_2O, Li_2MnO_3, Li_6MnO_4, as predicted by the Li-Mn-O phase diagram, which might be observed as "impurity" phases during synthesis.

6.3.3 Electrochemical delithiation process of $Li_4Mn_2O_5$ and TM/O redox competition

Having explored the structural ordering and thermodynamic stability of the $Li_4Mn_2O_5$ phase, we next explore the electrochemical delithiation process of this compound. To examine delithiation, we calculated the energies of disordered SQS-$Li_4Mn_2O_5$ and the fully-delithiated SQS-$Li_0Mn_2O_5$. Meanwhile, we consider compositions of $Li_xMn_2O_5$ ($x = 4, 3, 2, 1,$ and 0) in which $(4 - x)$ Li^+ ion(s) are removed from the original ordered *Cmmm* $Li_4Mn_2O_5$ structure using many geometrically-distinct configurations, and they are further relaxed using DFT. We evaluate the energies for these structures according to the following reaction: $Li_xMn_2O_5$ → Mn_2O_5 + xLi^+. The energies of these ordered/disordered delithiation products are plotted, and the delithiation convex hull of $Li_4Mn_2O_5$-Mn_2O_5 is then constructed, as shown in Figure 6.4a. In Figure 6.4a, the delithiation convex hull of $Li_4Mn_2O_5$-Mn_2O_5 is shown, where the ordered $Li_xMn_2O_5$ ($x = 3, 2, 1$) and disordered SQS-$Li_xMn_2O_5$ ($x = 0$) structures are found to be on the hull.

Converting the energies along this delithiation pathway into voltages, we find that voltage range obtained from our calculation well matches the interval as measured in the first experimental delithiation in Figure 6.4b.
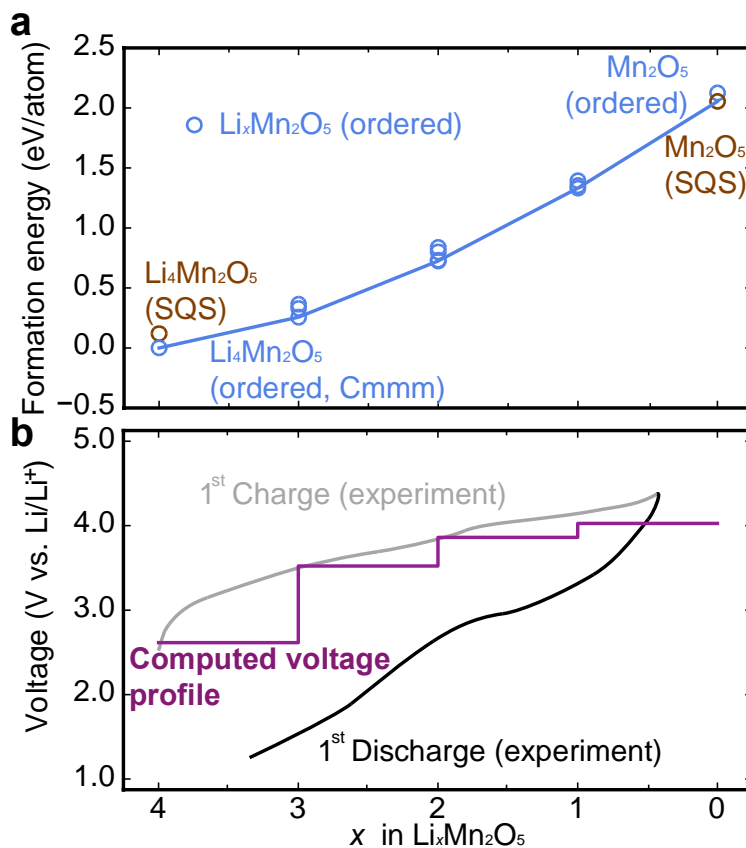
Figure 6.4 Electrochemical delithiation process of $Li_4Mn_2O_5$. (a) $Li_4Mn_2O_5$–Mn_2O_5 convex hull with calculated delithiated structures generated from ordered and disordered (SQS) $Li_4Mn_2O_5$ phase. (b) Corresponding voltage profile during the delithiation process in $Li_4Mn_2O_5$, the voltage range obtained from our calculation well matches the interval as measured in the first experimental delithiation [173].

We next use our calculations of the $Li_4Mn_2O_5$ phase and its delithiation products to interrogate in detail the TM/O redox sequence. We examine the oxidation states of Mn

and O ions during the delithiation process and investigate the local atomistic environments for cations and anions. The oxidation states can be determined by comparing calculated magnetizations of Mn and O ions with the number of unpaired electrons of the corresponding ions with known oxidation states. The numbers of unpaired electrons for Mn^{3+} (octahedrally-coordinated), Mn^{4+} (octahedrally-coordinated), and Mn^{5+} (tetrahedrally-coordinated) are 4, 3, and 2, respectively, as shown in Figure 6.6; and, the numbers of unpaired electrons for O^{2-} and O^{1-} (octahedrally-coordinated) are 0 and 1, respectively (Figure 6.6). We find that the electrochemical delithiation of $Li_4Mn_2O_5$ can be categorized in three different reaction steps, where each step contains a dominant redox of either TM or O ions:

(i) Cationic redox Mn^{3+}/Mn^{4+} delithiation ($Li_xMn_2O_5$, $4 > x > 2$): During the delithiation process of $Li_4Mn_2O_5 \rightarrow Li_3Mn_2O_5 \rightarrow Li_2Mn_2O_5$, we find that the Mn magnetizations decrease from 3.94 μ_B $\rightarrow$ 3.56 μ_B $\rightarrow$ 3.14 μ_B (see Figure 6.6), indicating an overall oxidation of Mn^{3+} to Mn^{4+}. Meanwhile, the O magnetizations retain a value between 0.01 μ_B to 0.14 μ_B (see Figure 6.6), implying a constant anion oxidation state of O^{2-}. The initial energetic preference of TM redox over O redox is confirmed by examining the projected density of states (*p*-DOS) of O 2*p* and Mn 3*d* orbitals (*e_g* and *t_{2g}*) of O^{2-} ions and Mn^{3+} ions in both ordered and disordered $Li_4Mn_2O_5$. As shown in Figure 6.5c, the contribution from Mn *e_g* to the valence band immediately below the Fermi level (E_F) is larger than that from O, which shows a preference for electron extraction from Mn (Figure 6.5b) during the initial stages of the charging process. As a result, the first delithiation step is dominated by cationic redox of Mn^{3+}/Mn^{4+}. It is interesting to connect the competition between cation

and anion redox to the local ionic environments in the $Li_xMn_2O_5$ structures. Recently, Seo *et al.*[14] proposed that a specific local Li-excess environment around the oxygen atoms (*i.e.*, a Li-O-Li linear configuration) is a key structural signature indicating the feasibility of both cationic (TM) and anodic (oxygen) redox process in Li-rich cathode materials. In other words, the electrons from the oxygen atom in this local Li-O-Li configuration can more easily contribute to the redox process due to the overlapping TM states and O $2p$ states. Interestingly, our examination of the local environments of oxygen shows that many O ions are in this Li-O-Li configuration in the ordered (*Cmmm*) and disordered structures, as shown in Figure 6.5a. However, we find that Mn^{3+} to Mn^{4+} cation oxidation is still the main redox contribution during the initial charging process. After 2 Li^+ ions are removed (*i.e.*, $Li_2Mn_2O_5$), a large fraction of O ions (4/5) still remain in these linear Li-excess environments (see Figure 6.5a). The *p*-DOS of O $2p$ and Mn $3d$ orbitals (e_g and t_{2g}) for O^{2-} ions in the Li-excess environment and nearest neighbor Mn^{4+} ions are shown in Figure 6.5d. The contribution from oxygen in the valence band immediately below E_F is significantly larger than that coming from Mn t_{2g}, implying the possibility of oxygen redox participation in the second delithiation step as described below. Taking extra electrons out from the t_{2g} orbital of Mn is significantly more difficult compared to the e_g orbital (Figure 6.5b), as discussed in Section I.
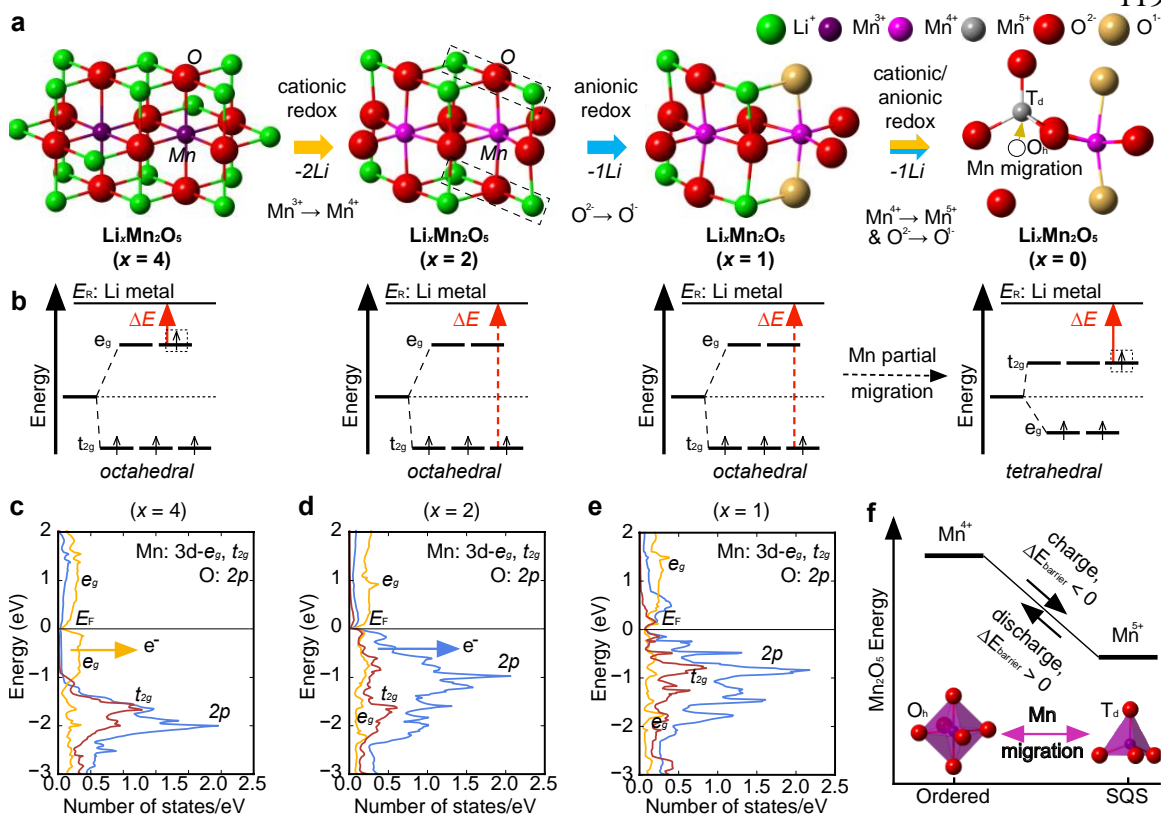
Figure 6.5 Cationic and anionic redox sequence during the delithiation of $Li_4Mn_2O_5$. (a) Local atomistic environments for Mn and O ions in $Li_xMn_2O_5$ (x = 4, 3, 2, 1, and 0). (b) Energies needed to oxidize octahedrally coordinated $Mn^{3+}(d^4)$ and $Mn^{4+}(d^3)$ and tetrahedrally coordinated $Mn^{4+}(d^3)$ to the reference state E_R (Li metal) (indicated by the red arrows). p-DOS of the O $2p$ and Mn $3d$ orbitals (e_g, t_{2g}) of O^{2-} ions in the 'Li–O–Li' configurations and the nearest Mn ions in (c) $Li_4Mn_2O_5$, (d) $Li_2Mn_2O_5$, and (e) $LiMn_2O_5$. (f) Energy difference between ordered and disordered Mn_2O_5 with the partial Mn migration from octahedral to tetrahedral sites. The redox reaction along with the $Li_4Mn_2O_5$ delithiation proceeds in three steps: *i*) cationic Mn^{3+}/Mn^{4+} ($4 > x > 2$), *ii*) anionic O^{2-}/O^{1-} ($2 > x > 1$), and *iii*) mixed cationic Mn^{4+}/Mn^{5+} and anionic O^{2-}/O^{1-} ($1 > x > 0$). The oxidation of Mn^{4+} to Mn^{5+} necessitates the migration of the Mn ion from its octahedral site to a nearby unoccupied tetrahedral site and impairs the reaction reversibility.
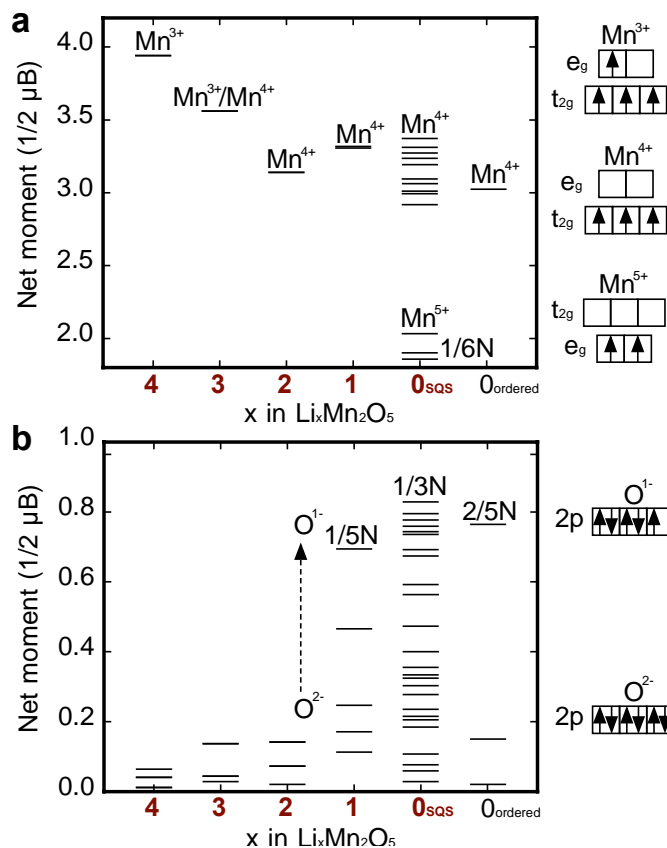
Figure 6.6 The magnetization and oxidation state evolution of (a) Mn and (b) O ions in intermediate phases $Li_xMn_2O_5$ ($x = 4$, 3, 2, 1, and 0) during delithiation. In nearly-delithiated intermediated phases ($x = 2$, 1, 0_{SQS}, $0_{ordered}$), oxidation states of Mn and O ions are not identical with the partition of certain oxidation state marked by fractions (*i.e.* 1/5N). Mn and O magnetizations show wide distribution in the $x = 0$ phase as a result of the various local environments of Mn in the disordered SQS structure. The electronic configurations of Mn^{3+}, Mn^{4+}, Mn^{5+}, O^{2-}, and O^{1-} are presented. Mn and O magnetizations in ordered Mn_2O_5 shown as a reference.

(ii) Anionic redox O^{2-}/O^{1-} dominant delithiation ($Li_xMn_2O_5$, $2 > x > 1$): Upon further delithiation of $Li_2Mn_2O_5$ into $LiMn_2O_5$, we find that the observed Mn magnetizations are largely constant in the range 3.14 μ_B to 3.30 μ_B, indicative of Mn^{4+}, consistent with the

experimental findings[173]. Here, the Mn ions still are octahedrally-coordinated. Interestingly, we find that 1/5 of the O ions exhibit magnetic moments around 0.69 μ_B, implying the partial oxidation of O^{2-} toward O^{1-}. By examining the local atomistic environments of all O^{1-} ions in $Li_1Mn_2O_5$ and comparing to their previous local environments in $Li_2Mn_2O_5$, we notice that all O^{1-} ions participating in redox during this step are located in the Li-O-Li Li-excess environments (Figure 6.5a), validating Seo *et al.*'s hypothesis.[14] Our calculations thus indicate the delithiation step from $Li_2Mn_2O_5$ to $LiMn_2O_5$ is dominated by anionic redox processes (*i.e.*, with O^{2-} being partially oxidized to O^{1-}). For the $LiMn_2O_5$ phase, as shown in Figure 6.5e, the contribution from Mn orbitals (mainly t_{2g}) to the valence band immediately below the Fermi level (E_F) is still slightly lower than that from O, implying a preference for electron extraction from O (Figure 6.5e) during the final stages of the charging process ($Li_xMn_2O_5$, $1 > x > 0$). However, in the experimental studies, further oxidation of Mn^{4+} to Mn^{5+} was observed during this stage.[173] Therefore, we suggest that some additional reaction mechanism must account for the Mn oxidation during the final stage.

(iii) Mixed cationic Mn^{4+}/Mn^{5+} and anionic O^{2-}/O^{1-} redox delithiation ($Li_xMn_2O_5$, $1 > x > 0$): During the final delithiation step, *i.e.*, $LiMn_2O_5$ to Mn_2O_5 (here, we examined the disordered SQS-Mn_2O_5 with the lowest DFT energy), we find the Mn magnetizations are distributed from 3.3 μ_B to 1.9 μ_B (see Figure 6.6), indicating that Mn^{4+} ions have been partially (1/6) oxidized to Mn^{5+}. At the same time, the magnetizations of 1/3 of the O ions are found to be 0.71 μ_B ~ 0.82 μ_B (Figure 6.6), implying a further oxidation of O^{2-} to O^{1-} (remember that we find 1/5 of anions are O^{1-} in $LiMn_2O_5$). The coexistence of Mn^{5+} and O^{1-} is consistent with the experimental observations in *Ref.* [173]. Interestingly, as depicted

in Figure 6.5a, we find that all the Mn^{5+} ions are tetrahedrally-coordinated in this Mn/Li vacancy disordered configuration. The observation of tetrahedrally-coordinated Mn^{5+} confirms our discussion above that the oxidation of tetrahedrally-coordinated Mn^{4+} to Mn^{5+} is energetically favored compared to the octahedrally-coordinated Mn^{4+} because of the crystal field t_{2g}/e_g effects (Figure 6.5b). Therefore, we suggest that the Mn ion migration to tetrahedral positions is necessary in the final delithiation process toward Mn_2O_5, which corresponds to the oxidation of Mn from 4+ to 5+. At the same time, all the Mn ions in our ordered Mn_2O_5 (blue circle in Figure 6.4a, 0.85eV/Mn higher in energy compared to the disordered configuration), however, are still located in the octahedral sites, where the oxidation states are preserved at 4+, as shown in Figure 6.6. As a result, the Mn migration not only enables the Mn^{4+} oxidation to Mn^{5+} but also lowers the energy of the system at this stoichiometry by 0.85eV/Mn (see Figure 6.5f). In order to achieve a reversible redox reaction, these Mn^{5+} ions would need to migrate back to their original octahedral sites during the following lithiation (*i.e.*, the discharge process). The large reverse migration barrier (*i.e.*, at least 0.85 eV/Mn, the difference in DFT energetic stability between these two structures) will result in a significant kinetic barrier for the tetrahedral Mn^{5+} to migrate back to its original octahedral position; therefore, we suggest that this metal migration will impair the reversibility of the reaction. After the extended cycling of $Li_4Mn_2O_5$ cathodes, it is likely that more Mn ions will migrate into the in tetrahedral sites and get trapped. We suggest that the phase transformation caused by the Mn ion migrations could be one of the most significant factors for the polarization between charge and discharge, as well as the capacity fade observed experimentally after the first cycle[173]. We also suggest that

improved performance and reversibility should be achieved by limiting charging to avoid the formation of Mn^{5+} and hence the migration of these metal cations.

The above results imply a design strategy to improve the extended cyclability of the rocksalt $Li_4Mn_2O_5$ cathodes would be to avoid Mn migration to the tetrahedral sites during the Mn^{4+}/Mn^{5+} redox process. The electrochemical cycling of $Li_4Mn_2O_5$ can be confined to a smaller range: $Li_xMn_2O_5$, $4 > x > 1$, without removing all Li from the system and oxidizing Mn to 5+. Thus, improved cyclability could be achieved by sacrificing a limited amount of capacity. An alternate strategy to achieve this goal of improved reversibility would be to partially substitute Mn in $Li_4Mn_2O_5$ with other TM elements that can access the oxidation state of 5+ or above, thereby eliminating the need for oxidation of Mn to 5+. In the following section, we present a high-throughput DFT screening strategy to determine stable metal dopants (M) in $Li_4(Mn,M)_2O_5$ compounds.

6.3.4 TM doping in $Li_4Mn_{2-x}M_xO_5$ with accessible 5+ oxidation state or above

We first start with all the metal elements (M) with possible oxidation states of 5+ or above: *i.e.*, M = Bi, Cr, Ir, Mo, Nb, Os, Pd, Pr, Pt, Re, Rh, Ru, Sb, Ta, V, and W.[201] For each of these elements, we compute the properties of mixed-metal $Li_4(Mn,M)_2O_5$ compounds, specifically focusing on stability and mixing energy. The mixing energies between $Li_4Mn_2O_5$ and $Li_4M_2O_5$ in $Li_4(Mn,M)_2O_5$ help determine the stability of metal mixing in this structure. When the mixing energy (E_{mix}) is found to be slightly negative or positive (near-zero, *i.e.* -30 to 30 meV/site), the mixing entropy at finite temperatures will overcome the mixing energy, and hence there will be a tendency for metal mixing in a solid-solution. A larger positive mixing energy (> 30 meV/site) or a larger (in magnitude)

negative mixing energy (< -30 meV/site) would lead to phase separation in the former case, and a quaternary ordered compound in the latter. These cases may have undesired phase transformations or possible mass transport kinetic limitations. As a result, we narrow down the list of our candidates to those with near-zero mixing energies between -30 to 30 meV/site in our study (Figure 6.7). Similar with $Li_4Mn_2O_5$, all $Li_4M_2O_5$ compounds are unstable at T = 0K with the potential to be entropically stabilized at finite temperatures. For cases where the $Li_4M_2O_5$ convex hull distance (*i.e.*, stability) is significantly positive, it will lead to an instability of the corresponding $Li_4(Mn,M)_2O_5$ compound. Here we also exclude the $Li_4(Mn,M)_2O_5$ compounds with related $Li_4M_2O_5$ convex hull distance larger than 50 meV/atom. In Figure 6.7, we suggest the top $Li_4(Mn,M)_2O_5$ candidates with stability near the convex hull and a small mixing energy in the Mn sublattice (favoring solid solution formation). We predict that mixing with M = V and Cr are particularly promising additives. We expect that the doping/substitution of these elements into $Li_4(Mn,M)_2O_5$ cathodes will lead to reduced phase transformation and controlled oxygen anodic chemistry for further improved electrochemical performance; therefore, calling for imminent experimental validations.
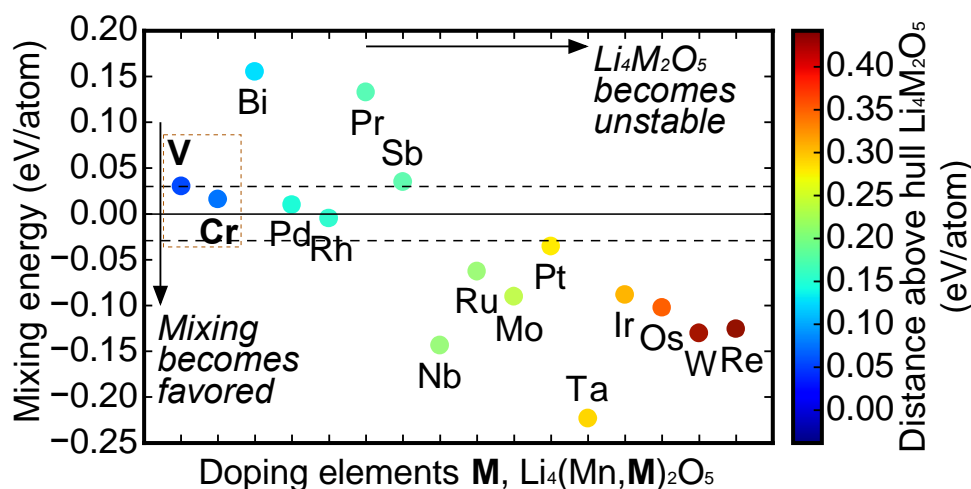
Figure 6.7 HT-DFT screening for doping into the Mn sublattice in the $Li_4(Mn,M)_2O_5$ cathode system. We performed computational screening of mixing on the Mn sites with metal cations (M) that produce energetically stable $Li_4(Mn,M)_2O_5$ mixtures and have stable 5+ oxidation states by examining the mixing energy and $Li_4M_2O_5$ stability. The top candidates with $-30 < E_{mix} < 30$ meV/site and the lowest formation energies are presented. Our top three TM dopant candidates in the $Li_4(Mn,M)_2O_5$ system are located in the left center of the plot: M = V and Cr.

6.4 Conclusion

In this study, we exploit the structural and electrochemical properties of Li-rich rocksalt $Li_4Mn_2O_5$ cathode materials using first-principles DFT calculations. We simulate the disordered rocksalt-type $Li_4Mn_2O_5$ structure using the special quasi-random structure method (SQS). Then we identify the ground state structure of $Li_4Mn_2O_5$ using an enumeration method by exploring geometrically-distinct Li/Mn and O/vacancy configurations on cation and anion sites of the rocksalt structure, respectively. The ordered structure is predicted to have much lower energy compared to the disordered structure. We reveal the underlying mechanism in the electrochemical delithiation process of $Li_4Mn_2O_5$ that proceeds through a three-step reaction with a different dominant cationic/anionic redox process in each step: *i*) $Li_xMn_2O_5$ ($4 > x > 2$; Mn^{3+}/Mn^{4+}), *ii*) $Li_xMn_2O_5$ ($2 > x > 1$; O^{2-}/O^{1-}), and *iii*) $Li_xMn_2O_5$ ($1 > x > 0$; Mn^{4+}/Mn^{5+}). We find that the oxidation of Mn^{4+} to Mn^{5+} can be achieved by the Mn ion migrations from the octahedral to the adjacent tetrahedral sites. A large barrier for Mn migration back to the octahedral site in the following lithiation process impairs the reversibility of the redox processes, which directly explains the capacity fades observed in $Li_4Mn_2O_5$ after the 1st cycle in experiment. Lastly, in order to improve the extended cyclability of $Li_4Mn_2O_5$ cathode system, we search for a suitable

dopant that can access the oxidation state of 5+ or above by evaluating the mixing energies and stabilities. We recommend the dopant candidates including M = V and Cr in $Li_4(Mn,M)_2O_5$ system for further experimental investigations. Our theoretical findings provide valuable insights on the structural and electrochemical behavior of Li-rich $Li_4Mn_2O_5$ cathode materials and could help designing the next-generation high-energy-density LIB cathode materials for future research and development.

CHAPTER 7

Cubine, a Novel 2-Dimensional Nano Sheet Based Superfast Rate Electrode for Lithium Ion Batteries

7.1 Introduction

Since the first successful exfoliating of graphene in 2004,[38,202–204] intense research has been devoted to the synthesis and characterization of 2D materials. Meanwhile, various 2D materials have been discovered, ranging from graphene analogs like silicene[205–208] to phosphorene[209] and borophene,[210] transition metal oxides,[211,212] transition metal dichalcogenides,[165,213] and transition metal carbinides/nitrides.[214,215] Due to their diverse properties, 2D materials have been considered for energy storage. For metal-ion batteries, materials that can host Li^+ or Na^+ at high densities are of particular interest, a market currently dominated by carbonaceous (*e.g.* graphite and hard carbon) and layered materials (*e.g.* $LiCoO_2$).[216] 2D materials are promising alternatives since they exhibit compelling ion transport and storage characteristics due to their open 2D channels and high specific surface areas with a large number of active sites.[216] Furthermore, since 2D materials only exhibit weak interlayer bonding *via* van-der-Waals (vdW) forces, unfavorable, large changes in their volumes during the intercalation and de-intercalation of lithium ions are alleviated. 2D materials can also serve as functional substrates for incorporating active materials to improve the electrical and ionic conductivity of electrodes.[38]

Theoretical efforts to identify potential new 2D materials have been aimed at screening large databases of crystalline materials for low-dimensional structural patterns.[217] Commonly, simple geometrical criteria such as large interlayer spacings are used to identify 2D units that could be separated through mechanical exfoliation. Recently, a high-pressure phase in the Cu–Bi system, CuBi, was discovered with an orthorhombic unit cell (Figure 7.1).[218] Despite being known to exhibit superconducting properties with a Tc between 1.33 and 1.40 K,[219] CuBi structure featured with voids to host the lone electron pairs (LEP) of the two nonbonding Bi 6s electrons that form in the vicinity of the bismuth atoms. Therefore, CuBi forms a 2-dimensional layered structure of alternating Cu, Bi, and LEP sheets.
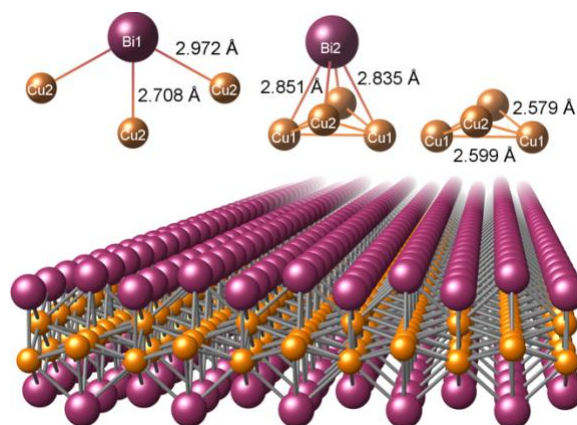
Figure 7.1 Single sheet of cubine, exfoliated from CuBi, along the a-axis, together with the interatomic bonds. The two symmetrically inequivalent atoms Bi1 and Bi2 are attached to the buckled triangular sheet of Cu through three and four bonds, respectively. The core Cu sheet itself consists of a triangular lattice with two distinct short Cu−Cu bonds. In all figures, Cu and Bi atoms are denoted by orange (small) and purple (large) spheres.

Here we investigate the CuBi compound using ab initio methods to unravel the unique structural features of CuBi and reveal its 2-dimensional character. The dynamical

stability of CuBi nano sheets show that they are viable as metastable phases, and could be potentially used as a new class of building blocks in 2D heterostructures with compelling physical properties: they are superconducting with a Tc $\approx$ 1 K, and could be used to intercalate Li atoms at low voltages, and hence make an interesting new electrode for Li-ion batteries.

7.2 Methodology

Density functional theory (DFT) calculations were carried out within the projector augmented wave (PAW) formalism61 as implemented in the VASP[103–106] package. Unless otherwise noted, we employed the Perdew−Burke−Ernzerhof (PBE) approximation[108] to the exchange− correlation potential. A plane-wave cutoff energy of 400 eV was used with a sufficiently dense k-point mesh to ensure a convergence of the total energy to within 1 meV/atom. Both the atomic and cell parameters were simultaneously relaxed until the maximal force components were less than 2 meV/Å and stresses less than 0.01 GPa.

The Li adsorption process on the cubine single layer was computed by exploring geometrically distinct Li/vacancy configurations on all possible adsorption sites of the cubine surface at different compositions (Li/vacancy ratios). Starting with the cubine unit cell (Cu_4Bi_4) which has a total of eight empty sites where Li ions can adsorb, we generated all symmetrically distinct configurations using Enum[127,220] for a series of compositions $Li_x\square_{2-x}CuBi$ ($0 < x < 2$, $\square$ denoting vacancies). The total energies of all configurations were evaluated with the DFT settings described earlier. We also adopted the vdW-DF

functional (optB88),[221] which employs a self-consistent van der Waals (vdW) correction.

At each composition x the adsorption energy was computed according to

$$E_{ads} = \frac{E(Li_xCuBi) - xE(Li) - E(CuBi)}{x} \qquad (6.1)$$

where the reference energy E(Li) of a single Li was evaluated in vacuum using a 10 Å ×

10 Å × 10 Å supercell. To simulate the lithiation process of bulk CuBi, the conventional

cell was used to explore geometrically distinct potential Li sites between the cubine layers.

All symmetrically inequivalent occupation of these sites was used as input structures and

relaxed with respect to the atomic and cell variables using the PBE functional, resulting in

energies as a function of Li/vacancy ratios, *i.e.*, the Li concentrations in Li_xCuBi. The

formation energies were evaluated according to the following reaction: CuBi + xLi →

Li_xCuBi. The lithiation convex hull was constructed from the lowest formation energies at

every composition, and only those intermediate phases which lie on the hull were

considered, using metallic Li as a reference.

7.3 Results and discussion

Due to their large surface areas, 2D materials such as graphite have recently

attracted interest as additives to enhance the performance of electrodes in metal-ion

batteries.[222] Here, we investigate the potential of using cubine sheets in lithium-ion

batteries by studying the adsorption of Li atoms directly on its surface. We identified three

symmetrically distinct sites on cubine where Li can be deposited, shown in the top right

inset of Figure 7.2a. We systematically explored all possible decorations of these three sites

on both sides of a cubine sheet in one unit cell of Li_xCuBi. For $x = 0.25$ (*i.e.*, one Li per

cell), the most favorable adsorption sites are A and B, which are located between four Bi

atoms and lead to adsorption energies per Li atom of 1.90 and 1.88 eV, respectively. Site C is energetically unfavorable and can only be occupied once both the A and B sites are completely filled at higher values of x. A full occupation of all sites results in Li_2CuBi, and a potential gravimetric charge density of 192.92 mA h/g. Figure 7.2a shows the lowest energy adsorption geometries together with the change in adsorption energies as a function of surface coverage.

In practical energy storage applications, the kinetics of the adsorbed species on a surface is an important factor in the rate of charge/discharge. Hence, we computed the diffusion barriers of Li along the geometrically distinct paths on the cubine sheet (Figure 7.2b). The lowest barrier was found for the pathway A−B with a height of merely 0.13 eV, which is 40% lower than the barrier between the two most stable adsorption sites of Li on graphene.[223] Since the A−B sites form a network on the surface connected through these low energy barriers, we expect that the Li atoms can diffuse at a high rate on the surface. The energy profile for the paths A−C and B−C show that the C site is indeed a stationary saddle point (between A−A and B−B sites), which only transforms into a local minimum once the A and B sites are occupied.
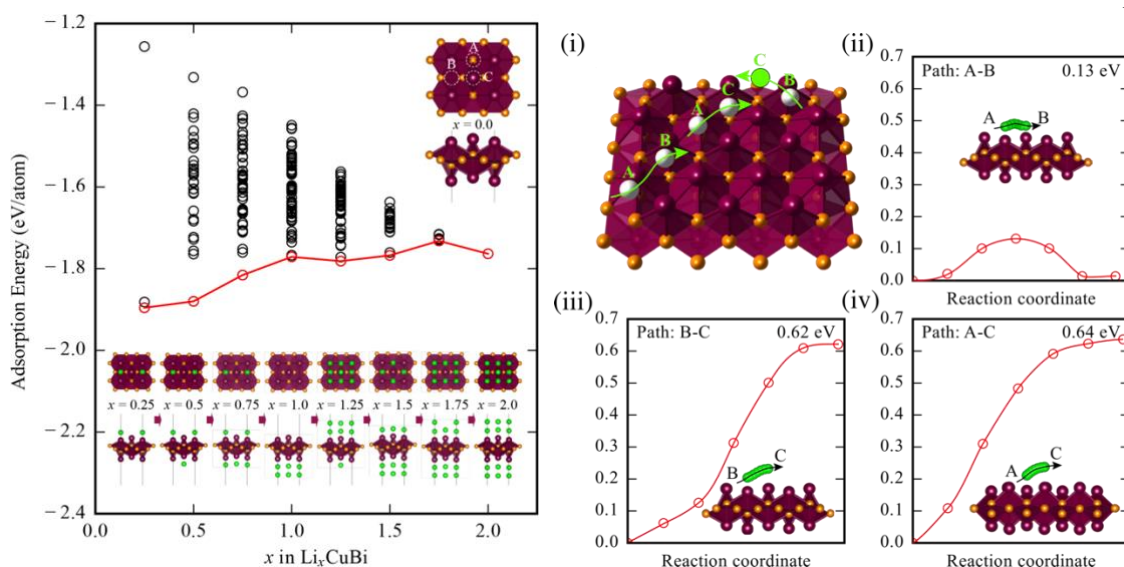
Figure 7.2 (a) Adsorption energies per Li atom of Li$_x$CuBi on a single sheet of cubine at various coverage densities x, where the red line connects the lowest energy configurations at a given x. The three distinct adsorption sites are denoted with A, B, and C (top right inset), and the lowest energy adsorption geometries at different surface coverages are shown by the insets at the bottom. (b) Calculated Li kinetics on a single sheet of cubine. Subpanel I shows the lithium-ion diffusion pathways on the surface. Subpanels ii−iv show the kinetic barriers calculated along geometrically distinct diffusion pathways: A−B, B−C, and A−C.

The very low interlayer binding energy, the large spacing of 3.98 Å (graphite, 3.35 Å) between the sheets, and the low diffusion barriers of Li on cubine also render bulk CuBi potentially an attractive candidate as a metal intercalation electrode. There are two symmetrically distinct interstitial sites per cell (inset of panel i, Figure 7.3a) with each 2-fold degeneracy between the cubine layers that can host four guest atoms in total. By fully occupying these sites with Li, Na, Mg, and Al, gravimetric (and volumetric) capacities of 96.46 mA h/g (493.25 mA h/mL), 92.45 mA h/g (472.75 mA h/mL), 184.27 mA h/g (942.27 mA h/mL), and 274.51 mA h/g (1403.72 mA h/mL) could be potentially achieved,

respectively. Although the gravimetric capacities of bulk CuBi are rather moderate, the volumetric capacities are close to values of commercially used anode materials such as graphite (550 mA h/mL). Besides a high capacity, there is an increasing demand for electrode materials with high rate capacities to improve battery power and to reduce the (re)charge time. To assess these charge/discharge and ion diffusion properties, we investigated the lithiation electrochemistry of CuBi. There are two intermediate phases on the CuBi−Li convex hull, where the end points are given by CuBi and elemental metallic Li, as shown in panel I of Figure 7.3a: $Li_{0.5}CuBi$ and LiCuBi. The corresponding voltage profile is shown in panel ii, with values in a fairly low range of 0.18−0.34 V, indicating that this material is more suitable as an anode material. During the whole lithiation process, the CuBi backbone remains completely intact with only a slight sliding of the cubine layers against each other around the concentration $Li_{0.5}CuBi$ (see panel iii in Figure 7.3a).
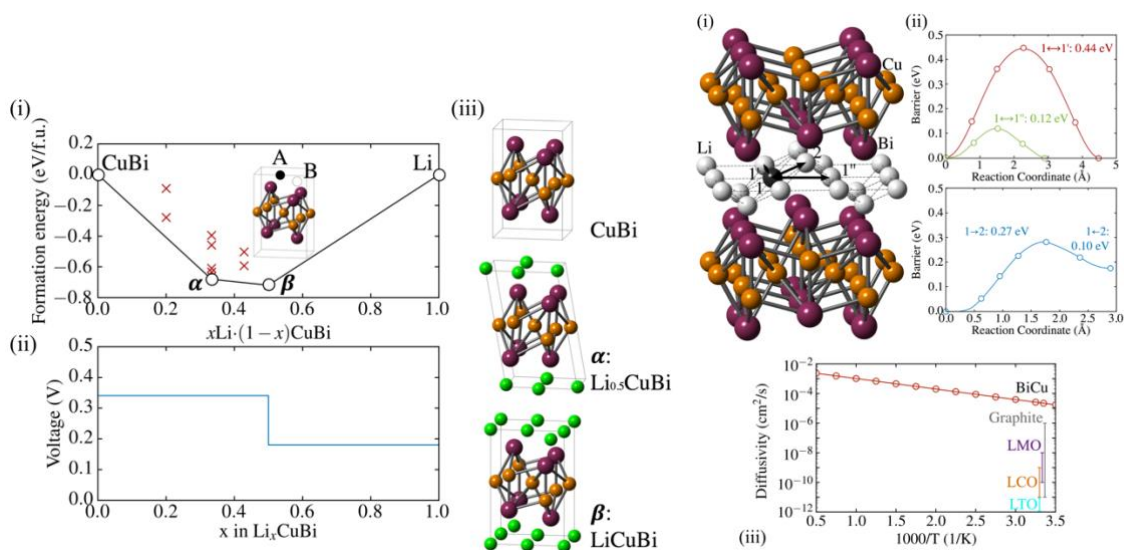
Figure 7.3 (a) PBE results of the CuBi-Li convex hull of stability as a function of lithium concentration (i) and the corresponding voltage profile (ii). Predicted structures of the intermediate

phases are shown in iii. (b, i) Lithium-ion diffusion network through the interlayer space of CuBi; (ii) kinetic barriers calculated along geometrically distinct diffusion paths using PBE; (iii) calculated lithium-ion diffusivity as a function of temperature (attempt frequency, $v = 10^{13}$ s^{-1}), compared to state-of-the-art anodes (graphite and LTO ($Li_4Ti_5O_{12}$)) and cathodes (LCO ($LiCoO_2$) and LMO ($LiMn_2O_4$)), with experimental data adopted from refs [224] and [225].

Furthermore, the interlayer diffusion of the Li atoms was investigated by computing the barriers along the geometrically distinct paths between the cubine layers (Figure 7.3b). The lowest among all barriers was found for the transition between the symmetrically equivalent 1 and 1" sites with a value of merely 0.12 eV, which is even lower than the lowest barrier for the isolated cubine sheet. With all transition barriers at hand, a kinetic Monte Carlo simulation was carried out to estimate the lithium-ion diffusivity D. The values of D as a function of temperature are shown in Figure 7.3b(iii), calculated using a typical attempt frequency of $v = 10^{13}$ s^{-1}. We find a superior Li diffusivity of 3.8×10^{-5} cm^2/s at room temperature, more than 1 order of magnitude higher than state-of-the-art anodes (graphite, D = 10^{-6}~10^{-11} cm^2/s; $Li_4Ti_5O_{12}$ (LTO), D = 10^{-11}~10^{-12} cm^2/s) and cathodes ($LiCoO_2$ (LCO), D = 10^{-8}~10^{-10} cm^2/s; $LiMn_2O_4$ (LMO), D = 10^{-9}~10^{-11} cm^2/s).[57,58] This remarkable diffusivity renders CuBi a high-rate material that is capable of conducting Li faster than any known electrode material to date. Considering the high volumetric capacity together with the intriguing Li conductivity at relatively low cost, CuBi is a promising candidate to be used on its own in an anode for applications where space is limited, and a high charge/discharge rate is required in electrical energy storage, *e.g.*, in electric vehicles and for peak load regulations of smart power grids. On the other hand,

cubine with its large surface area and high number of active sites could be used as a component in composite anode and cathode materials (such as graphene) to improve their performance, *e.g.*, by increasing the rate capacity[226] and cyclability.[227]

7.4 Conclusion

In summary, we report on the discovery of a novel quasi 2D sheet, cubine. Since it is dynamically stable, cubine can readily serve as a building block for heterostructured 2D materials, and its large surface area offers potential active sites for adsorbates such as Li atoms. The low energy barriers between the A and B sites allows a high diffusion of Li on cubine. Furthermore, we demonstrate that the bulk CuBi can be readily intercalated with lithium with a high ion diffusivity, rendering it a promising candidate for energy storage applications.

CHAPTER 8

Kinetics and Reaction Mechanism during Electrochemistry of Sodium and Lithium with Selenium

8.1 Introduction

Selenium shows promising electrochemical performance as a cathode with both Li and Na, capable of room temperature cycling (up to 4.6 V) without failure.[228] Selenium has a much higher electrical conductivity (1×10^{-3} S m^{-1}) than that of sulfur (5×10^{-28} S m^{-1}), and its volumetric capacity is as high as sulfur cathode material.[228,229] Combining Se with carbon in particular will drastically improve the cycle performance and Columbic efficiency of selenium cathode due to the increasing electronic and ionic conductivity.[230]

However, different reaction pathways have been observed when the cells are run with different electrolytes. [229–231] A detailed mechanism of the alloying reactions with selenium in cycling remains unclear. It is especially unclear why the electrochemical properties of Se in sodium-ion batteries are as good as those in lithium-ion batteries. Here, both the reaction mechanism of selenium in sodium- and lithium-ion batteries, the reaction kinetics are investigated by DFT calculations with consideration of the crystalline structure, reaction thermodynamic energies, band gaps and ion diffusivities.

8.2 Methodology

The first principle density functional theory (DFT) calculations were conducted through the Vienna Ab-initio Simulation Package (VASP).[103–106] With the projector augmented wave (PAW) potentials,[107] generalized gradient approximation (GGA) of Perdew-Becke-Ernzerhof (PBE)[108] was used for exchange-correlation function under

spin polarization. A plane-wave basis set cutoff energy of 520 eV, and Γ-centered k-meshes with the density of 8000 k-points per reciprocal atom were used in all calculations.

To create a supercell of amorphous $Na_{0.5}Se$ suitable for DFT calculations, a cell containing 96 atoms was melted at 2900 K in ab initio molecular dynamics (Figure 8.1). The liquid state configuration was equilibrated over two picoseconds under an NVT ensemble,[232] followed by a rapid quench from the equilibration temperature to 300 K at rate of 1 K fs^{-1}. Then the atomic coordinates and cell parameters of the configuration were relaxed in DFT till the average forces fall below 10^{-2} eV $Å^{-1}$.[185]
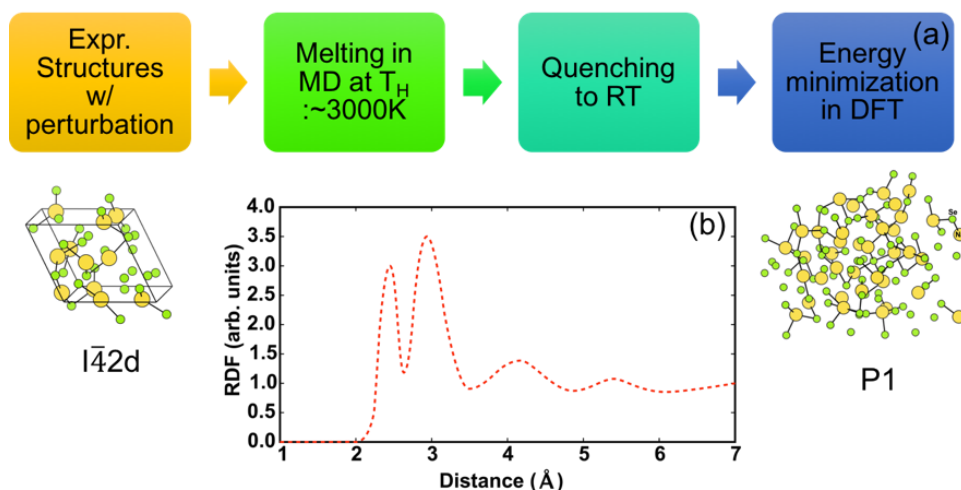
Figure 8.1 The generating and structure of amorphous $Na_{0.5}Se$ phase. (a) The proceeding process of amorphous $Na_{0.5}Se$ for the crystalline $NaSe_2$ phase. (b) Radius distribution function the amorphous phase $Na_{0.5}Se$.

In order to simulate the Na (Li) ion diffusions in selenium during the sodiation (lithiation), different first principle methods were applied to evaluate the ion transport through different kinetic mechanisms. For ion self diffusions by vacancies, kinetic Monte

Carlo Simulation was conducted based on transition-state theory as introduced in Section 2.2.3.

For ion diffusions through interstitial mechanisms, ab-initio molecular dynamics (MD) simulations were performed in VASP using supercells consisting of 96 (96, 81 and 81) atoms for $NaSe_2$ (Na_2Se_2, Na_2Se and Li_2Se). We simulated the canonical (NVT) ensemble through Nose thermostat with a minimal Γ-centered $1\times1\times1$ k-point grid.[233,234] In each run, Velocity-Verlet was used for time integration scheme with a step of 2 femtoseconds. Considering thermal expansion, we conducted a series of volume varying picosecond runs at each target temperature. Therefore, the volume of supercell was determined at where averaged pressure was approximately zero. When the MD simulations started, the Na (Li)-Se systems were assigned an initial temperature of 100 K and then it was heated up to target temperatures (600 K to 1800 K) in 2 picoseconds (ps) and equilibrated for 5 ps. We performed MD simulations to conduct the diffusion for 40 ps.

In addition, Na (Li) ion diffusivities at each target temperature were calculated by fitting the mean square displacement over time using the following equation: $D = \frac{1}{2t}\langle[r_c(t)]^2\rangle$. Here, $r(t)$ is the displacement of ions at time t, and D was obtained by a linear fitting to the dependence of average mean square displacement over $2t$.

8.3 Results and discussion

Ab Initio molecular dynamic (MD) simulations and kinetic Monte Carlo simulations with nudged elastic band (NEB) method implemented are applied to understand the underline mechanism of the electrochemical reaction of Se with Na and Li, and their reaction kinetics. Using the DFT energies of known compounds available in the

Open Quantum Materials Database[113,114]for the Na (Li)-Se system, the ground-state

phase diagrams are constructed shown as in Figure 8.2. The stable compounds in the binary

phase diagram refer to those which have lower energy than any linear combination of other

compounds. According to the DFT calculations, Li_2Se is the only ground-state phase in Li-

Se binary systems, while in Na-Se systems three phases $NaSe_2$, Na_2Se_2, and Na_2Se are

ground-state phases. This explains why three-step reaction mechanism has been observed

in the sodiation experiment, while only a single step reaction has been observed for

lithiation experiment. Accordingly in the calculated discharge profile, there is only one

plateau in the lithiation, while three plateaus appear upon sodiation as shown in Figure 8.3.

The calculated discharge profile matches also to the measured one,[228] except there is a

large overpotential for Na-ion battery, which could be due to cell resistance.
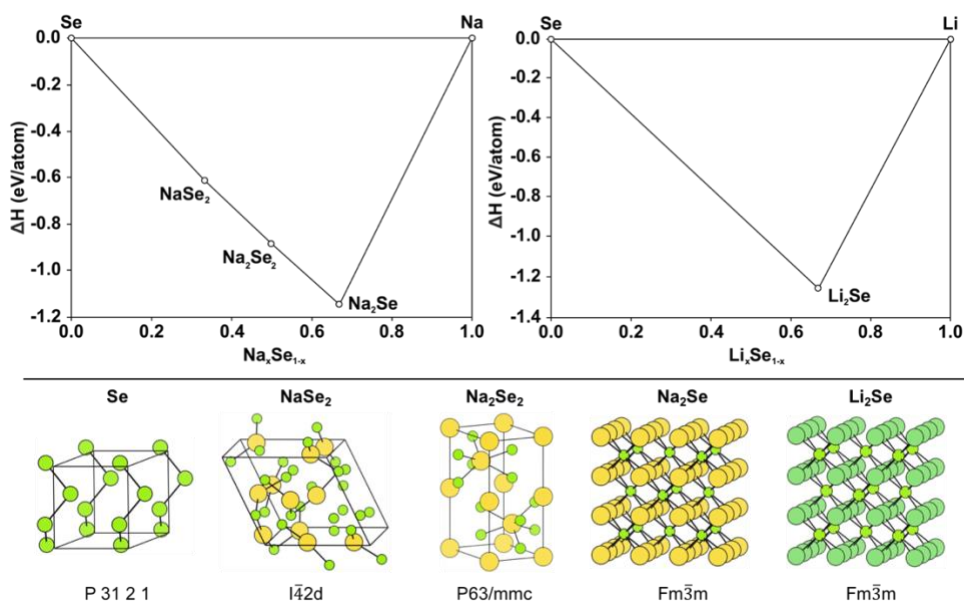
Figure 8.2 The phase diagram of Na-Se and Li-Se system and the unit cell of all the intermediate

phases in both sodiation and lithiation process.
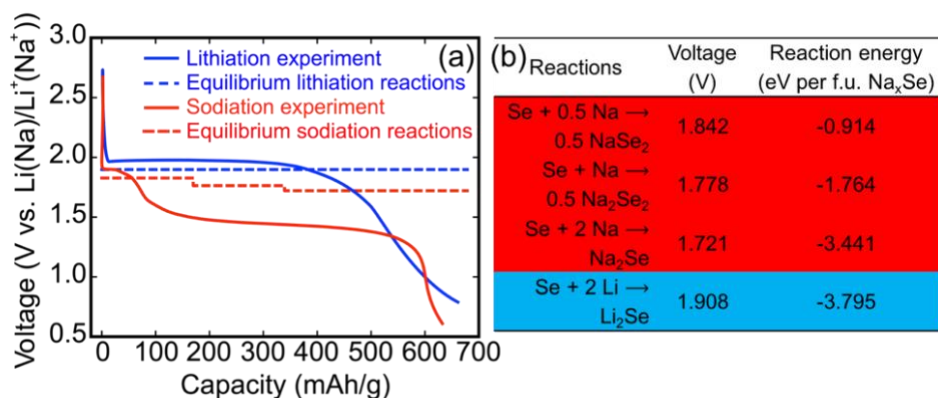
Figure 8.3 Thermodynamic driving force for sodiation and lithiation. (a) Calculated equilibrium lithiation/delithiation voltage profiles and experimental voltage profiles adopted from Ref. [228]. (b) The corresponding conversion reaction at different plateaus and the reaction energy.
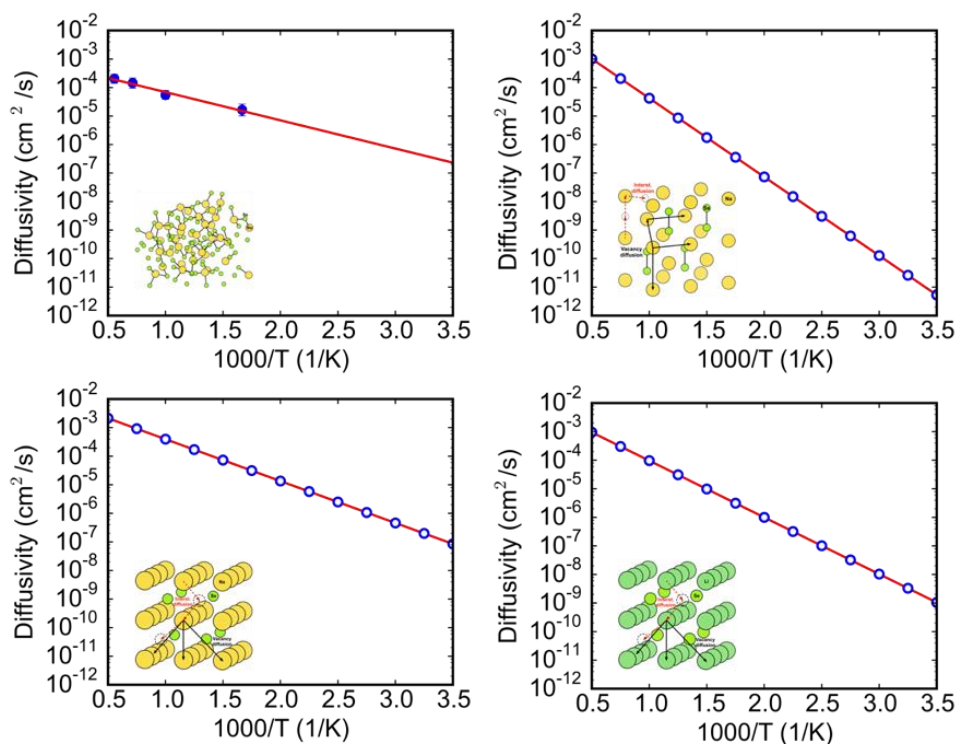
Figure 8.4. Arrhenius plot of the overall diffusion coefficient of the Na ion in the Na−Se phases and the Li ion in the Li2Se phase through a vacancy mechanism.

Table 8.1 The kinetics of Na-ion and Li-ion in product phases.

	$Na_{0.5}Se_{(Amorp.)}$	Na_2Se_2	Na_2Se	Li_2Se
Band gap (eV)	1.0	0.6	2.3	3.3
D (cm^2/s)	3.3×10^{-7}	4.7×10^{-11}	1.5×10^{-7}	2.2×10^{-7}

To further explore the kinetics of reactions with sodium and lithium, reaction thermodynamics, electronic and ionic diffusivities are calculated by DFT. As shown in Figure 8.3, the reaction energy between sodium and selenium (-3.441 eV) is slightly lower than that between lithium and selenium (-3.795 eV). This implies that although the diameter of sodium ion (1.04 Å) is much larger than that of lithium ion (0.76 Å), the chemical activity of sodium actually very close to that lithium. This suggests the difference in lithiation and sodiation speed should be mainly due to the kinetics of these reactions. The band gaps and ionic diffusivities in the Na-Se and Li-Se alloy phases have been calculated using first-principle calculations with the results being listed in the Table S1 and Figure 8.4. Band gaps of all the Na-Se intermediate phases are lower than that of the Li_2Se suggesting that electrical conductivities of all the Na-Se intermediate phases are much better than that of the Li-Se phases. Meanwhile, the ionic diffusivity of sodium ions in all Na-Se alloying phases has also been calculated and the results shown in Figure 8.4. The ionic conductivity of the amorphous $Na_{0.5}Se$ phase (3.3×10^{-7} cm^2 s^{-1}) for Na-ions is almost two orders higher than that of Li_2Se phase (2.2×10^{-9} cm^2 s^{-1}) for Li-ions. Therefore, the higher kinetics in sodiation reaction is caused by the better electric conductivity and higher Na$^+$ mobility in the Na-Se alloying phases, compared to that of Li_2Se phase. The sodiation initialized with solid-state amorphization process with formation of amorphous $Na_{0.5}Se$ phase, and the amorphous phase is gradually reduced to polycrystalline Na_2Se_2 and Na_2Se crystalline phases. It is intriguing that selenium is reduced to an amorphous sodium

polyselenide $Na_{0.5}Se$ phase, instead of forming the crystalline $NaSe_2$ phase. This could be due to fast insertion of sodium ions, leaving no time for the amorphous phase to relax to its ground-state phase.

8.4 Conclusion

In summary, we investigate the reaction mechanism and kinetics of lithium/sodium with selenium, as a promising cathode material in both sodium and lithium ion batteries. Selenium is reduced to the polyselenides, *e.g.* amorphous $Na_{0.5}Se$, polycrystsalline Na_2Se_2 and Na_2Se sequentially in sodiation. In lithiation, Se is directly reduced into Li_2Se phase. Kinetics of the electrochemical reaction of Na/Se and Li/Se has been systematically investigated. DFT calculation shows that the Na-Se compounds appeared in sodiation have narrow band gaps, thus high electronic conductivity and fast diffusion channels for sodium ions. Our finding shows that selenium is a promising high rate capability cathodic material for sodium ion batteries. It provides also the new insights to understand the sodiation and lithiation kinetics, which is helpful to design new type sodium ion batteries in the future.

CHAPTER 9

Stability and conductivity of cation and anion substituted LiBH$_4$ based solid-state electrolyte

9.1 Introduction

Lithium borohydride, LiBH$_4$, shows a great potential for next-generation LIBs with the following advantageous features[235]: *i*) fast lithium ion conductivity, *ii*) low grain boundary resistance, *iii*) negligible electronic conductivity, *iv*) high electrochemical stability (up to ~5 V *vs*. Li/Li$^+$), and *iv*) high chemical stability against the decomposition in contact with a lithium metal and/or graphite-based anode materials. Previously, LiBH$_4$ has been mostly studied as a candidate material to be used in hydrogen storage applications.[236–238]

The low-temperature (LT) phase of LiBH$_4$ (denoted as LT-LiBH$_4$ in this work) has an orthorhombic *Pnma* structure; and it undergoes a structural phase transition to become a hexagonal *P6$_3$mc* phase above ~390 K. The high-temperature (HT) phase of LiBH$_4$ (denoted as HT-LiBH$_4$ in this work) exhibits a high ionic conductivity on the order of 10^{-3} S/cm,[239] and the HT-LiBH$_4$ behave as an electrical insulator with a large band gap of ~6 eV[240], which make it highly promising to be utilized as a SSE in LIBs. Previous studies have also reported that incorporation of lithium halides (LiX, where X = Cl, Br, and I) into LiBH$_4$ structure can form a solid solution (*i.e.*, xLiX·(1-x)LiBH$_4$) in a wide range of concentration, which can further lower the phase transition temperature of LT-LiBH$_4$ to HT-LiBH$_4$ (*i.e.*, we will refer this as the "stabilization" of HT-LiBH$_4$ in this work).[56,241–245] The substitution of LiI into LiBH$_4$ structure enables not only stabilizing effect, but

also achieves a very high lithium ion conductivity.[56,246,247] Previous study has demonstrated that lithium ions can be transported in a two-dimensional channel in xLiX·(1-x)LiBH$_4$, and the Frenkel defects can be formed favorably and stays mobile (*i.e.*, low defect formation energy and small migration barrier).[248] Another effective strategy reported to date that lowers the phase transition temperature of LiBH$_4$ is to substitute Li with other alkali elements such as Na and K.[249]·[250]

In this work, we report the stabilization effects (*i.e.*, reducing the energy difference between the LT- and HT-LiBH$_4$) by the elemental substitutions using standard DFT calculations; namely, the alkali metals Na and K as cation substitutions on the Li site, and the halogens F, Cl, Br, and I as anion substitutions on BH$_4$ site. Additionally, we have determined the defect concentrations and lithium ion conductivities using native defect formation energy calculation, with the combination of the Nudged elastic band (NEB) and Kinetic Monte Carlo (KMC) simulations for the targeted systems. Lastly, we have analyzed the relations between the ionic conductivity and stabilization effects that are highly dependent on both substituents and their concentrations in LiBH$_4$-based lithium ion conducting materials. Based on our first-principles investigations, we suggest that the maximum stabilization and lithium ionic conductivities of the specific system can be accomplished by carefully tuning the concentrations of cation/anion substituents.

9.2 Methodology

All total energies were obtained from density functional theory (DFT) calculations using the Vienna *ab initio* simulation package (VASP).[106] We used the PW91[251] generalized gradient approximation (GGA) to the exchange-correlation energy with the

projector augmented wave (PAW)[107] method and a plane wave cutoff energy of 875 eV. Since the detailed substituted structures for LiBH$_4$ are unknown, we initiated with supercell of HT *P6$_3$mc* and LT *Pnma* phase structures of LiBH$_4$ containing 16 formula units (96 atoms). For the cation/anion substituted LiBH$_4$, we used ENUM[127] to generate all derivative configurations with various compositions and substituent concentrations. After relaxation of all these structures within VASP, we chose the structure with the lowest DFT energy for the further analysis. Defects were introduced in supercells of HT-LiBH$_4$, Li(BH$_4$)$_{1-x}$I$_x$, ($x = 0.25$ and 0.5), and Li$_{1-y}$K$_y$BH$_4$ ($y = 0.25$) that contained 96, 80, and 96 atoms after a series of convergence tests, respectively. For all these calculations, we used Γ-centered k-meshes with the density of 8000 k-points per reciprocal atom. The atomic coordinates were relaxed until the total energy converged within 10^{-5} eV and the interatomic forces were below 10^{-2} eV/Å. Defect conductivity calculations were conducted using method described in Section 2.2.

9.3 Results and discussion

9.3.1 Stabilization of HT-LiBH$_4$ by halogen (F, Cl, Br, I) and alkali metal (Na, K) substitution

To evaluate the stabilization effects of various substitutions including halogen (F, Cl, Br, and I) and alkali (Na, K) elements, we have calculated the DFT energy differences (ΔE) between the HT- and LT-LiBH$_4$ phases: $\Delta E = E_{HT} - E_{LT}$, where E_{HT} and E_{LT} are the energy of partially-substituted HT- and LT-LiBH$_4$ structures. Considering that the stabilization effects can further depend on the substituent concentration, we repeat the

calculation for a series of concentrations: $x, y = 0.125, 0.25, 0.50$ in xLiX·$(1-x)$LiBH$_4$ and yABH$_4$·$(1-y)$LiBH$_4$.

Both the anion (F, Cl, Br, and I) and cation (Na, K) substitutions decrease the energy difference between the substituted HT- and LT-LiBH$_4$ phases, as displayed in Figure 9.1a. It can be also observed in Figure 9.1a that a higher substituent concentration further lowers the DFT energy difference between the substituted HT- and LT-LiBH$_4$ phase (*i.e.*, enhanced stabilization effects). However, there are no clear tendencies in Figure 9.1a among different substitution elements at the same specific concentration.

In Figure 9.1b, we have computed the DFT volumes (per formula unit) of cation/anion substituted HT-LiBH$_4$ structures. We find that K$^+$ and I$^-$ ions that have a larger effective radius (see Table 9.1) directly contribute to the enlargement of the cell volumes upon the substitutions in LiBH$_4$ structure, while the substitutions of ions with a smaller ionic radius (*e.g.*, Br$^-$ and Cl$^-$) only have a limited impact on the final cell volume. From the variations among the predicted cell volumes provided in Figure 9.1b, we therefore conclude that the stabilization effects cannot be solely explained by the size differences of the substituents.[247]

In Figure 9.1c, we show the calculated mixing energy between HT-LiBH$_4$, ABH$_4$ (A = Na and K) or LiX (X = F, Cl, Br and I). We find in Figure 9.1c that the moderate-sized substituents (*e.g.*, Br$^-$, I$^-$ and Na$^+$) lead to a lower mixing energy, compared with the substituents with large ionic radii (*e.g.*, K$^+$, I$^-$) or small ionic radii (*e.g.*, F$^-$) in HT-LiBH$_4$. All mixing energies calculated in Figure 9.1c are negative (except F$^-$), which explains the favorable solid solution formation between HT-LiBH$_4$ and LiX (X = Cl, Br, I)[244] or ABH$_4$ (A = Na, K)[249] with the wide range of substituent concentrations. For further Li$^+$

ion kinetic studies, we chose I- and K-substituted $LiBH_4$ structures to investigate the effects of halogen and alkali metal substitutions on the transport properties. Previous literature suggests that the Li^+ ion conduction is highly dependent on the concentration of substituents in $LiBH_4$,[58] therefore, we simulate two different structures with varying concentrations, namely, $Li(BH_4)_{0.75}I_{0.25}$ and $Li(BH_4)_{0.5}I_{0.5}$ compounds. To compare to the I substitution, we further studied K substitution, as in $Li_{0.75}K_{0.25}BH_4$.

Table 9.1 Effective radii of substituting halogen/alkali ions and B-H bond length

Ion	Li^+	Na^+	K^+	F^-	Cl^-	Br^-	I^-	B-H
Radius (Å)[252]	0.90	1.13	1.51	1.33	1.67	1.82	2.06	1.29 (HT)
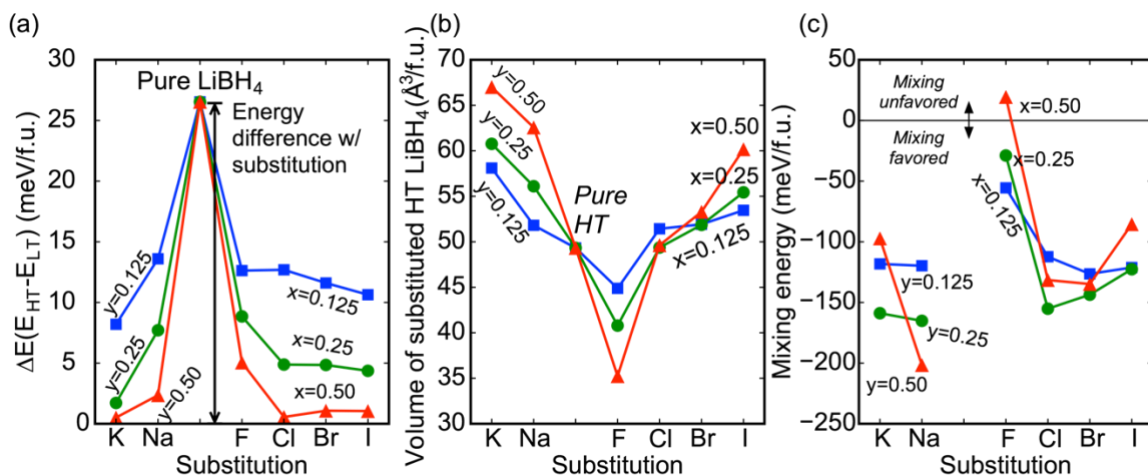
Figure 9.1 (a) DFT energy differences between HT- and LT-$LiBH_4$ phases with/without cation/anion substituents. We have tested three different substituent concentrations in each system. (b) Evolution of the DFT volume (per formula unit) in $(1-x)LiBH_4+xLiX$ and $(1-y)ABH_4+yLiBH_4$ as a function of substituents and their concentrations. (c) DFT mixing energy between HT-$LiBH_4$ and LiX or ABH_4.

9.3.2 Native defect concentrations in HT-LiBH$_4$, Li(BH$_4$)$_{1-x}$I$_x$, (x = 0.25, 0.5) and Li$_{1-y}$K$_y$BH$_4$ (y = 0.25)

To study the point defects in HT-LiBH$_4$ and selected systems of Li(BH$_4$)$_{0.75}$X$_{0.25}$, Li(BH$_4$)$_{0.5}$X$_{0.5}$, and Li$_{0.75}$K$_{0.25}$BH$_4$, we consider following interstitials with the specified charged states: Li with q = +1, 0, -1; H with q = +1, 0, -1; H$_2$ with q = 0; and K with q = +1, 0, -1. We also examine vacancy Li with q = +1, 0, -1; H with q = +1, 0, -1; B with q = +3, +2, +1, 0, -1, -2, -3; BH$_x$ (x = 1, 2, 3, 4) with q = +1, 0, -1; I with q = +1, 0, -1; and K with q = +1, 0, -1. Additionally, Li Frenkel defect is also examined. For all these defect types, we evaluate the defect formation energies considering different number of geometrical configurations (Table S1).

Here, we only show the formation energies of Li related defects (Figure 9.2). For HT-LiBH$_4$, both Li Frenkel defect and Li defect pair (Li$_{Int}^+$, Li$_{vac}^-$) have negative formation energies: -1.3 eV, -0.9 eV (0.92 eV, 0.53eV for LT-LiBH$_4$), which are expected, as HT-LiBH$_4$ phase is unstable at room temperature.[253,254] For I- and K-substituted cases, Li related formation energies are always positive, confirming the stabilization effects. Dominant Li defect types with the lowest formation energy for Li(BH$_4$)$_{0.75}$I$_{0.25}$, Li(BH$_4$)$_{0.5}$I$_{0.5}$ and Li$_{0.75}$K$_{0.25}$BH$_4$ are defect pair (0.05 eV), Frenkel defect (0.15 eV), and defect pair (0.44 eV), respectively. It is noteworthy that Frenkel defect is more favorable in Li(BH$_4$)$_{0.5}$I$_{0.5}$ compared with the individual Li interstitial and vacancy formations. With increasing I$^-$ concentration (from x = 0.25 to 0.50), the dominant defect formation energy goes up from 0.05 eV to 0.15 eV, while the energy difference (ΔE) decreases from 48 meV/$f.u.$ to 11 meV/$f.u.$ We therefore conclude in Figure 9.2 that enhanced stabilization

can significantly increase the defect formation energies; however, this is not desired at all, as it can decrease the total defect concentration in the system.
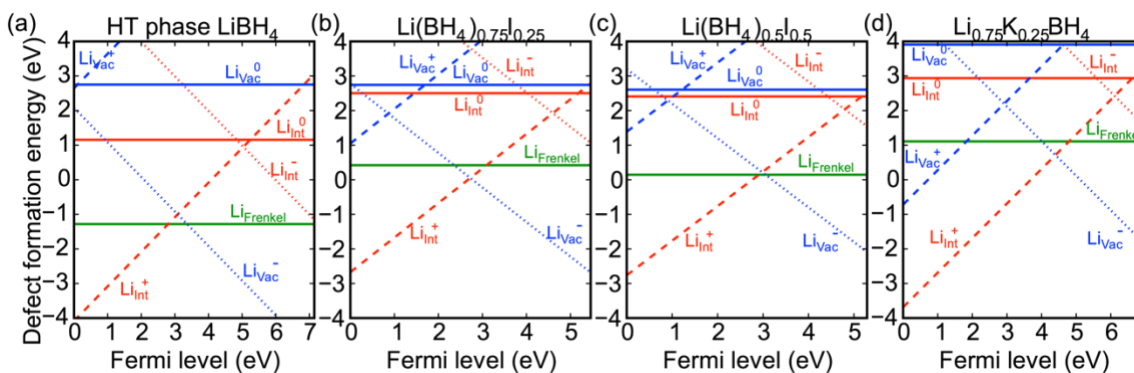
Figure 9.2 Calculated formation energies of lithium-related defects in (a) HT-LiBH$_4$, (b) Li(BH$_4$)$_{0.75}$I$_{0.25}$, (c) Li(BH$_4$)$_{0.5}$I$_{0.5}$, and (d) Li$_{0.75}$K$_{0.25}$BH$_4$, plotted as a function of Fermi energy with respect to the valence-band maximum.

The calculated temperature-dependent native defect concentrations in Li(BH$_4$)$_{0.75}$I$_{0.25}$, Li(BH$_4$)$_{0.5}$I$_{0.5}$, and Li$_{0.75}$K$_{0.25}$BH$_4$ are shown in Figure 9.3. It is numerically not feasible to carry out the defect concentration calculations in HT-LiBH$_4$ due to its negative defect formation energy. As we mentioned above, the defect formation energy elevations caused by the structural stabilizations with cation/anion substitutions decrease the room temperature Li related defect concentrations. The concentrations of dominant defects at room temperature for these three cases (Li(BH$_4$)$_{0.75}$I$_{0.25}$, Li(BH$_4$)$_{0.5}$I$_{0.5}$, and Li$_{0.75}$K$_{0.25}$BH$_4$) are found to be 10^{-1} #/$f.u.$, 10^{-3} #/$f.u.$, and 10^{-10} #/$f.u.$, as displayed in Figure 9.3.
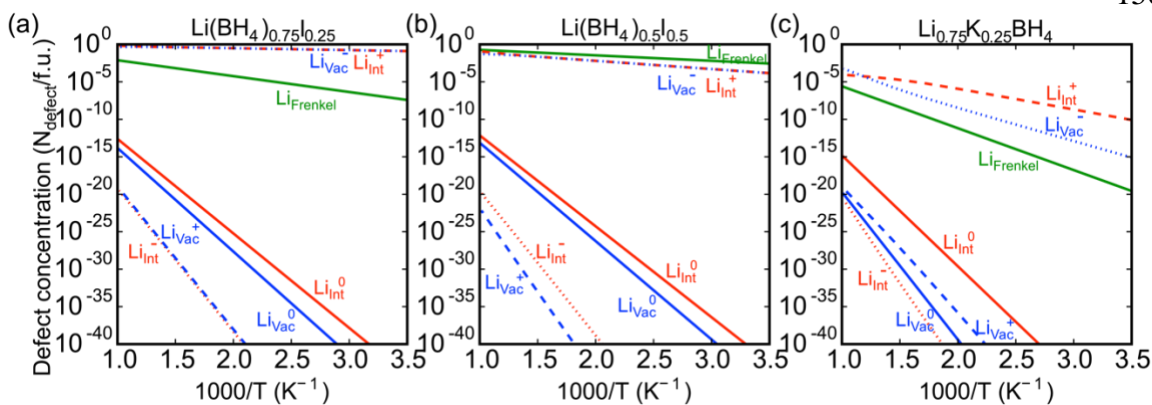
Figure 9.3 Lithium related defect concentrations in (a) $Li(BH_4)_{0.75}I_{0.25}$ (b) $Li(BH_4)_{0.5}I_{0.5}$, and (c) $Li_{0.75}K_{0.25}BH_4$ plotted as a function of temperature. The highest defect concentrations at room temperature for these three cases are found to be 10^{-1} #/f.u., 10^{-3} #/f.u. and 10^{-10} #/f.u., respectively.

9.3.3 Lithium ion mass transport in $Li(BH_4)_{1-x}I_x$ ($x = 0.25, 0.5$) and $Li_{1-y}K_yBH_4$ ($y = 0.25$)

In this section, we present the lithium ion conductivities calculated for $Li(BH_4)_{0.75}I_{0.25}$, $Li(BH_4)_{0.5}I_{0.5}$, and $Li_{0.75}K_{0.25}BH_4$ system with the combinations of nudged elastic band (NEB) method and Kinetic Monte Carlo simulations. Spatial lithium ion diffusion networks of both interstitial and vacancy were built for all these cases based on all the interstitial and vacancy sites, as demonstrated in Figure 9.4. Different number of diffusion pathways was considered for interstitials and vacancies, and the subsequent energy barriers are examined for all these pathways.
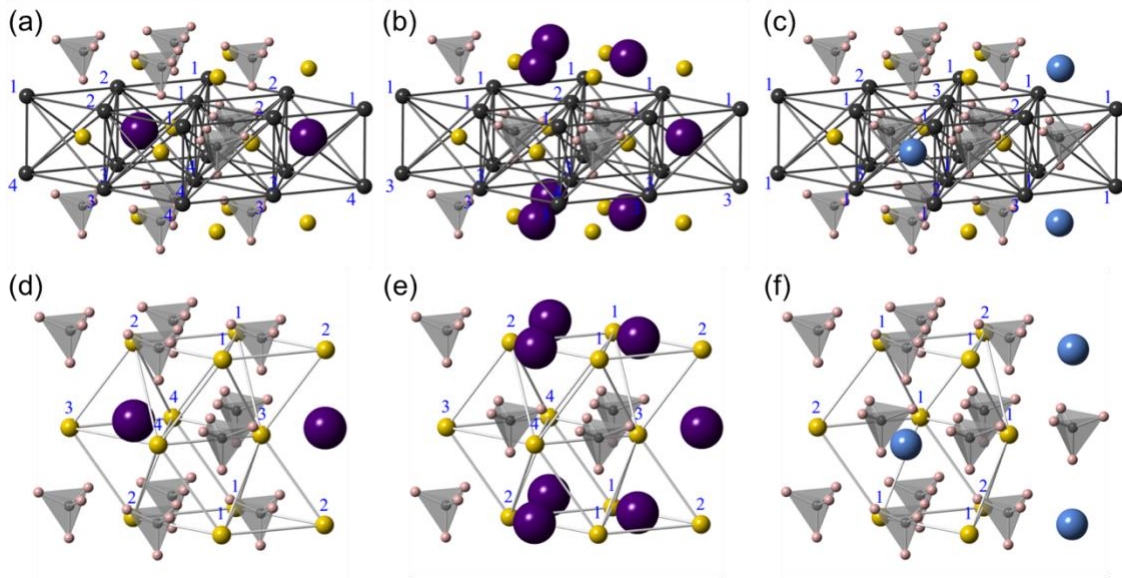
Figure 9.4 Lithium ion defect diffusion network: interstitial paths in (a) $Li(BH_4)_{0.75}I_{0.25}$, (b) $Li(BH_4)_{0.5}I_{0.5}$, and (c) $Li_{0.75}K_{0.25}BH_4$; vacancy paths in (d) $Li(BH_4)_{0.75}I_{0.25}$, (e) $Li(BH_4)_{0.5}I_{0.5}$, and (f) $Li_{0.75}K_{0.25}BH_4$. Black (silver) lines represent the interstitial (vacancy) lithium ion diffusion paths between different defects sites (the numbers shown in blue-colored font). The gold, black, blue, dark grey, light grey, and violet circles represent Li (and vacancy site), Li interstitial site, K, B, H, and I, respectively.

We report the lowest barriers of 0.14 eV/0.25 eV for interstitial and vacancy diffusion, respectively, in $Li(BH_4)_{0.75}I_{0.25}$, which is consistent with previous work[248]. In the system of $Li(BH_4)_{0.5}I_{0.5}$, very similar preferred paths are identified for both interstitial and vacancy diffusions with the lowest barriers of 0.20 eV/0.18 eV, respectively. In $Li_{0.75}K_{0.25}BH_4$, both interstitial and vacancy diffusions found to be very difficult, with the lowest barriers of 0.56 eV/0.59 eV, respectively. The KMC simulations are also carried at a series of temperatures for each kind of defect using the all energy barriers obtained. The diffusivity pre-factor D_0 and Q were fitted and all the diffusivity profiles *vs.* temperature are provided in Figure 9.5a.
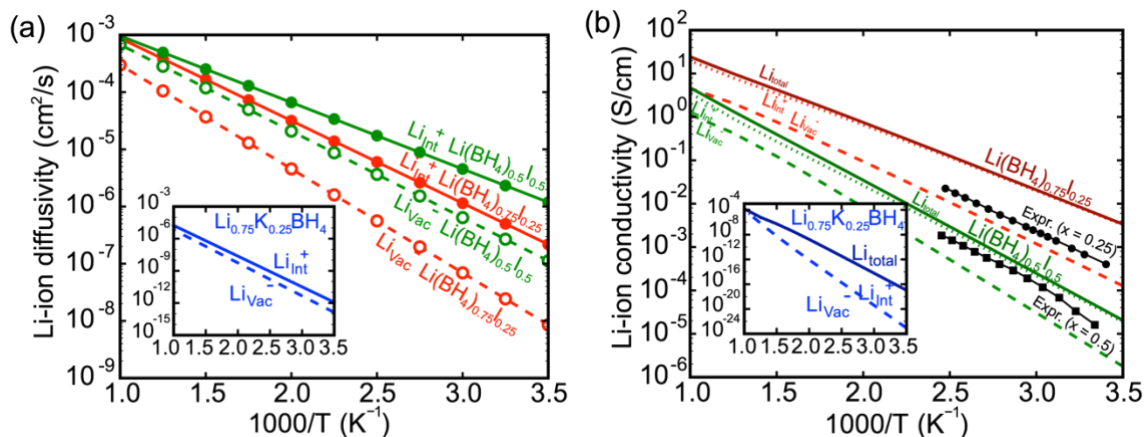
Figure 9.5 (a) Calculated lithium ion defect diffusivities of $Li(BH_4)_{0.75}I_{0.25}$, $Li(BH_4)_{0.5}I_{0.5}$, and $Li_{0.75}K_{0.25}BH_4$ as a function of temperature. (b) Calculated lithium ion defect conductivities of $Li(BH_4)_{0.75}I_{0.25}$, $Li(BH_4)_{0.5}I_{0.5}$, and $Li_{0.75}K_{0.25}BH_4$ as a function of temperature (attempt frequency: $\nu = 10^{13}$). The experimental conductivity profiles are adopted from *Refs. (11)* and *(34)*.

At room temperature, the lithium ion diffusivities in $Li(BH_4)_{0.75}I_{0.25}$ are found to be 10^{-7} cm^2/s (interstitial mechanism) and 10^{-8} cm^2/s (vacancy mechanism). Lithium ion diffusivities in $Li(BH_4)_{0.5}I_{0.5}$ are found to be ~10^{-6} cm^2/s (for interstitial) and 10^{-7} cm^2/s (vacancy), due to a relatively longer defect diffusion distance. For $Li_{0.75}K_{0.25}BH_4$, the lithium ion diffusion at room temperature is not fast enough for SSE applications, with a calculated diffusivity of 10^{-12} cm^2/s. Overall, interstitial diffusion is preferred in all systems, which can be explained by the volume expansion caused by I- or K-substitutions in $LiBH_4$.

In addition, the conductivities in Figure 9.5 were calculated, combined with the defect diffusivities and concentrations obtained above (*i.e.*, by adding interstitial and vacancy conductivities together). The computed conductivity profiles of $Li(BH_4)_{1-x}I_x$ ($x = 0.25$, 0.5) in Figure 9.5b demonstrate a reasonable comparison with the experimental observations. The

overestimate is expected, as we performed simulations within a perfect crystal structure (*i.e.*, without any impurities and grain boundaries) that can further lead to a decreased experimental Li^+ ion conductivity.[224] We find that the conductivity profile of $Li(BH_4)_{0.75}I_{0.25}$ is much higher than $Li(BH_4)_{0.5}I_{0.5}$ counterpart with a larger room temperature conductivity of 5.7×10^{-3} S/cm (compared with 4.2×10^{-5} S/cm for $Li(BH_4)_{0.5}I_{0.5}$). It is noteworthy that the diffusivity profiles show a trend opposite to conductivity, with an easier lithium ion migration in $Li(BH_4)_{0.5}I_{0.5}$ system in Figure 5a. Higher lithium ion conductivity in $Li(BH_4)_{0.75}I_{0.25}$ can be attributed to its higher defect concentration, as a result of lower defect formation energies and decreased stabilization effects. Therefore, the experimentally-observed fluctuations in the conductivity profile *vs.* concentration[58,247,255] of $Li(BH_4)_{1-x}I_x$ systems can be explained by the competing effects between the defect concentration and Li^+ ion mobility caused by the substitutional effects. We conclude that the stabilization of HT-LiBH$_4$ should be carefully tuned in order to permit the formation of sufficient amount of defects that can facilitate a fast lithium ion conduction. Lithium ion conductivity in $Li_{0.75}K_{0.25}BH_4$ is found to be extremely low, which can be further explained by the blocked lithium ion diffusion pathway and a narrow diffusion channel due to the K-substitutions in LiBH$_4$.

9.4 Conclusion

In this work, we have shown that various cation/anion substitutional effects in HT-LiBH$_4$ (*i.e.*, halogen substation of F, Cl, Br, and I in BH$_4$ site; and alkali metal substitution of Na and K in Li site) decreases the ground state energy gap between less stable HT- and more stable LT-phase. We find that it is most effective to substitute I^- for BH$_4$ or K^+ for Li^+ to achieve the stabilization of the HT phase at the equal substituent concentration. A positive relation between

the substitution concentration and energetic stabilization of the HT phase was found. The moderately-sized ions (Br^-, I^-, and Na^+) led to a lower mixing energy compared with the substituents with larger ionic radii (*e.g.*, K^+, I^-) or smaller ionic radii (*e.g.*, F^-). The calculated mixing energies of HT-$LiBH_4$ and LiX or ABH_4 are found to be negative (except F^-), which explains the experimentally-observed solid solution formation in a wide range of substituent concentrations. The stabilization of HT-$LiBH_4$ increases the defect formation energy, leading to a lower defect concentration. In $Li(BH_4)_{1-x}I_x$, we find that higher concentration of I^- yielded a higher diffusivity; however, with a lower conductivity. The non-monotonic relation between concentration and conductivity could be a result of competing effects between the diffusivity and defect concentration. The lithium ion conductivity obtained by K-substitution in Li site is found to be very low, because of the blocking of lithium ion diffusion pathway by K ion and the narrow diffusion channel. We emphasize that the stabilization of $LiBH_4$-based lithium ion conductor can be optimized experimentally by careful selection of cation/anion substituents and their concentrations, which can further realize the highest lithium ion conduction in $LiBH_4$.

CHAPTER 10

Conclusions and future work

10.1 Summary

Density functional theory (DFT) based first-principles calculations have been widely used as efficient tools to accelerate the lithium ion battery designing through predicting new electrode materials, as well as to improving the existing materials by accurately revealing detailed underlying mechanisms that are often difficult to obtain solely *via* experiments. In this dissertation, we present our work on the development of next-generation high energy density, low cost and fast rate lithium ion batteries.

In Chapter 3, we use the first-principles calculations to understand the electrochemical charge and discharge of the conversion reaction electrodes *via* exploring the equilibrium and non-equilibrium thermodynamics with a mechanistic method as designed. We provide detailed information for the origin of large voltage hysteresis and volume expansion which have been hindering the practical application of conversion reaction materials and offer tips on alleviating them through reasonably operation range restrictions.

In Chapter 4, we continue our research on applying the Non-Equilibrium Phase Searching method as designed to other transition metal oxides/sulfides in order to obtain a more general understanding of the detailed mechanism for conversion materials during charging and discharging. Together with experimental efforts, we attempt to reveal the conversion mechanisms of additional transition metal oxides and sulfides such as $(Cu,Co)_3O_4$, CuS, and MoS_2.

In Chapter 5 and 6, we demonstrate how the coordination structure and bonding environment enable the reversible oxygen redox in the 3d metal oxides. The specific redox active Li_6-O local Li-excess configuration as identified for the iron oxide electrode enriches the anionic redox battery chemistry with a low-cost high energy density battery designed. For the manganese oxide anionic redox active electrodes, we predict novel materials with improved properties compared to the original system through high-throughput DFT screening.

In Chapter 7, using kinetics calculations we discover a novel 2-dimensional material with superior electric and ionic conductivity compared to traditional 2-dimensional nano sheet like graphene which can be used to boost the rate capacity of state-of-the-art LIBs.

In Chapter 8, we accurately reveal the mechanism of the kinetics-dominated electrochemical sodiation and lithiation reactions of selenium.

In Chapter 9, we clarify the relationship between the stability and ionic conductivity of the complex borohydride based lithium ion conductor and giving guidance on its further investigations.

As one of the most active research field, a large number of research directions are undergoing focusing on different aspects of this electrochemical device. All the battery related research topics as described in this dissertation are far from mature and completion and further investigations are necessary to clarify all the undefined issues. In the following section, we will briefly go through several most promising future research directions.

10.2 Future work

10.2.1 Explore the non-equilibrium thermodynamics in electrochemical conversion reactions

We succeeded to reveal the conversion mechanisms of transition metal oxides and sulfides such as Co_3O_4, $(Cu,Co)_3O_4$, NiO, MoS_2, and CuS by the nonequilibrium intermediate phase search method as developed. Based on what we have learned from these systems, we plan to continue our research on the conversion type electrodes and apply our method to other conversion material systems in order to obtain a more general understanding of the detailed mechanism for conversion materials during charging and discharging. Our study could help future experiments to overcome the current limitations of the conversion-type electrode materials and promote the development of more advanced LIBs.

10.2.2 Discovery of high energy density anionic redox active iron oxide electrodes

The pursuit of breaking the capacity limits has recently turns the research focus to the anionic redox because of a remarkably enhanced capacity can be achieved without breaking the basic structure of conventional lithium ion battery (no O_2 releasing). As discussed in Chapter 5, currently the capacity is limited to be 192 mAh/g with the reaction proceeds between two disordered rocksalt phases as follows with $x = 0$:

$$Li_{3-x}Fe^{3+/4+}O_{3.5}^{2-/1-} + (1+x)\, Li + 1\, e^- \leftrightarrow Li_4Fe^{3+}O_{3.5}^{2-} \tag{10.1}$$
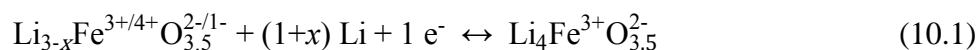
One of the way to improve its capacity is to push x to be larger than 0. In light of the complexity of the nature of solid solution reactions, the accurately prediction of the largest size of x requires a comprehensive understanding of the relationship between rocksalt structural

disordering, valence and anionic redox activity. The most straightforward approach would be generating a series of structures with different x and monitor the structure status, and Fe/O valence evolution. The purpose of checking structure status is to avoid possible structure collapse on delithiation and keep the redox centers: Li_6-O configurations nearly intact, as well as potential Fe migration which would cause extra kinetics burden to the system on cycling. Meanwhile, the O valence should be monitored to detect the possible formation of O^0 or O_2. Once we have a thorough understanding of this specific relationship and able to predict the detailed value of x, we will be aware of the capacity maximum of this super lithium rich iron oxide electrode. At the same time, the findings will shed light on the search of non-iron oxide based anionic redox active electrode materials.

10.2.3 High-throughput DFT screening for Cubine based fast rate electrodes

The success in building large database storing quantum properties of materials enabled the high-throughput DFT study. The Open Quantum Materials Database (OQMD) as developed at Northwestern University is an open access web database containing >450,000 inorganic materials adopted from the Inorganic Crystal Structure Database (ICSD) and hypothetical prototypes. As discussed in Chapter 7, cubine exhibits superior electric and ionic conductivities compared to all well-known conventional electrodes. However, considering the heavy atom mass of Bi and Cu, the gravimetric capacity of cubine is relative low. The idea is to find the structural analogs of cubine which are composed by lighter atoms. Our high-throughput screening strategy contains four steps as follows:

1. Start with the cubine structure and replace Bi/Cu with other Pnictogen elements/3d metal elements (PM) to build cubine analogue structures.

2. Perform DFT calculations to obtain the total energies of all these structures before (PM) and after full lithiation (LiPM) and then evaluate their stability using OQMD.

3. Pick the systems with negative or less positive formation energies (< 25 meV/atom) and geometrically well-maintained structures for both PM and LiPM.

4. Rank the selected systems with their electric and ionic conductivity.

Through this screening, we would be able to find cubine analogs with comparable kinetics yet much higher capacities.

Reference

[1]   A. Yoshino, K. Sanechika, T. Nakajima, Secondary battery, 4668595, 1987.

[2]   M.S. Whittingham, Lithium Batteries and Cathode Materials, Chem. Rev. 104 (2004) 4271–4302. doi:10.1021/cr020731c.

[3]   Y. Wang, G. Cao, Developments in Nanostructured Cathode Materials for High-Performance Lithium-Ion Batteries, Adv. Mater. 20 (2008) 2251–2269. doi:10.1002/adma.200702242.

[4]   K. Mizushima, P.C. Jones, P.J. Wiseman, J.B. Goodenough, LixCoO2 (0<x<1):A new cathode material for batteries of high energy density, Mater. Res. Bull. 15 (1980) 783–789. doi:10.1016/0025-5408(80)90012-4.

[5]   P. Albertus, J. Christensen, J. Newman, Experiments on and Modeling of Positive Electrodes with Multiple Active Materials for Lithium-Ion Batteries, J. Electrochem. Soc. 156 (2009) A606–A618. doi:10.1149/1.3129656.

[6]   R.J. Gummow, A. de Kock, M.M. Thackeray, Improved capacity retention in rechargeable 4 V lithium/lithium-manganese oxide (spinel) cells, Solid State Ionics. 69 (1994) 59–67. doi:10.1016/0167-2738(94)90450-2.

[7]   A.K. Padhi, K.S. Nanjundaswamy, J.B. Goodenough, Phospho-olivines as Positive-Electrode Materials for Rechargeable Lithium Batteries, J. Electrochem. Soc. 144 (1997) 1188–1194. doi:10.1149/1.1837571.

[8]   R. Malini, U. Uma, T. Sheela, M. Ganesan, N.G. Renganathan, Conversion reactions: a new pathway to realise energy in lithium-ion battery—review, Ionics (Kiel). 15 (2009) 301–307. doi:10.1007/s11581-008-0236-x.

[9]   J. Cabana, L. Monconduit, D. Larcher, M.R. Palacín, Beyond Intercalation-Based Li-Ion

        Batteries: The State of the Art and Challenges of Electrode Materials Reacting Through

        Conversion Reactions, Adv. Mater. 22 (2010) E170–E192. doi:10.1002/adma.201000717.

[10]   M. Sathiya, G. Rousse, K. Ramesha, C.P. Laisa, H. Vezin, M.T. Sougrati, M.-L. Doublet,

        D. Foix, D. Gonbeau, W. Walker, A.S. Prakash, M. Ben Hassine, L. Dupont, J.-M.

        Tarascon, Reversible anionic redox chemistry in high-capacity layered-oxide electrodes,

        Nat. Mater. 12 (2013) 827–835. doi:10.1038/nmat3699.

[11]   E. McCalla, A.M. Abakumov, M. Saubanère, D. Foix, E.J. Berg, G. Rousse, M.-L.

        Doublet, D. Gonbeau, P. Novák, G. Van Tendeloo, R. Dominko, J.-M. Tarascon,

        Visualization of O-O peroxo-like Dimers in High-capacity Layered Oxides for Li-ion

        Batteries., Science (80-.). 350 (2015) 1516–1521. doi:10.1126/science.aac8260.

[12]   E. McCalla, M.T. Sougrati, G. Rousse, E.J. Berg, A. Abakumov, N. Recham, K. Ramesha,

        M. Sathiya, R. Dominko, G. Van Tendeloo, P. Novák, J.-M. Tarascon, Understanding the

        Roles of Anionic Redox and Oxygen Release during Electrochemical Cycling of Lithium-

        Rich Layered Li4FeSbO6, J. Am. Chem. Soc. 137 (2015) 4804–4814.

        doi:10.1021/jacs.5b01424.

[13]   K. Luo, M.R. Roberts, R. Hao, N. Guerrini, D.M. Pickup, Y.-S. Liu, K. Edström, J. Guo,

        A. V. Chadwick, L.C. Duda, P.G. Bruce, Charge-compensation in *3d*-transition-metal-

        oxide intercalation cathodes through the generation of localized electron holes on oxygen,

        Nat. Chem. 8 (2016) 684–691. doi:10.1038/nchem.2471.

[14]   D.-H. Seo, J. Lee, A. Urban, R. Malik, S. Kang, G. Ceder, The Structural and Chemical

        Origin of the Oxygen Redox Activity in Layered and Cation-disordered Li-excess

Cathode Materials, Nat. Chem. 8 (2016) 692–697. doi:10.1038/nchem.2524.

[15]   M. Sathiya, J.-B. Leriche, E. Salager, D. Gourier, J.-M. Tarascon, H. Vezin, Electron paramagnetic resonance imaging for real-time monitoring of Li-ion batteries, Nat. Commun. 6 (2015) 6276–6282. doi:10.1038/ncomms7276.

[16]   A. Grimaud, W.T. Hong, Y. Shao-Horn, J.-M. Tarascon, Anionic redox processes for electrochemical devices, Nat. Mater. 15 (2016) 121–126. doi:10.1038/nmat4551.

[17]   C. Wolverton, A. Zunger, First-Principles Prediction of Vacancy Order-Disorder and Intercalation Battery Voltages in LixCoO2, Phys. Rev. Lett. 81 (1998) 606–609. doi:10.1103/PhysRevLett.81.606.

[18]   G. Ceder, Y.-M. Chiang, D.R. Sadoway, M.K. Aydinol, Y.-I. Jang, B. Huang, Identification of Cathode Materials for Lithium Batteries Guided by First-principles Calculations, Nature. 392 (1998) 694–696. doi:10.1038/33647.

[19]   D. Morgan, A. Van der Ven, G. Ceder, Li Conductivity in LixMPO4 (M = Mn, Fe, Co, Ni) Olivine Materials, Electrochem. Solid-State Lett. 7 (2004) A30–A32. doi:10.1149/1.1633511.

[20]   K. Kang, Y.S. Meng, J. Bréger, C.P. Grey, G. Ceder, Electrodes with High Power and High Capacity for Rechargeable Lithium Batteries, Science (80-.). 311 (2006) 977–980. doi:10.1126/science.1122152.

[21]   M.M. Thackeray, C. Wolverton, E.D. Isaacs, Electrical Energy Storage for Transportation-approaching the Limits of, and Going Beyond, Lithium-ion Batteries, Energy Environ. Sci. 5 (2012) 7854–7863. doi:10.1039/c2ee21892e.

[22]   Y.S. Meng, M.E. Arroyo-de Dompablo, First Principles Computational Materials Design

for Energy Storage Materials in Lithium Ion Batteries, Energy Environ. Sci. 2 (2009) 589–609. doi:10.1039/b901825e.

[23] Q. Li, H. Liu, Z. Yao, J. Cheng, T. Li, Y. Li, C. Wolverton, J. Wu, V.P. Dravid, Electrochemistry of Selenium with Sodium and Lithium: Kinetics and Reaction Mechanism, ACS Nano. 10 (2016) 8788–8795. doi:10.1021/acsnano.6b04519.

[24] S. Curtarolo, G.L.W. Hart, M.B. Nardelli, N. Mingo, S. Sanvito, O. Levy, The High-throughput Highway to Computational Materials Design., Nat. Mater. 12 (2013) 191–201. doi:10.1038/nmat3568.

[25] Z. Yao, S. Kim, M. Aykol, Q. Li, J. Wu, J. He, C. Wolverton, Revealing the Conversion Mechanism of Transition Metal Oxide Electrodes during Lithiation from First-Principles, Chem. Mater. 29 (2017) 9011–9022. doi:10.1021/acs.chemmater.7b02058.

[26] R. Khatib, A.-L. Dalverny, M. Saubanère, M. Gaberscek, M.-L. Doublet, Origin of the Voltage Hysteresis in the CoP Conversion Material for Li-Ion Batteries, J. Phys. Chem. C. 117 (2013) 837–849. doi:10.1021/jp310366a.

[27] D. Meggiolaro, G. Gigli, A. Paolone, P. Reale, M.L. Doublet, S. Brutti, Origin of the Voltage Hysteresis of MgH2 Electrodes in Lithium Batteries, J. Phys. Chem. C. 119 (2015) 17044–17052. doi:10.1021/acs.jpcc.5b04615.

[28] L. Li, R. Jacobs, P. Gao, L. Gan, F. Wang, D. Morgan, S. Jin, Origins of Large Voltage Hysteresis in High-Energy-Density Metal Fluoride Lithium-Ion Battery Conversion Electrodes, J. Am. Chem. Soc. 138 (2016) 2838–2848. doi:10.1021/jacs.6b00061.

[29] C. Delacourt, P. Poizot, J.-M. Tarascon, C. Masquelier, The existence of a temperature-driven solid solution in LixFePO4 for $0 \leq x \leq 1$, Nat. Mater. 4 (2005) 254–260.

doi:10.1038/nmat1335.

[30] R. Malik, F. Zhou, G. Ceder, Kinetics of non-equilibrium lithium incorporation in LiFePO4., Nat. Mater. 10 (2011) 587–590. doi:10.1038/nmat3065.

[31] A. Singer, A. Ulvestad, H.-M. Cho, J.W. Kim, J. Maser, R. Harder, Y.S. Meng, O.G. Shpyrko, Nonequilibrium structural dynamics of nanoparticles in LiNi(1/2)Mn(3/2)O4 cathode under operando conditions., Nano Lett. 14 (2014) 5295–5300. doi:10.1021/nl502332b.

[32] R.E. Doe, K.A. Persson, Y.S. Meng, G. Ceder, First-Principles Investigation of the Li−Fe−F Phase Diagram and Equilibrium and Nonequilibrium Conversion Reactions of Iron Fluorides with Lithium, Chem. Mater. 20 (2008) 5274–5283. doi:10.1021/cm801105p.

[33] M.K.Y. Chan, C. Wolverton, J.P. Greeley, First principles simulations of the electrochemical lithiation and delithiation of faceted crystalline silicon., J. Am. Chem. Soc. 134 (2012) 14362–14374. doi:10.1021/ja301766z.

[34] M.Z. Bazant, Theory of chemical kinetics and charge transfer based on nonequilibrium thermodynamics., Acc. Chem. Res. 46 (2013) 1144–1160. doi:10.1021/ar300145c.

[35] A. Jain, S.P. Ong, G. Hautier, W. Chen, W.D. Richards, S. Dacek, S. Cholia, D. Gunter, D. Skinner, G. Ceder, K.A. Persson, Commentary: The Materials Project: A materials genome approach to accelerating materials innovation, APL Mater. 1 (2013) 11002. doi:10.1063/1.4812323.

[36] D. Chang, M.-H. Chen, A. Van der Ven, Factors Contributing to Path Hysteresis of Displacement and Conversion Reactions in Li Ion Batteries, Chem. Mater. 27 (2015)

7593–7600. doi:10.1021/acs.chemmater.5b02356.

[37] H. Kim, H. Kim, H. Kim, J. Kim, G. Yoon, K. Lim, W.-S. Yoon, K. Kang, Understanding Origin of Voltage Hysteresis in Conversion Reaction for Na Rechargeable Batteries: The Case of Cobalt Oxides, Adv. Funct. Mater. 26 (2016) 5042–5050. doi:10.1002/adfm.201601357.

[38] Z.-S. Wu, W. Ren, L. Wen, L. Gao, J. Zhao, Z. Chen, G. Zhou, F. Li, H.-M. Cheng, Graphene anchored with Co3O4 nanoparticles as anode of lithium ion batteries with enhanced reversible capacity and cyclic performance., ACS Nano. 4 (2010) 3187–3194. doi:10.1021/nn100740x.

[39] H. Liu, Q. Li, Z. Yao, L. Li, Y. Li, C. Wolverton, M.C. Hersam, V.P. Dravid, Origin of fracture-resistance to large volume change in Cu-doped Co3O4 electrode, Adv. Mater. (2017) 1704851. doi:10.1002/adma.201704851.

[40] K. He, F. Lin, Y. Zhu, X. Yu, J. Li, R. Lin, D. Nordlund, T.-C. Weng, R.M. Richards, X.-Q. Yang, M.M. Doeff, E.A. Stach, Y. Mo, H.L. Xin, D. Su, Sodiation Kinetics of Metal Oxide Conversion Electrodes: A Comparative Study with Lithiation, Nano Lett. 15 (2015) 5755–5763. doi:10.1021/acs.nanolett.5b01709.

[41] X. Wang, X. Shen, Z. Wang, R. Yu, L. Chen, Atomic-Scale Clarification of Structural Transition of MoS2 upon Sodium Intercalation, ACS Nano. 8 (2014) 11394–11400. doi:10.1021/nn505501v.

[42] K. He, Z. Yao, S. Hwang, N. Li, K. Sun, H. Gan, Y. Du, H. Zhang, C. Wolverton, D. Su, Kinetically-Driven Phase Transformation during Lithiation in Copper Sulfide Nanoflakes, Nano Lett. 17 (2017) 5726–5733. doi:10.1021/acs.nanolett.7b02694.

[43]   H. Koga, L. Croguennec, M. Menetrier, K. Douhil, S. Belin, L. Bourgeois, E. Suard, F. Weill, C. Delmas, Reversible Oxygen Participation to the Redox Processes Revealed for Li1.20Mn0.54Co0.13Ni0.13O2, J. Electrochem. Soc. 160 (2013) A786–A792. doi:10.1149/2.038306jes.

[44]   N. Yabuuchi, M. Takeuchi, M. Nakayama, H. Shiiba, M. Ogawa, K. Nakayama, T. Ohta, D. Endo, T. Ozaki, T. Inamasu, K. Sato, S. Komaba, High-capacity Electrode Materials for Rechargeable Lithium Batteries: Li3NbO4-based System with Cation-disordered Rocksalt Structure, Proc. Natl. Acad. Sci. U. S. A. 112 (2015) 7650–7655. doi:10.1073/pnas.1504901112.

[45]   P.E. Pearce, A.J. Perez, G. Rousse, M. Saubanère, D. Batuk, D. Foix, E. McCalla, A.M. Abakumov, G. Van Tendeloo, M.-L. Doublet, J.-M. Tarascon, Evidence for anionic redox activity in a tridimensional-ordered Li-rich positive electrode β-Li2IrO3, Nat. Mater. 16 (2017) 580–586. doi:10.1038/nmat4864.

[46]   M.M. Thackeray, M.K.Y. Chan, L. Trahey, S. Kirklin, C. Wolverton, Vision for Designing High-Energy, Hybrid Li Ion/Li-O2 Cells, J. Phys. Chem. Lett. 4 (2013) 3607–3611. doi:10.1021/jz4018464.

[47]   K. Luo, M.R. Roberts, R. Hao, N. Guerrini, D.M. Pickup, Y.-S. Liu, K. Edström, J. Guo, A. V. Chadwick, L.C. Duda, P.G. Bruce, Charge-compensation in 3d-transition-metal-oxide intercalation cathodes through the generation of localized electron holes on oxygen, Nat. Chem. 8 (2016) 684–691. doi:10.1038/nchem.2471.

[48]   C. Zhan, Z. Yao, J. Lu, L. Ma, V.A. Maroni, L. Li, E. Lee, E.E. Alp, T. Wu, J. Wen, Y. Ren, C. Johnson, M.M. Thackeray, M.K.Y. Chan, C. Wolverton, K. Amine, Enabling the

high capacity of lithium-rich anti-fluorite lithium iron oxide by simultaneous anionic and cationic redox, Nat. Energy. 2 (2017) 963–971. doi:10.1038/s41560-017-0043-6.

[49]   K. Ozawa, Lithium-ion Rechargeable Batteries with LiCoO2 and Carbon Electrodes: the LiCoO2/C System, Solid State Ionics. 69 (1994) 212–221. doi:10.1016/0167-2738(94)90411-1.

[50]   J.M. Tarascon, M. Armand, Issues and Challenges Facing Rechargeable Lithium Batteries., Nature. 414 (2001) 359–367. doi:10.1038/35104644.

[51]   J.B. Goodenough, Y. Kim, Challenges for Rechargeable Li Batteries, Chem. Mater. 22 (2010) 587–603. doi:10.1021/cm901452z.

[52]   P. Arora, R.E. White, M. Doyle, Capacity Fade Mechanisms and Side Reactions in Lithium-Ion Batteries, J. Electrochem. Soc. 145 (1998) 3647–3667. doi:10.1149/1.1838857.

[53]   D.H. Jang, Y.J. Shin, S.M. Oh, Dissolution of Spinel Oxides and Capacity Losses in 4V Li/LixMn2O4 Cells, J. Electrochem. Soc. 143 (1996) 2204–2211. doi:10.1149/1.1836981.

[54]   J.C. Bachman, S. Muy, A. Grimaud, H.-H. Chang, N. Pour, S.F. Lux, O. Paschos, F. Maglia, S. Lupart, P. Lamp, L. Giordano, Y. Shao-Horn, Inorganic Solid-State Electrolytes for Lithium Batteries: Mechanisms and Properties Governing Ion Conduction, Chem. Rev. 116 (2016) 140–162. doi:10.1021/acs.chemrev.5b00563.

[55]   A. Rabenau, Lithium Nitride and Related Materials Case Study of the Use of Modern Solid State Research Techniques, Solid State Ionics. 6 (1982) 277–293. doi:10.1016/0167-2738(82)90012-1.

[56]   H. Maekawa, M. Matsuo, H. Takamura, M. Ando, Y. Noda, T. Karahashi, S. Orimo,

Halide-stabilized LiBH4, A Room-temperature Lithium Fast-ion Conductor, J. Am. Chem. Soc. 131 (2009) 894–895. doi:10.1021/ja807392k.

[57]   M. Matsuo, H. Takamura, H. Maekawa, H.-W. Li, S. Orimo, Stabilization of Lithium Superionic Conduction Phase and Enhancement of Conductivity of LiBH4 by LiCl Addition, Appl. Phys. Lett. 94 (2009) 084103–084105. doi:10.1063/1.3088857.

[58]   D. Sveinbjörnsson, J.S.G. Myrdal, D. Blanchard, J.J. Bentzen, T. Hirata, M.B. Mogensen, P. Norby, S.-I. Orimo, T. Vegge, Effect of Heat Treatment on the Lithium Ion Conduction of the LiBH4–LiI Solid Solution, J. Phys. Chem. C. 117 (2013) 3249–3257. doi:10.1021/jp310050g.

[59]   M.B. Ley, D.B. Ravnsbæk, Y. Filinchuk, Y.-S. Lee, R. Janot, Y.W. Cho, J. Skibsted, T.R. Jensen, LiCe(BH4)3Cl, a New Lithium-Ion Conductor and Hydrogen Storage Material with Isolated Tetranuclear Anionic Clusters, Chem. Mater. 24 (2012) 1654–1663. doi:10.1021/cm300792t.

[60]   M.B. Ley, S. Boulineau, R. Janot, Y. Filinchuk, T.R. Jensen, New Li Ion Conductors and Solid State Hydrogen Storage Materials: LiM(BH4)3Cl, M = La, Gd, J. Phys. Chem. C. 116 (2012) 21267–21276. doi:10.1021/jp307762g.

[61]   Y. Inaguma, C. Liquan, M. Itoh, T. Nakamura, T. Uchida, H. Ikuta, M. Wakihara, High Ionic Conductivity in Lithium Lanthanum Titanate, Solid State Commun. 86 (1993) 689–693. doi:10.1016/0038-1098(93)90841-A.

[62]   H.-J. Deiseroth, S.-T. Kong, H. Eckert, J. Vannahme, C. Reiner, T. Zaiß, M. Schlosser, Li6PS5X: A Class of Crystalline Li-Rich Solids with an Unusually High Li+ Mobility, Angew. Chemie Int. Ed. 47 (2008) 755–758. doi:10.1002/anie.200703900.

[63]   V. Thangadurai, J. Schwenzel, W. Weppner, Tailoring Ceramics for Specific

       Applications: A Case Study of the Development of All-solid-state Lithium Batteries,

       Ionics (Kiel). 11 (2005) 11–23. doi:10.1007/BF02430397.

[64]   K. Arbi, J.M. Rojo, J. Sanz, Lithium Mobility in Titanium Based NASICON Li1+xTi2-

       xAlx(PO4)3 and LiTi2-xZrx(PO4)3 Materials Followed by NMR and Impedance

       Spectroscopy, J. Eur. Ceram. Soc. 27 (2007) 4215–4218.

       http://cat.inist.fr/?aModele=afficheN&cpsidt=18959015 (accessed August 14, 2014).

[65]   P.G. Bruce, The A-C Conductivity of Polycrystalline LISICON, Li2+2xZn1-xGeO4, and

       a Model for Intergranular Constriction Resistances, J. Electrochem. Soc. 130 (1983) 662–

       669. doi:10.1149/1.2119778.

[66]   N. Kamaya, K. Homma, Y. Yamakawa, M. Hirayama, R. Kanno, M. Yonemura, T.

       Kamiyama, Y. Kato, S. Hama, K. Kawamoto, A. Mitsui, A Lithium Superionic

       Conductor, Nat. Mater. 10 (2011) 682–686. doi:10.1038/nmat3066.

[67]   S.P. Ong, Y. Mo, W.D. Richards, L. Miara, H.S. Lee, G. Ceder, Phase Stability,

       Electrochemical Stability and Ionic Conductivity of The Li10±1MP2X12 (M = Ge, Si, Sn,

       Al or P, and X = O, S or Se) Family of Superionic Conductors, Energy Environ. Sci. 6

       (2013) 148–156. doi:10.1039/c2ee23355j.

[68]   P. Hohenberg, Inhomogeneous Electron Gas, Phys. Rev. 136 (1964) B864–B871.

       doi:10.1103/PhysRev.136.B864.

[69]   W. Kohn, L.J. Sham, Self-Consistent Equations Including Exchange and Correlation

       Effects, Phys. Rev. 140 (1965) A1133–A1138. doi:10.1103/PhysRev.140.A1133.

[70]   J. Hafner, C. Wolverton, G. Ceder, Toward Computational Materials Design: The Impact

of Density Functional Theory on Materials Research, MRS Bull. 31 (2011) 659–668. doi:10.1557/mrs2006.174.

[71]   V.I. Anisimov, F. Aryasetiawan, A.I. Lichtenstein, First-principles calculations of the electronic structure and spectra of strongly correlated systems: the LDA + U method, J. Phys. Condens. Matter. 9 (1997) 767–808. doi:10.1088/0953-8984/9/4/002.

[72]   M. Cococcioni, S. de Gironcoli, Linear response approach to the calculation of the effective interaction parameters in the LDA+U method, Phys. Rev. B. 71 (2005) 035105–035120. doi:10.1103/PhysRevB.71.035105.

[73]   S. Kirklin, B. Meredig, C. Wolverton, High-Throughput Computational Screening of New Li-Ion Battery Anode Materials, Adv. Energy Mater. 3 (2013) 252–262. doi:10.1002/aenm.201200593.

[74]   M.K. Aydinol, A.F. Kohan, G. Ceder, K. Cho, J. Joannopoulos, Ab initio study of lithium intercalation in metal oxides and metal dichalcogenides, Phys. Rev. B. 56 (1997) 1354–1365. doi:10.1103/PhysRevB.56.1354.

[75]   C.G. Van de Walle, First-principles Calculations for Defects and Impurities: Applications to III-nitrides, J. Appl. Phys. 95 (2004) 3851–3879. doi:10.1063/1.1682673.

[76]   K.J. Michel, Y. Zhang, C. Wolverton, Fast Mass Transport Kinetics in B20H16 : A High-Capacity Hydrogen Storage Material, J. Phys. Chem. C. 117 (2013) 19295–19301. doi:10.1021/jp402669u.

[77]   H. Eyring, The Activated Complex in Chemical Reactions, J. Chem. Phys. 3 (1935) 107–115. doi:10.1063/1.1749604.

[78]   G.H. Vineyard, Frequency Factors and Isotope Effects in Solid State Rate Processes, J.

Phys. Chem. Solids. 3 (1957) 121–127. doi:10.1016/0022-3697(57)90059-8.

[79] K.J. Michel, V. Ozoliņš, Vacancy Diffusion in NaAlH4 and Na3AlH6, J. Phys. Chem. C. 115 (2011) 21465–21472. doi:10.1021/jp203675e.

[80] K.J. Michel, C. Wolverton, Symmetry Building Monte Carlo-based Crystal Structure Prediction, Comput. Phys. Commun. 185 (2014) 1389–1393. doi:10.1016/j.cpc.2014.01.015.

[81] P. Poizot, S. Laruelle, S. Grugeon, L. Dupont, J.M. Tarascon, Nano-sized transition-metal oxides as negative-electrode materials for lithium-ion batteries., Nature. 407 (2000) 496–499. doi:10.1038/35035045.

[82] F. Badway, I. Plitz, S. Grugeon, S. Laruelle, M. Dollé, A.S. Gozdz, J.-M. Tarascon, Metal Oxides as Negative Electrode Materials in Li-Ion Cells, Electrochem. Solid-State Lett. 5 (2002) A115–A118. doi:10.1149/1.1472303.

[83] M. Thackeray, S. Baker, K. Adendorff, J. Goodenough, Lithium insertion into Co3O4: A preliminary investigation, Solid State Ionics. 17 (1985) 175–181. doi:10.1016/0167-2738(85)90069-4.

[84] Y.-M. Kang, K.-T. Kim, K.-Y. Lee, S.-J. Lee, J.-H. Jung, J.-Y. Lee, Improvement of Initial Coulombic Efficiency of Co3O4 by Ballmilling Using Ni as an Additive, J. Electrochem. Soc. 150 (2003) A1538–A1543. doi:10.1149/1.1617299.

[85] S.A. Needham, G.X. Wang, K. Konstantinov, Y. Tournayre, Z. Lao, H.K. Liu, Electrochemical Performance of Co3O4–C Composite Anode Materials, Electrochem. Solid-State Lett. 9 (2006) A315–A319. doi:10.1149/1.2197108.

[86] P.A. Connor, J.T.. Irvine, Combined X-ray study of lithium (tin) cobalt oxide matrix

negative electrodes for Li-ion batteries, Electrochim. Acta. 47 (2002) 2885–2892. doi:10.1016/S0013-4686(02)00144-5.

[87]   Y. Wang, Q.-Z. Qin, A Nanocrystalline NiO Thin-Film Electrode Prepared by Pulsed Laser Ablation for Li-Ion Batteries, J. Electrochem. Soc. 149 (2002) A873–A878. doi:10.1149/1.1481715.

[88]   D. Larcher, G. Sudant, J.-B. Leriche, Y. Chabre, J.-M. Tarascon, The Electrochemical Reduction of Co3O4 in a Lithium Cell, J. Electrochem. Soc. 149 (2002) A234–A241. doi:10.1149/1.1435358.

[89]   K. He, H.L. Xin, K. Zhao, X. Yu, D. Nordlund, T.-C. Weng, J. Li, Y. Jiang, C.A. Cadigan, R.M. Richards, M.M. Doeff, X.-Q. Yang, E.A. Stach, J. Li, F. Lin, D. Su, Transitions from Near-Surface to Interior Redox upon Lithiation in Conversion Electrode Materials, Nano Lett. 15 (2015) 1437–1444. doi:10.1021/nl5049884.

[90]   P. Poizot, S. Laruelle, S. Grugeon, J.-M. Tarascon, Rationalization of the Low-Potential Reactivity of 3d-Metal-Based Inorganic Compounds toward Li, J. Electrochem. Soc. 149 (2002) A1212–A1217. doi:10.1149/1.1497981.

[91]   G.X. Wang, Y. Chen, K. Konstantinov, J. Yao, J. Ahn, H.K. Liu, S.X. Dou, Nanosize cobalt oxides as anode materials for lithium-ion batteries, J. Alloys Compd. 340 (2002) L5–L10. doi:10.1016/S0925-8388(02)00005-1.

[92]   Y.-M. Kang, M.-S. Song, J.-H. Kim, H.-S. Kim, M.-S. Park, J.-Y. Lee, H.K. Liu, S.X. Dou, A Study on the Charge–discharge Mechanism of Co3O4 as an Anode for the Li Ion Secondary Battery, Electrochim. Acta. 50 (2005) 3667–3673. doi:10.1016/j.electacta.2005.01.012.

[93] G. Rollmann, M.E. Gruner, A. Hucht, R. Meyer, P. Entel, M.L. Tiago, J.R. Chelikowsky, Shellwise Mackay Transformation in Iron Nanoclusters, Phys. Rev. Lett. 99 (2007) 083402–083405. doi:10.1103/PhysRevLett.99.083402.

[94] F. Wang, H.-C. Yu, M.-H. Chen, L. Wu, N. Pereira, K. Thornton, A. Van der Ven, Y. Zhu, G.G. Amatucci, J. Graetz, Tracking lithium transport and electrochemical reactions in nanoparticles., Nat. Commun. 3 (2012) 1201–1208. doi:10.1038/ncomms2185.

[95] X.W. Lou, D. Deng, J.Y. Lee, J. Feng, L.A. Archer, Self-Supported Formation of Needlelike Co3O4 Nanotubes and Their Application as Lithium-Ion Battery Electrodes, Adv. Mater. 20 (2008) 258–262. doi:10.1002/adma.200702412.

[96] Y. Li, B. Tan, Y. Wu, Freestanding mesoporous quasi-single-crystalline CO3O4 nanowire arrays., J. Am. Chem. Soc. 128 (2006) 14258–14259. doi:10.1021/ja065308q.

[97] X. Wang, X.-L. Wu, Y.-G. Guo, Y. Zhong, X. Cao, Y. Ma, J. Yao, Synthesis and Lithium Storage Properties of Co3O4 Nanosheet-Assembled Multishelled Hollow Spheres, Adv. Funct. Mater. 20 (2010) 1680–1686. doi:10.1002/adfm.200902295.

[98] B. Varghese, M. V. Reddy, Z. Yanwu, C.S. Lit, T.C. Hoong, G. V. Subba Rao, B.V.R. Chowdari, A.T.S. Wee, C.T. Lim, C.-H. Sow, Fabrication of NiO Nanowall Electrodes for High Performance Lithium Ion Battery, Chem. Mater. 20 (2008) 3360–3367. doi:10.1021/cm703512k.

[99] E. Hosono, S. Fujihara, I. Honma, H. Zhou, The High Power and High Energy Densities Li Ion Storage Device by Nanocrystalline and Mesoporous Ni/NiO Covered Structure, Electrochem. Commun. 8 (2006) 284–288. doi:10.1016/j.elecom.2005.11.023.

[100] H.-C. Yu, C. Ling, J. Bhattacharya, J.C. Thomas, K. Thornton, A. Van der Ven, Designing

the next generation high capacity battery electrodes, Energy Environ. Sci. 7 (2014) 1760–1768. doi:10.1039/c3ee43154a.

[101] U. Boesenberg, M.A. Marcus, A.K. Shukla, T. Yi, E. McDermott, P.F. Teh, M. Srinivasan, A. Moewes, J. Cabana, Asymmetric pathways in the electrochemical conversion reaction of NiO as battery electrode with high storage capacity, Sci. Rep. 4 (2014) 7133–7141. doi:10.1038/srep07133.

[102] A. Ponrouch, J. Cabana, R. Dugas, J.L. Slack, M.R. Palacín, Electroanalytical study of the viability of conversion reactions as energy storage mechanisms, RSC Adv. 4 (2014) 35988–35996. doi:10.1039/C4RA05189K.

[103] G. Kresse, J. Hafner, Ab Initio Molecular Dynamics for Liquid Metals, Phys. Rev. B. 47 (1993) 558–561. doi:10.1103/PhysRevB.47.558.

[104] G. Kresse, J. Hafner, Ab Initio Molecular-dynamics Simulation of the Liquid-metal-amorphous-semiconductor Transition in Germanium, Phys. Rev. B. 49 (1994) 14251–14269. doi:10.1103/PhysRevB.49.14251.

[105] G. Kresse, J. Furthmüller, Efficiency of Ab-initio Total Energy Calculations for Metals and Semiconductors Using a Plane-wave Basis Set, Comput. Mater. Sci. 6 (1996) 15–50. doi:10.1016/0927-0256(96)00008-0.

[106] G. Kresse, Efficient Iterative Schemes for Ab Initio Total-energy Calculations Using a Plane-Wave Basis Set, Phys. Rev. B. 54 (1996) 11169–11186. doi:10.1103/PhysRevB.54.11169.

[107] P.E. Blöchl, Projector Augmented-wave Method, Phys. Rev. B. 50 (1994) 17953–17979. doi:10.1103/PhysRevB.50.17953.

[108] J.P. Perdew, M. Ernzerhof, K. Burke, Rationale for Mixing Exact Exchange with Density Functional Approximations, J. Chem. Phys. 105 (1996) 9982–9985. doi:10.1063/1.472933.

[109] S.L. Dudarev, S.Y. Savrasov, C.J. Humphreys, A.P. Sutton, Electron-energy-loss Spectra and The Structural Stability of Nickel Oxide: An LSDA+U Study, Phys. Rev. B. 57 (1998) 1505–1509. doi:10.1103/PhysRevB.57.1505.

[110] J. Chen, X. Wu, A. Selloni, Electronic structure and bonding properties of cobalt oxide in the spinel structure, Phys. Rev. B. 83 (2011) 245204–245210. doi:10.1103/PhysRevB.83.245204.

[111] J. Chen, A. Selloni, Electronic states and magnetic structure at the Co3O4 (110) surface: A first-principles study, Phys. Rev. B. 85 (2012) 085306–085314. doi:10.1103/PhysRevB.85.085306.

[112] L. Wang, T. Maxisch, G. Ceder, Oxidation Energies of Transition Metal oxides within the GGA+U framework, Phys. Rev. B. 73 (2006) 195107–195112. doi:10.1103/PhysRevB.73.195107.

[113] J.E. Saal, S. Kirklin, M. Aykol, B. Meredig, C. Wolverton, Materials Design and Discovery with High-Throughput Density Functional Theory: The Open Quantum Materials Database (OQMD), JOM. 65 (2013) 1501–1509. doi:10.1007/s11837-013-0755-4.

[114] S. Kirklin, J.E. Saal, B. Meredig, A. Thompson, J.W. Doak, M. Aykol, S. Rühl, C. Wolverton, The Open Quantum Materials Database (OQMD): Assessing the Accuracy of DFT Formation Energies, Npj Comput. Mater. 1 (2015) 15010–15024.

doi:10.1038/npjcompumats.2015.10.

[115] S. Kirklin, J.E. Saal, V.I. Hegde, C. Wolverton, High-throughput Computational Search for Strengthening Precipitates in Alloys, Acta Mater. 102 (2016) 125–135. doi:10.1016/j.actamat.2015.09.016.

[116] F. Zhou, C.A. Marianetti, M. Cococcioni, D. Morgan, G. Ceder, Phase Separation in LixFePO4 Induced by Correlation Effects, Phys. Rev. B. 69 (2004) 201101–201104. doi:10.1103/PhysRevB.69.201101.

[117] L. Alberts, E.W. Lee, Magnetostriction in Antiferromagnetic Nickel Oxide, Proc. Phys. Soc. 78 (1961) 728–733. doi:10.1088/0370-1328/78/5/312.

[118] A. R. Akbarzadeh, V. Ozoliņš, C. Wolverton, First-Principles Determination of Multicomponent Hydride Phase Diagrams: Application to the Li-Mg-N-H System, Adv. Mater. 19 (2007) 3233–3239. doi:10.1002/adma.200700843.

[119] C. Wolverton, X.-Y. Yan, R. Vijayaraghavan, V. Ozoliņš, Incorporating first-principles energetics in computational thermodynamics approaches, Acta Mater. 50 (2002) 2187–2197. doi:10.1016/S1359-6454(01)00430-X.

[120] A. Belsky, M. Hellenbrandt, V.L. Karen, P. Luksch, New Developments in the Inorganic Crystal Structure Database (ICSD): Accessibility in Support of Materials Research and Design, Acta Crystallogr. Sect. B Struct. Sci. 58 (2002) 364–369. doi:10.1107/S0108768102006948.

[121] S. Grindy, B. Meredig, S. Kirklin, J.E. Saal, C. Wolverton, Approaching Chemical Accuracy with Density Functional Calculations: Diatomic Energy Corrections, Phys. Rev. B. 87 (2013) 075150–075157. doi:10.1103/PhysRevB.87.075150.

[122] V. Stevanović, S. Lany, X. Zhang, A. Zunger, Correcting density functional theory for accurate predictions of compound enthalpies of formation: Fitted elemental-phase reference energies, Phys. Rev. B. 85 (2012) 115104–115115. doi:10.1103/PhysRevB.85.115104.

[123] SGTE, Thermodynamic Properties of Inorganic Materials, Berlin, Heidelberg, 1999.

[124] P. Nash, Thermodynamic database, (2013). https://tptc.iit.edu/index.php/thermo-database.

[125] K.J. Michel, V. Ozoliņš, Native Defect Concentrations in NaAlH4 and Na3AlH6, J. Phys. Chem. C. 115 (2011) 21443–21453. doi:10.1021/jp203672u.

[126] L. Ward, K. Michel, Materials/Mint: Initial Release, Doi.org. (2016). doi:10.5281/zenodo.167890.

[127] G. Hart, R. Forcade, Algorithm for Generating Derivative Structures, Phys. Rev. B. 77 (2008) 224115–224126. doi:10.1103/PhysRevB.77.224115.

[128] G.L.W. Hart, R.W. Forcade, Generating derivative structures from multilattices: Algorithm and application to hcp alloys, Phys. Rev. B. 80 (2009) 014120–014127. doi:10.1103/PhysRevB.80.014120.

[129] G.L.W. Hart, L.J. Nelson, R.W. Forcade, Generating Derivative Structures at A Fixed Concentration, Comput. Mater. Sci. 59 (2012) 101–107. doi:10.1016/j.commatsci.2012.02.015.

[130] E. Cockayne, A. van de Walle, Building effective models from sparse but precise data: Application to an alloy cluster expansion model, Phys. Rev. B. 81 (2010) 012104–012107. doi:10.1103/PhysRevB.81.012104.

[131] A. van de Walle, Multicomponent Multisublattice Alloys, Nonconfigurational Entropy

and Other Additions to the Alloy Theoretic Automated Toolkit, Calphad. 33 (2009) 266–290.

[132] A. van de Walle, Methods for First-Principles Alloy Thermodynamics, JOM - J. Min. Met. Mat. S. 65 (2013) 1523–1532.

[133] H. Bin, Z. Yao, S. Zhu, C. Zhu, H. Pan, Z. Chen, C. Wolverton, D. Zhang, A High-performance Anode Material Based on FeMnO3/graphene Composite, J. Alloys Compd. 695 (2017) 1223–1230. doi:10.1016/j.jallcom.2016.10.249.

[134] R. van de Krol, A. Goossens, E.A. Meulenkamp, In Situ X-Ray Diffraction of Lithium Intercalation in Nanostructured and Thin Film Anatase TiO2, J. Electrochem. Soc. 146 (1999) 3150–3154. doi:10.1149/1.1392447.

[135] Y. Li, B. Tan, Y. Wu, Mesoporous Co3O4 nanowire arrays for lithium ion batteries with high capacity and rate capability., Nano Lett. 8 (2008) 265–270. doi:10.1021/nl0725906.

[136] H. Kim, D.-H. Seo, S.-W. Kim, J. Kim, K. Kang, Highly reversible Co3O4/graphene hybrid anode for lithium rechargeable batteries, Carbon N. Y. 49 (2011) 326–332. doi:10.1016/j.carbon.2010.09.033.

[137] Y.J. Mai, S.J. Shi, D. Zhang, Y. Lu, C.D. Gu, J.P. Tu, NiO–graphene hybrid as an anode material for lithium ion batteries, J. Power Sources. 204 (2012) 155–161. doi:10.1016/j.jpowsour.2011.12.038.

[138] E. Sanville, S.D. Kenny, R. Smith, G. Henkelman, Improved Grid-based Algorithm for Bader Charge Allocation., J. Comput. Chem. 28 (2007) 899–908. doi:10.1002/jcc.20575.

[139] W. Tang, E. Sanville, G. Henkelman, A Grid-based Bader Analysis Algorithm without Lattice Bias, J. Phys. Condens. Matter. 21 (2009) 084204–084210. doi:10.1088/0953-

8984/21/8/084204.

[140] B.-M. Chae, E.-S. Oh, Y.-K. Lee, Conversion mechanisms of cobalt oxide anode for Li-ion battery: In situ X-ray absorption fine structure studies, J. Power Sources. 274 (2015) 748–754. doi:10.1016/j.jpowsour.2014.10.108.

[141] Y.N. Zhuravlev, O.S. Obolonskaya, Structure, Mechanical Stability, and Chemical Bond in Alkali Metal Oxides, J. Struct. Chem. 51 (2010) 1005–1013. doi:10.1007/s10947-010-0157-1.

[142] J. Häglund, A. Fernández Guillermet, G. Grimvall, M. Körling, Theory of Bonding in Transition-metal Carbides and Nitrides, Phys. Rev. B. 48 (1993) 11685–11691. doi:10.1103/PhysRevB.48.11685.

[143] Q. Li, J. Wu, Z. Yao, M.M. Thackeray, C. Wolverton, V.P. Dravid, Dynamic imaging of metastable reaction pathways in lithiated metal oxide electrodes, Nano Energy. 44 (2017) 15–22. doi:10.1016/j.nanoen.2017.11.052.

[144] G. Evmenenko, T.T. Fister, D.B. Buchholz, Q. Li, K.-S. Chen, J. Wu, V.P. Dravid, M.C. Hersam, P. Fenter, M.J. Bedzyk, Morphological Evolution of Multilayer Ni/NiO Thin Film Electrodes during Lithiation, ACS Appl. Mater. Interfaces. 8 (2016) 19979–19986. doi:10.1021/acsami.6b05040.

[145] M.T. McDowell, S.W. Lee, J.T. Harris, B.A. Korgel, C. Wang, W.D. Nix, Y. Cui, In Situ TEM of Two-Phase Lithiation of Amorphous Silicon Nanospheres, Nano Lett. 13 (2013) 758–764. doi:10.1021/nl3044508.

[146] Q. Li, J. Wu, J. Xu, V.P. Dravid, Synergistic sodiation of cobalt oxide nanoparticles and conductive carbon nanotubes (CNTs) for sodium-ion batteries, J. Mater. Chem. A. 4

(2016) 8669–8675. doi:10.1039/C6TA02051H.

[147] J.Y. Huang, L. Zhong, C.M. Wang, J.P. Sullivan, W. Xu, L.Q. Zhang, S.X. Mao, N.S. Hudak, X.H. Liu, A. Subramanian, H. Fan, L. Qi, A. Kushima, J. Li, In situ observation of the electrochemical lithiation of a single SnO_2 nanowire electrode., Science. 330 (2010) 1515–1520. doi:10.1126/science.1195628.

[148] X.H. Liu, J.Y. Huang, B. Scrosati, J.M. Tarascon, W. Van Schalkwijk, J. Vlassak, E. Kaxiras, F. Wu, Q. Li, D.R. Baer, N. Salmon, E. Epstein, S.T. Picraux, T. Zhu, J. Li, J.P. Sullivan, J. Cumings, C. Wang, S.X. Mao, Z.Z. Ye, S. Zhang, J.Y. Huang, In situ TEM electrochemistry of anode materials in lithium ion batteries, Energy Environ. Sci. 4 (2011) 3844–3860. doi:10.1039/c1ee01918j.

[149] C.M. Julien, Lithium intercalated compounds: Charge transfer and related properties, Mater. Sci. Eng. R Reports. 40 (2003) 47–102. doi:10.1016/S0927-796X(02)00104-3.

[150] J. Wan, W. Bao, Y. Liu, J. Dai, F. Shen, L. Zhou, X. Cai, D. Urban, Y. Li, K. Jungjohann, M.S. Fuhrer, L. Hu, In Situ Investigations of Li-MoS2 with Planar Batteries, Adv. Energy Mater. 5 (2015) 1401742–1401748. doi:10.1002/aenm.201401742.

[151] X. Hu, W. Zhang, X. Liu, Y. Mei, Y. Huang, Nanostructured Mo-based electrode materials for electrochemical energy storage, Chem. Soc. Rev. 44 (2015) 2376–2404. doi:10.1039/C4CS00350K.

[152] Z. Zeng, X. Zhang, K. Bustillo, K. Niu, C. Gammer, J. Xu, H. Zheng, In Situ Study of Lithiation and Delithiation of MoS2 Nanosheets Using Electrochemical Liquid Cell Transmission Electron Microscopy, Nano Lett. 15 (2015) 5214–5220. doi:10.1021/acs.nanolett.5b02483.

[153] A. Kushima, X. Qian, P. Zhao, S. Zhang, J. Li, Ripplocations in van der Waals Layers, Nano Lett. 15 (2015) 1302–1308. doi:10.1021/nl5045082.

[154] P. Gao, L. Wang, Y.-Y. Zhang, Y. Huang, L. Liao, P. Sutter, K. Liu, D. Yu, E.-G. Wang, High-Resolution Tracking Asymmetric Lithium Insertion and Extraction and Local Structure Ordering in SnS2, Nano Lett. 16 (2016) 5582–5588. doi:10.1021/acs.nanolett.6b02136.

[155] J.-S. Chung, H.-J. Sohn, Electrochemical behaviors of CuS as a cathode material for lithium secondary batteries, J. Power Sources. 108 (2002) 226–231. doi:10.1016/S0378-7753(02)00024-1.

[156] A. Débart, L. Dupont, R. Patrice, J.-M. Tarascon, Reactivity of transition metal (Co, Ni, Cu) sulphides versus lithium: The intriguing case of the copper sulphide, Solid State Sci. 8 (2006) 640–651. doi:10.1016/J.SOLIDSTATESCIENCES.2006.01.013.

[157] B. Jache, B. Mogwitz, F. Klein, P. Adelhelm, Copper sulfides for rechargeable lithium batteries: Linking cycling stability to electrolyte composition, J. Power Sources. 247 (2014) 703–711. doi:10.1016/J.JPOWSOUR.2013.08.136.

[158] X. Li, X. He, C. Shi, B. Liu, Y. Zhang, S. Wu, Z. Zhu, J. Zhao, Synthesis of One-Dimensional Copper Sulfide Nanorods as High-Performance Anode in Lithium Ion Batteries, ChemSusChem. 7 (2014) 3328–3333. doi:10.1002/cssc.201402862.

[159] Y. Wang, X. Zhang, P. Chen, H. Liao, S. Cheng, In situ preparation of CuS cathode with unique stability and high rate performance for lithium ion batteries, Electrochim. Acta. 80 (2012) 264–268. doi:10.1016/J.ELECTACTA.2012.07.004.

[160] K. Sun, D. Su, Q. Zhang, D.C. Bock, A.C. Marschilok, K.J. Takeuchi, E.S. Takeuchi, H.

Gan, Interaction of CuS and Sulfur in Li-S Battery System, J. Electrochem. Soc. 162 (2015) A2834–A2839. doi:10.1149/2.1021514jes.

[161] Y. Chen, C. Davoisne, J.-M. Tarascon, C. Guéry, Growth of single-crystal copper sulfide thin films via electrodeposition in ionic liquid media for lithium ion batteries, J. Mater. Chem. 22 (2012) 5295–5299. doi:10.1039/c2jm16692e.

[162] Y. Ren, H. Wei, B. Yang, J. Wang, J. Ding, "Double-Sandwich-Like" CuS@reduced graphene oxide as an Anode in Lithium Ion Batteries with Enhanced Electrochemical Performance, Electrochim. Acta. 145 (2014) 193–200. doi:10.1016/J.ELECTACTA.2014.08.049.

[163] Y. Du, Z. Yin, J. Zhu, X. Huang, X.-J. Wu, Z. Zeng, Q. Yan, H. Zhang, A general method for the large-scale synthesis of uniform ultrathin metal sulphide nanocrystals, Nat. Commun. 3 (2012) 1177. doi:10.1038/ncomms2181.

[164] H. Peelaers, C.G. Van de Walle, First-principles study of van der Waals interactions in MoS2 and MoO3, J. Phys. Condens. Matter. 26 (2014) 305502–305508. doi:10.1088/0953-8984/26/30/305502.

[165] J. Xiao, D. Choi, L. Cosimbescu, P. Koech, J. Liu, J.P. Lemmon, Exfoliated MoS2 Nanocomposite as an Anode Material for Lithium Ion Batteries, Chem. Mater. 22 (2010) 4522–4524. doi:10.1021/cm101254j.

[166] Y.-X. Wang, K.H. Seng, S.-L. Chou, J.-Z. Wang, Z. Guo, D. Wexler, H.-K. Liu, S.-X. Dou, Reversible sodium storage via conversion reaction of a MoS2–C composite, Chem. Commun. 50 (2014) 10730–10733. doi:10.1039/C4CC00294F.

[167] P. Gao, L. Wang, Y. Zhang, Y. Huang, K. Liu, Atomic-Scale Probing of the Dynamics of

Sodium Transport and Intercalation-Induced Phase Transformations in MoS2, ACS Nano. 9 (2015) 11296–11301. doi:10.1021/acsnano.5b04950.

[168] Y. Liang, H.D. Yoo, Y. Li, J. Shuai, H.A. Calderon, F.C. Robles Hernandez, L.C. Grabow, Y. Yao, Interlayer-Expanded Molybdenum Disulfide Nanocomposites for Electrochemical Magnesium Storage, Nano Lett. 15 (2015) 2194–2202. doi:10.1021/acs.nanolett.5b00388.

[169] R.B. Somoano, V. Hadek, A. Rembaum, Alkali metal intercalates of molybdenum disulfide, J. Chem. Phys. 58 (1973) 697–701. doi:10.1063/1.1679256.

[170] G.S. Bang, K.W. Nam, J.Y. Kim, J. Shin, J.W. Choi, S.-Y. Choi, Effective Liquid-Phase Exfoliation and Sodium Ion Battery Application of MoS2 Nanosheets, ACS Appl. Mater. Interfaces. 6 (2014) 7084–7089. doi:10.1021/am4060222.

[171] V. Petkov, S.J.L. Billinge, P. Larson, S.D. Mahanti, T. Vogt, K.K. Rangan, M.G. Kanatzidis, Structure of nanocrystalline materials using atomic pair distribution function analysis: Study of LiMoS2, Phys. Rev. B. 65 (2002) 092105–092108. doi:10.1103/PhysRevB.65.092105.

[172] X. Rocquefelte, I. Bouessay, F. Boucher, P. Gressier, G. Ouvrard, Synergetic Theoretical and Experimental Structure Determination of Nanocrystalline Materials: Study of LiMoS2, 2003. doi:10.1016/S0022-4596(03)00330-X.

[173] M. Freire, N. V. Kosova, C. Jordy, D. Chateigner, O.I. Lebedev, A. Maignan, V. Pralong, A new active Li–Mn–O compound for high energy density Li-ion batteries, Nat. Mater. 15 (2016) 173–177. doi:10.1038/nmat4479.

[174] Z. Zhu, A. Kushima, Z. Yin, L. Qi, K. Amine, J. Lu, J. Li, Anion-redox nanolithia

cathodes for Li-ion batteries, Nat. Energy. 1 (2016) 16111–16117. doi:10.1038/nenergy.2016.111.

[175] S. Okuoka, Y. Ogasawara, Y. Suga, M. Hibino, T. Kudo, H. Ono, K. Yonehara, Y. Sumida, Y. Yamada, A. Yamada, M. Oshima, E. Tochigi, N. Shibata, Y. Ikuhara, N. Mizuno, A New Sealed Lithium-Peroxide Battery with a Co-Doped Li2O Cathode in a Superconcentrated Lithium Bis(fluorosulfonyl)amide Electrolyte, Sci. Rep. 4 (2015) 5684–5689. doi:10.1038/srep05684.

[176] Y. Ogasawara, M. Hibino, H. Kobayashi, T. Kudo, D. Asakura, Y. Nanba, E. Hosono, N. Nagamura, Y. Kitada, I. Honma, M. Oshima, S. Okuoka, H. Ono, K. Yonehara, Y. Sumida, N. Mizuno, Charge/discharge mechanism of a new Co-doped Li2O cathode material for a rechargeable sealed lithium-peroxide battery analyzed by X-ray absorption spectroscopy, J. Power Sources. 287 (2015) 220–225. doi:10.1016/J.JPOWSOUR.2015.04.050.

[177] K. Harada, M. Hibino, H. Kobayashi, Y. Ogasawara, S. Okuoka, K. Yonehara, H. Ono, Y. Sumida, K. Yamaguchi, T. Kudo, N. Mizuno, Electrochemical reactions and cathode properties of Fe-doped Li2O for the hermetically sealed lithium peroxide battery, J. Power Sources. 322 (2016) 49–56. doi:10.1016/j.jpowsour.2016.04.141.

[178] S. Narukawa, Anti-fluorite Type Li6CoO4, Li5FeO4, and Li6MnO4 As the Cathode for Lithium Secondary Batteries, Solid State Ionics. 122 (1999) 59–64. doi:10.1016/S0167-2738(99)00018-1.

[179] N. Imanishi, Y. Inoue, A. Hirano, M. Ueda, Y. Takeda, H. Sakaebe, M. Tabuchi, Antifluorite compounds, Li5+xFe1−xCoxO4, as a lithium intercalation host, J. Power

Sources. 146 (2005) 21–26. doi:10.1016/j.jpowsour.2005.03.010.

[180] Y.-G. Lim, D. Kim, J.-M. Lim, J.-S. Kim, J.-S. Yu, Y.-J. Kim, D. Byun, M. Cho, K. Cho, M.-S. Park, R. Kotz, M. Carlen, A.D. Pasquier, I. Plitz, S. Menocal, G. Amatucci, W. Li, G. Joos, M.E. Glavin, P.K.W. Chan, S. Armstrong, W.G. Hurley, S. Vazquez, S.M. Lukic, E. Galvan, L.G. Franquelo, J.M. Carrasco, J. Cao, A. Emadi, T.M. Masaud, K. Lee, P.K. Sen, I. Hadjipaschalis, A. Poullikkas, V. Efthimiou, C. Liu, F. Li, L.-P. Ma, H.-M. Cheng, G.G. Amatucci, F. Badway, A.D. Pasquier, T. Zheng, A. Yoshino, T. Tsubata, M. Shimoyamada, H. Satake, Y. Okano, S. Mori, S. Yata, K. Naoi, P. Simon, K. Naoi, R.B. Sepe, A. Steyerl, S.P. Bastien, J.R. Miller, A.F. Burke, A.K. Shukla, A. Banerjee, M.K. Ravikumar, A. Jalajakshi, F. Ciccarelli, D. Iannuzzi, M.-S. Park, Y.-G. Lim, J.-H. Kim, Y.-J. Kim, J. Cho, J.-S. Kim, M.-S. Park, Y.-G. Lim, S.M. Hwang, J.H. Kim, J.-S. Kim, S.X. Dou, J. Cho, Y.-J. Kim, M.-S. Park, Y.-G. Lim, J.-W. Park, J.-S. Kim, J.-W. Lee, J.H. Kim, S.X. Dou, Y.-J. Kim, M.M. Thackeray, M.K.Y. Chan, L. Trahey, S. Kirklin, C. Wolverton, M. Noh, J. Cho, R. Luge, R. Hoppe, M.K. Aydinol, G. Ceder, C. Frayret, A. Villesuzanne, N. Spaldin, E. Bousquet, J.-N. Chotard, N. Recham, J.-M. Tarascon, D. Carlier, A. Van der Ven, C. Delmas, G. Ceder, M. Wagemaker, A. Van Der Ven, D. Morgan, G. Ceder, F.M. Mulder, G.J. Kearley, Anti-fluorite Li_6CoO_4 as an alternative lithium source for lithium ion capacitors: an experimental and first principles study, J. Mater. Chem. A. 3 (2015) 12377–12385. doi:10.1039/C5TA00297D.

[181] S. Kirklin, M.K.Y. Chan, L. Trahey, M.M. Thackeray, C. Wolverton, High-throughput Screening of High-capacity Electrodes for Hybrid Li-ion–Li–O2 Cells, Phys. Chem. Chem. Phys. 16 (2014) 22073–22082. doi:10.1039/C4CP03597F.

[182] C.S. Johnson, S.-H. Kang, J.T. Vaughey, S. V. Pol, M. Balasubramanian, M.M. Thackeray, Li2O Removal from Li5FeO4: A Cathode Precursor for Lithium-Ion Batteries, Chem. Mater. 22 (2010) 1263–1270. doi:10.1021/cm902713m.

[183] L. Trahey, C.S. Johnson, J.T. Vaughey, S.-H. Kang, L.J. Hardwick, S.A. Freunberger, P.G. Bruce, M.M. Thackeray, Activated Lithium-Metal-Oxides as Catalytic Electrodes for Li–O2 Cells, Electrochem. Solid-State Lett. 14 (2011) A64. doi:10.1149/1.3555366.

[184] E. Cockayne, A. van de Walle, Building Effective Models from Scarce but Accurate Data: Application to an Alloy Cluster Expansion Model, Phys. Rev. B. 81 (2010) 12104–12113.

[185] S. Hao, C. Wolverton, Lithium Transport in Amorphous Al2O3 and AlF3 for Discovery of Battery Coatings, J. Phys. Chem. C. 117 (2013) 8009–8013. doi:10.1021/jp311982d.

[186] A. HIRANO, T. MATSUMURA, M. UEDA, N. IMANISHI, Y. TAKEDA, M. TABUCHI, Electrochemical properties and Mössbauer effect of anti-fluorite type compound, LiFeO, Solid State Ionics. 176 (2005) 2777–2782. doi:10.1016/j.ssi.2005.08.013.

[187] T. Okumura, M. Shikano, H. Kobayashi, Effect of bulk and surface structural changes in Li 5 FeO 4 positive electrodes during first charging on subsequent lithium-ion battery performance, J. Mater. Chem. A. 2 (2014) 11847. doi:10.1039/C4TA01884B.

[188] V.A. Maroni, C.S. Johnson, S.C.M. Rood, A.J. Kropf, D.A. Bass, Characterization of novel lithium battery cathode materials by spectroscopic methods: the $Li5+xFeO_4$ system., Appl. Spectrosc. 67 (2013) 903–12. doi:10.1366/12-06893.

[189] K. Gilmore, J. Vinson, E.L. Shirley, D. Prendergast, C.D. Pemmaraju, J.J. Kas, F.D. Vila, J.J. Rehr, Efficient implementation of core-excitation Bethe-Salpeter equation

calculations, Comput. Phys. Commun. 197 (2015) 109–117. doi:10.1016/j.cpc.2015.08.014.

[190] J. Vinson, J.J. Rehr, J.J. Kas, E.L. Shirley, Bethe-Salpeter equation calculations of core excitation spectra, Phys. Rev. B. 83 (2011) 115106–115112. doi:10.1103/PhysRevB.83.115106.

[191] H. Meyer, R. Hoppe, Zum thermischen Verhalten von Li3MnO4 I. [1]. Über α- und β-Li3MnO4, Z. Anorg. Allg. Chem. 424 (1976) 249–256. doi:10.1002/zaac.19764240308.

[192] J.A. Saint, M.M. Doeff, J. Reed, Synthesis and electrochemistry of Li3MnO4: Mn in the +5 oxidation state, J. Power Sources. 172 (2007) 189–197. doi:10.1016/j.jpowsour.2007.07.027.

[193] R.G. Burns, Mineralogical Applications of Crystal Field Theory, Cambridge University Press, 1993.

[194] A. Togo, F. Oba, I. Tanaka, First-principles calculations of the ferroelastic transition between rutile-type and CaCl2-type SiO 2 at high pressures, Phys. Rev. B. 78 (2008) 134106–134114. doi:10.1103/PhysRevB.78.134106.

[195] J. Heyd, G.E. Scuseria, M. Ernzerhof, Hybrid functionals based on a screened Coulomb potential, J. Chem. Phys. 118 (2003) 8207–8215. doi:10.1063/1.1564060.

[196] B.S. Murty, S. Ranganathan, Novel materials synthesis by mechanical alloying/milling, Int. Mater. Rev. 43 (1998) 101–141. doi:10.1179/imr.1998.43.3.101.

[197] G.F. Zhou, H. Bakker, Mechanically induced structural and magnetic changes in the GdAl2 Laves phase, Phys. Rev. B. 52 (1995) 9437–9445. doi:10.1103/PhysRevB.52.9437.

[198] R. Wang, X. Li, L. Liu, J. Lee, D.-H. Seo, S.-H. Bo, A. Urban, G. Ceder, A disordered

rock-salt Li-excess cathode material with high capacity and substantial oxygen redox

activity: Li1.25Nb0.25Mn0.5O2, Electrochem. Commun. 60 (2015) 70–73.

doi:10.1016/j.elecom.2015.08.003.

[199] K. Schubert, M. Poetzschke, Zum Aufbau einiger T4-B3 homologer und quasihomologer

Systeme. I. Die Systeme Ti-Ga, Zr-Ga und Hf-Ga, Naturwissenschaften. 53 (1962) 474–

488.

[200] G. Brachtel, R. Hoppe, Die Koordinationszahl 5 bei MnIII: Na4Mn2O5 [1,2], Zeitschrift

Für Anorg. Und Allg. Chemie. 468 (1980) 130–136. doi:10.1002/zaac.19804680116.

[201] N.N. (Norman N. Greenwood, A. (Alan) Earnshaw, Chemistry of the elements,

Butterworth-Heinemann, 1997.

[202] K.S. Novoselov, A.K. Geim, S. V Morozov, D. Jiang, Y. Zhang, S. V Dubonos, I. V

Grigorieva, A.A. Firsov, Electric Field Effect in Atomically Thin Carbon Films., Science

(80-.). 306 (2004) 666–669. doi:10.1126/science.1102896.

[203] E. Yoo, J. Kim, E. Hosono, H. Zhou, T. Kudo, I. Honma, Large Reversible Li Storage of

Graphene Nanosheet Families for Use in Rechargeable Lithium Ion Batteries, Nano Lett.

8 (2008) 2277–2282. doi:10.1021/nl800957b.

[204] H. Wang, L.-F. Cui, Y. Yang, H. Sanchez Casalongue, J.T. Robinson, Y. Liang, Y. Cui,

H. Dai, Mn3O4−Graphene Hybrid as a High-Capacity Anode Material for Lithium Ion

Batteries, J. Am. Chem. Soc. 132 (2010) 13978–13980. doi:10.1021/ja105296a.

[205] K. Takeda, K. Shiraishi, Theoretical Possibility of Stage Corrugation in Si and Ge

Analogs of Graphite, Phys. Rev. B. 50 (1994) 14916–14922.

doi:10.1103/PhysRevB.50.14916.

[206] G.G. Guzmán-Verri, L.C. Lew Yan Voon, Electronic Structure of Silicon-Based Nanostructures, Phys. Rev. B. 76 (2007) 75131. doi:10.1103/PhysRevB.76.075131.

[207] S. Cahangirov, M. Topsakal, E. Aktürk, H. \cSahin, S. Ciraci, Two- and One-Dimensional Honeycomb Structures of Silicon and Germanium, Phys. Rev. Lett. 102 (2009) 236804. doi:10.1103/physrevlett.102.236804.

[208] P. Vogt, P. De Padova, C. Quaresima, J. Avila, E. Frantzeskakis, M.C. Asensio, A. Resta, B. Ealet, G. Le Lay, Silicene: Compelling Experimental Evidence for Graphenelike Two-Dimensional Silicon, Phys. Rev. Lett. 108 (2012) 155501.

[209] W. Li, Y. Yang, G. Zhang, Y.-W. Zhang, Ultrafast and Directional Diffusion of Lithium in Phosphorene for High-Performance Lithium-Ion Battery, Nano Lett. 15 (2015) 1691–1697. doi:10.1021/nl504336h.

[210] H. Tang, S. Ismail-Beigi, Novel Precursors for Boron Nanotubes: The Competition of Two-Center and Three-Center Bonding in Boron Sheets, Phys. Rev. Lett. 99 (2007) 115501–115504. doi:10.1103/PhysRevLett.99.115501.

[211] J. Ni, Y. Zhao, L. Li, L. Mai, Ultrathin MoO_2 Nanosheets for Superior Lithium Storage, Nano Energy. 11 (2015) 129–135. doi:10.1016/j.nanoen.2014.10.027.

[212] H.A. Eivari, S.A. Ghasemi, H. Tahmasbi, S. Rostami, S. Faraji, R. Rasoulkhani, S. Goedecker, M. Amsler, Two-Dimensional Hexagonal Sheet of TiO_2, Chem. Mater. 29 (2017) 8594–8603. doi:10.1021/acs.chemmater.7b02031.

[213] R. Bhandavat, L. David, G. Singh, Synthesis of Surface-Functionalized WS_2 Nanosheets and Performance as Li-Ion Battery Anodes, J. Phys. Chem. Lett. 3 (2012) 1523–1530. doi:10.1021/jz300480w.

[214] M. Naguib, J. Come, B. Dyatkin, V. Presser, P.-L. Taberna, P. Simon, M.W. Barsoum, Y. Gogotsi, MXene: A Promising Transition Metal Carbide Anode for Lithium-ion Batteries, Electrochem. Commun. 16 (2012) 61–64. doi:10.1016/j.elecom.2012.01.002.

[215] D. Er, J. Li, M. Naguib, Y. Gogotsi, V.B. Shenoy, Ti3C2 MXene as a High Capacity Electrode Material for Metal (Li, Na, K, Ca) Ion Batteries, ACS Appl. Mater. Interfaces. 6 (2014) 11173–11179. doi:10.1021/am501144q.

[216] L. Peng, Y. Zhu, D. Chen, R.S. Ruoff, G. Yu, Two-Dimensional Materials for Beyond-Lithium-Ion Batteries, Adv. Energy Mater. 6 (2016) 1600025–1600045. doi:10.1002/aenm.201600025.

[217] S. Lebègue, T. Björkman, M. Klintenberg, R.M. Nieminen, O. Eriksson, Two-Dimensional Materials from Data Filtering and Ab Initio Calculations, Phys. Rev. X. 3 (2013) 31002. doi:10.1103/PhysRevX.3.031002.

[218] M. Amsler, S.M. Clarke, J.P.S. Walsh, T. Yu, Y. Wang, Y. Meng, S.D. Jacobsen, C. Wolverton, D.E. Freedman, Creating Binary Cu-Bi Compounds Via High-Pressure Synthesis: A Combined Experimental and Theoretical Study, Chem. Mater. 29 (2017) 5276–5285. doi:10.1021/acs.chemmater.7b01418.

[219] B.T. Matthias, A. Jayaraman, T.H. Geballe, K. Andres, E. Corenzwit, Many More Superconducting Bismuth Phases, Phys. Rev. Lett. 17 (1966) 640–643. doi:10.1103/PhysRevLett.17.640.

[220] G.L.W. Hart, R.W. Forcade, Algorithm for generating derivative structures, Phys. Rev. B. 77 (2008) 224115. doi:10.1103/PhysRevB.77.224115.

[221] T. Thonhauser, V.R. Cooper, S. Li, A. Puzder, P. Hyldgaard, D.C. Langreth, Van der

Waals density functional: Self-consistent potential and the nature of the van der Waals bond, Phys. Rev. B. 76 (2007) 125112–125122. doi:10.1103/PhysRevB.76.125112.

[222] F. Bonaccorso, L. Colombo, G. Yu, M. Stoller, V. Tozzini, A.C. Ferrari, R.S. Ruoff, V. Pellegrini, Graphene, Related Two-Dimensional Crystals, and Hybrid Systems for Energy Conversion and Storage, Science (80-.). 347 (2015) 1246501. doi:10.1126/science.1246501.

[223] E.G. Leggesse, C.-L. Chen, J.-C. Jiang, Lithium Diffusion in Graphene and Graphite: Effect of Edge Morphology, Carbon N. Y. 103 (2016) 209–216. doi:10.1016/j.carbon.2016.03.016.

[224] M. Park, X. Zhang, M. Chung, G.B. Less, A.M. Sastry, A Review of Conduction Phenomena in Li-ion Batteries, J. Power Sources. 195 (2010) 7904–7929. doi:10.1016/j.jpowsour.2010.06.060.

[225] N. Nitta, F. Wu, J.T. Lee, G. Yushin, Li-ion battery materials: present and future, Mater. Today. 18 (2015) 252–264. doi:10.1016/j.mattod.2014.10.040.

[226] X. Zhou, F. Wang, Y. Zhu, Z. Liu, Graphene modified LiFePO4 cathode materials for high power lithium ion batteries, J. Mater. Chem. 21 (2011) 3353–3358. doi:10.1039/c0jm03287e.

[227] L. Jaber-Ansari, K.P. Puntambekar, S. Kim, M. Aykol, L. Luo, J. Wu, B.D. Myers, H. Iddir, J.T. Russell, S.J. Saldaña, R. Kumar, M.M. Thackeray, L.A. Curtiss, V.P. Dravid, C. Wolverton, M.C. Hersam, Suppressing Manganese Dissolution from Lithium Manganese Oxide Spinel Cathodes with Single-Layer Graphene, Adv. Energy Mater. 5 (2015) 1500646–1500655. doi:10.1002/aenm.201500646.

[228] A. Abouimrane, D. Dambournet, K.W. Chapman, P.J. Chupas, W. Weng, K. Amine, A new class of lithium and sodium rechargeable batteries based on selenium and selenium-sulfur as a positive electrode., J. Am. Chem. Soc. 134 (2012) 4505–8. doi:10.1021/ja211766q.

[229] Y. Cui, A. Abouimrane, J. Lu, T. Bolin, Y. Ren, W. Weng, C. Sun, V.A. Maroni, S.M. Heald, K. Amine, (De)Lithiation Mechanism of Li/SeSx (x = 0–7) Batteries Determined by in Situ Synchrotron X-ray Diffraction and X-ray Absorption Spectroscopy, J. Am. Chem. Soc. 135 (2013) 8047–8056. doi:10.1021/ja402597g.

[230] C. Luo, Y. Xu, Y. Zhu, Y. Liu, S. Zheng, Y. Liu, A. Langrock, C. Wang, Selenium@mesoporous carbon composite with superior lithium and sodium storage capacity., ACS Nano. 7 (2013) 8003–10. doi:10.1021/nn403108w.

[231] C.-P. Yang, S. Xin, Y.-X. Yin, H. Ye, J. Zhang, Y.-G. Guo, An advanced selenium-carbon cathode for rechargeable lithium-selenium batteries., Angew. Chem. Int. Ed. Engl. 52 (2013) 8363–7. doi:10.1002/anie.201303147.

[232] D.E. Farrell, C. Wolverton, Structure and diffusion in liquid complex hydrides via ab initio molecular dynamics, Phys. Rev. B. 86 (2012) 174203–174214. doi:10.1103/PhysRevB.86.174203.

[233] S. Nosé, A unified formulation of the constant temperature molecular dynamics methods, J. Chem. Phys. 81 (1984) 511–519. doi:10.1063/1.447334.

[234] S. Nosé, Constant Temperature Molecular Dynamics Methods, Prog. Theor. Phys. Suppl. 103 (1991) 1–46. doi:10.1143/PTPS.103.1.

[235] M. Matsuo, S. Orimo, Lithium Fast-Ionic Conduction in Complex Hydrides: Review and

Prospects, Adv. Energy Mater. 1 (2011) 161–172. doi:10.1002/aenm.201000012.

[236] A. Züttel, P. Wenger, S. Rentsch, P. Sudan, P. Mauron, C. Emmenegger, LiBH4 a New Hydrogen Storage Material, J. Power Sources. 118 (2003) 1–7. doi:10.1016/S0378-7753(03)00054-5.

[237] A. Züttel, S. Rentsch, P. Fischer, P. Wenger, P. Sudan, P. Mauron, C. Emmenegger, Hydrogen Storage Properties of LiBH4, J. Alloys Compd. 356–357 (2003) 515–520. doi:10.1016/S0925-8388(02)01253-7.

[238] Y. Zhang, Y. Wang, K. Michel, C. Wolverton, First-principles Insight into the Degeneracy of Ground-state LiBH4 Structures, Phys. Rev. B. 86 (2012) 94111. doi:10.1103/PhysRevB.86.094111.

[239] M. Matsuo, Y. Nakamori, S. Orimo, H. Maekawa, H. Takamura, Lithium Superionic Conduction in Lithium Borohydride Accompanied by Structural Transition, Appl. Phys. Lett. 91 (2007) 224103–224105. doi:10.1063/1.2817934.

[240] E. Orgaz, A. Membrillo, R. Castañeda, A. Aburto, Electronic Structure of Ternary Hydrides Based on Light Elements, J. Alloys Compd. 404 (2005) 176–180. doi:10.1016/j.jallcom.2004.11.111.

[241] L. Mosegaard, B. Moller, J.-E. Jorgensen, Y. Filinchuk, Y. Cerenius, J.C. Hanson, E. Dimasi, F. Besenbacher, T.R. Jensen, Reactivity of LiBH4: In Situ Synchrotron Radiation Powder X-ray Diffraction Study, J. Phys. Chem. C. 112 (2008) 1299–1303. doi:10.1021/jp076999v.

[242] L.H. Rude, O. Zavorotynska, L.M. Arnbjerg, D.B. Ravnsbæk, R.A. Malmkjær, H. Grove, B.C. Hauback, M. Baricco, Y. Filinchuk, F. Besenbacher, T.R. Jensen, Bromide

Substitution in Lithium Borohydride, LiBH4–LiBr, Int. J. Hydrogen Energy. 36 (2011) 15664–15672. doi:10.1016/j.ijhydene.2011.08.087.

[243] L.M. Arnbjerg, D.B. Ravnsbæk, Y. Filinchuk, R.T. Vang, Y. Cerenius, F. Besenbacher, J.-E. Jørgensen, H.J. Jakobsen, T.R. Jensen, Structure and Dynamics for LiBH4−LiCl Solid Solutions, Chem. Mater. 21 (2009) 5772–5782. doi:10.1021/cm902013k.

[244] A. Borgschulte, R. Gremaud, S. Kato, N.P. Stadie, A. Remhof, A. Züttel, M. Matsuo, S.-I. Orimo, Anharmonicity in LiBH4–LiI Induced by Anion Exchange and Temperature, Appl. Phys. Lett. 97 (2010) 031916–031918. doi:10.1063/1.3467260.

[245] L.H. Rude, E. Groppo, L.M. Arnbjerg, D.B. Ravnsbæk, R.A. Malmkjær, Y. Filinchuk, M. Baricco, F. Besenbacher, T.R. Jensen, Iodide Substitution in Lithium Borohydride, LiBH4–LiI, J. Alloys Compd. 509 (2011) 8299–8305. doi:10.1016/j.jallcom.2011.05.031.

[246] H. Oguchi, M. Matsuo, J.S. Hummelshøj, T. Vegge, J.K. Nørskov, T. Sato, Y. Miura, H. Takamura, H. Maekawa, S. Orimo, Experimental and Computational Studies on Structural Transitions in the LiBH4–LiI Pseudobinary System, Appl. Phys. Lett. 94 (2009) 141912–141914. doi:10.1063/1.3117227.

[247] A.N. Cormack, K. Funke, N. Sammes, A. Petric, D. Edwards, R. Miyazaki, T. Karahashi, N. Kumatani, Y. Noda, M. Ando, H. Takamura, M. Matsuo, S. Orimo, H. Maekawa, Room Temperature Lithium Fast-ion Conduction and Phase Relationship of LiI Stabilized LiBH4, Solid State Ionics. 192 (2011) 143–147. doi:10.1016/j.ssi.2010.05.017.

[248] J.S.G. Myrdal, D. Blanchard, D. Sveinbjörnsson, T. Vegge, Li-ion Conduction in the LiBH4: LiI System from Density Functional Theory Calculations and Quasi-Elastic Neutron Scattering, J. Phys. Chem. C. 117 (2013) 9084–9091. doi:10.1021/jp311980h.

[249] J.S.G. Myrdal, D. Sveinbjornsson, T. Vegge, Computational Design and Synthesis of New Ternary Solid Li+ Superionic Conductors, Meet. Abstr. MA2011-02 (2011) 756. http://ma.ecsdl.org/content/MA2011-02/15/756.abstract (accessed July 30, 2014).

[250] N. Bernstein, M.D. Johannes, K. Hoang, First-principles Free Energy Calculations of the Structural Phase Transition in LiBH4 with I, Cl, Na, and K Substitution, Phys. Rev. B. 88 (2013) 220102–220106. doi:10.1103/PhysRevB.88.220102.

[251] J.P. Perdew, Y. Wang, Accurate and Simple Analytic Representation of The Electron-gas Correlation Energy, Phys. Rev. B. 45 (1992) 13244–13249. doi:10.1103/PhysRevB.45.13244.

[252] R.D. Shannon, IUCr, Revised Effective Ionic Radii and Systematic Studies of Interatomic Distances in Halides and Chalcogenides, Acta Crystallogr. Sect. A. 32 (1976) 751–767. doi:10.1107/S0567739476001551.

[253] K. Hoang, C.G. Van de Walle, Mechanism for the Decomposition of Lithium Borohydride, Int. J. Hydrogen Energy. 37 (2012) 5825–5832. doi:10.1016/j.ijhydene.2012.01.002.

[254] Z. Łodziana, T. Vegge, Structural Stability of Complex Hydrides: LiBH4 Revisited., Phys. Rev. Lett. 93 (2004) 145501–145504. http://www.ncbi.nlm.nih.gov/pubmed/15524809 (accessed July 2, 2013).

[255] A. V Skripov, A. V Soloninin, M.B. Ley, T.R. Jensen, Y. Filinchuk, Nuclear Magnetic Resonance Studies of BH4 Reorientations and Li Diffusion in LiLa(BH4)3Cl, J. Phys. Chem. C. 117 (2013) 14965–14972. doi:10.1021/jp403746m.

Publication List

[1] C. Zhan†, **Z. Yao†**, J. Lu, L. Ma, V. Maroni, L. Li, E. Lee, E. E. Alp, T. Wu, J. Wen, Y. Ren, C. S. Johnson, M. M. Thackeray, M. Chan, <u>C. Wolverton</u>, K. Amine, Enabling the High Capacity of Lithium-rich Anti-fluorite Lithium Iron Oxide by Simultaneous Anionic and Cationic Redox, Nature Energy 2, 963–971 (2017). (†: Equal Contribution)

[2] H. Liu, Q. Li, **Z. Yao**, L. Li, Y. Li, <u>C. Wolverton</u>, M. C. Hersam, J. Wu, V. P. Dravid, Origin of Fracture-resistance to Large Volume Change in Cu-substituted Co_3O_4 Electrode, Advanced Materials, 1704851, (2017).

[3] **Z. Yao**, S. Kim, M. Aykol, Q. Li, J. Wu, J. He, <u>C. Wolverton</u>. Revealing the Conversion Mechanism of Transition Metal Oxide Electrodes during Lithiation from First Principles, Chemistry of Materials 29(21), 9011-9022 (2017).

[4] Q. Li†, **Z. Yao†**, J. Wu†, S. Mitra, S. Hao, T. S. Sahu, Y. Li, <u>C. Wolverton</u>, V. P. Dravid, Intermediate Phases in Sodium Intercalation into MoS_2 Nanosheets and Its Implications for Sodium-Ion Battery, Nano Energy 38, 342-349 (2017). (†: Equal Contribution)

[5] Q. Li†, J. Wu†, **Z. Yao†**, M. M. Thackeray, <u>C. Wolverton</u>, V. P. Dravid, Dynamic Imaging of Metastable Reaction Pathways in Lithiated Metal Oxide Electrodes, Nano Energy 44, 15-22 (2018). (†: Equal Contribution)

[6] M. Amsler, **Z. Yao**, <u>C. Wolverton</u>. Cubine, A Quasi 2-dimensional Copper-bismuth Nano Sheet, Chemistry of Materials 29(22), 9819-9828 (2017).

[7] K. He, **Z. Yao**, S. Hwang, N. Li, K. Sun, H. Gan, Y. Du, H. Zhang, <u>C. Wolverton</u>, D Su. Kinetically-Driven Phase Transformation during Lithiation in Copper Sulfide Nanoflakes, Nano Letters 17(9), 5726-5733 (2017).

[8] Q. Li, H. Liu, **Z. Yao**, J. Cheng, T. Li, Y. Li, <u>C. Wolverton</u>, J. Wu, V. P. Dravid. Electrochemistry of Selenium with Sodium and Lithium: Kinetics and Reaction Mechanism, ACS Nano 10(9), 8788-8795 (2016).

[9] H. Bin, **Z. Yao**, S. Zhu, C. Zhu, H. Pan, Z. Chen, <u>C. Wolverton</u>, D. Zhang, A High-Performance Anode Material Based on $FeMnO_3$/Graphene Composite, Journal of Alloys and Compounds 695, 1223-1230 (2017).

[10] **Z. Yao**, S. Kim, J. He, V. I. Hegde, <u>C. Wolverton</u>, Interplay of Cation and Anion Redox in $Li_4Mn_2O_5$ Material and Prediction of Improved $Li_4(Mn,M)_2O_5$ Cathodes for Li-ion Batteries, Under review.

[11] **Z. Yao**, S. Kim, K. Michel, Y. Zhang, M. Aykol, <u>C. Wolverton</u>, Stability and Conductivity Study of the Complex Lithium Borohydride Based Solid-state Electrolytes from First Principles, Under review.

[12] **Z. Yao**, V. Hedge, M. K. Y. Chan, M. M. Thackeray, and <u>C. Wolverton</u>, A High-Throughput Discovery of Novel Hybrid Metal-ion-Metal-O_2 Battery Chemistries Metal = Li, Na, Mg, and Al, In preparation.

[13] **Z. Yao**, C. Zhan, J. Lu, L. Li, M. K. Y. Chan, M. M. Thackeray, <u>C. Wolverton</u>, Exploring the Combined Anionic and Cationic Redox Reactivity in the Super Li-rich Li_5FeO_4 Based High-Energy-Density Cathode Materials, In preparation.

[14] S. Hwang, **Z. Yao**, L. Zhang, M. Fu, K. He, L. Mai, <u>C. Wolverton</u>, D. Su, Multi-step Lithiation of Tin Sulfide: An Investigation using In-Situ Electron Microscopy, Under review.

[15]   L. Li, **Z. Yao**, J. Zhu, K. Chen, <u>C. Wolverton</u>, M. C. Hersam, Comprehensive Enhancement of Nanostructured NMC Cathode Materials *via* Conformal Graphene Dispersion, In preparation.

[16]   J. He, **Z. Yao**, <u>C. Wolverton</u>, Discovery of oxysulfide based Li-ion super ionic conductors, In preparation.

[17]   S. Kim, V. Hedge, **Z. Yao**, Z. Lu, <u>C. Wolverton</u>, First-principles Study on Lithium Cobalt Spinel Oxides: Current and Future Prospects, Under review

[18]   L. Li, S. Kim, **Z. Yao**, J. Zhu, K. Chen, L. M. Guiney, X. Liu, Z. Wang, <u>C. Wolverton</u>, M. C. Hersam, Toward A Qualitative Understanding of Graphene in Improving Electrochemical Performance of Spinel $LiMn_2O_4$ Cathodes, In preparation.

[19]   S. Kim, K. He, **Z. Yao**, C. Wolverton, V.P. Dravid, Exploring the electrochemical delithiation process of $LiFePO_4$, In preparation.

[20]   Y. Shi, **Z. Yao**, S. Zhu, D. Wang, <u>C. Wolverton</u>, and D. Zhang, Design and Fabrication of carbon-coated porous multiple metal oxide for lithium-ion battery with high performance. In preparation.

[21]   J. Khoury; S. Hao, C. Stoumpos, **Z. Yao**, C. Malliakas, U. Aydemir, T. Slade, G. Snyder, <u>C. Wolverton</u>, M. Kanatzidis, Quaternary Pavonites $A_{1+x}Sn_{2-x}Bi_{5+x}S_{10}$ (A+ = Li+, Na+): Site Occupancy Disorder Defines Electronic Structure, Under review.

[22]   L. Li, F. Castro, J. S. Park, E. Lee, J.W. Freeland, **Z. Yao**, T. T. Fister, J. Vinson, E. L. Shirley, <u>C. Wolverton</u>, V. P. Dravid, M. M. Thackeray, and M. K.Y. Chan, Probing Electrochemically-Induced Oxygen Redox Reactions in Li_2IrO_3, Under review.